ABSTRACT

Title of Document: A MULTI-MODE MAGNETORHEOLOGICAL AXIAL ISOLATOR

Mikel J. Brigley, Master of Science, 2006

Directed By: Professor, Dr. Norman Wereley, Department of Aerospace Engineering

MR dampers are semi-active devices that are finding success where controllable damping is required. The goal of this work is to determine a suitable design of a six-degree-of-freedom MR isolator for vibration attenuation of a sensor platform and characterize its axial performance through experiments as well as theoretical modeling. This investigation is begun by developing several MR designs and through experiment a single design is chosen for further analysis.

Several methods of characterization, including equivalent damping and the complex modulus approach, are used to study the behavior of the MR damper. Several theoretical models for the MR damper are developed: one based upon the Bingham plastic model and the other a nonlinear hysteresis model. The methods used to determine the models parameters are discussed and model results are compared to experimental results.

A MULTI-MODE MAGNETORHEOLOGICAL AXIAL ISOLATOR

By

Mikel J. Brigley.

Thesis submitted to the Faculty of the Graduate School of the
University of Maryland, College Park, in partial fulfillment
of the requirements for the degree of
Master of Science
2006

Advisory Committee:
Professor Norman Wereley, Chair
Professor Alison Flatau
Dr. Young-Tai Choi

Dedication

To my Mom and Dad for providing all of the tools necessary to achieve my goals.

To my girlfriend, Cristina, for her encouragement and support throughout my graduate studies.

Acknowledgements

My thanks to Dr. Norman Wereley for giving me the opportunity to work on this project. He offered much advice and guidance throughout the process. I would also like to thank Dr. Choi who has been a great teacher, advisor and friend. Without his incredible support this would not have been possible.

Table of Contents

List of Figures

Chapter 1: Introduction

1.1 Background

In recent years vibration attenuation in aerial vehicles has attracted increasing attention because of stringent performance requirements, such as static and dynamic pointing accuracy during flight [10,11]. In order to achieve this, many payloads demand high precision from the host craft in order to perform their mission. The transmission of disturbances to sensitive instruments and payloads has resulted in malfunctioning components, shorter lifetime and degradation of overall operational performance. In particular, extreme vibration and shock environments are produced during fast maneuvers as well as take-off and landing of these aerial vehicles [10]. In the past this extreme liftoff environment has exacerbated malfunctions of the spacecraft subcomponents. The vibration produced during fast maneuvering has translated into problems such as poor imaging and tracking capabilities (loss of line of sight), resulting in an inability to follow a desired trajectory path. In certain cases, loss of line of sight has resulted in catastrophic mission failures. A solution to this dilemma is to isolate precision payloads from the vehicle.

Vibration isolation in the high frequency range can be achieved by placing soft (low damping and stiffness) isolators into the transmission path of excitation [21]. However, soft isolators lead to large vibration of the payload in the low frequency range, particularly at the resonant frequency—where firm (high damping and stiffness) isolators are desired. Typical passive isolators cannot produce a substantial change in their dynamic properties, of damping and stiffness, resulting in

designs that are a trade-off between soft and firm components. Inherently, a damper, which could significantly change its dynamic properties would be better than one in which these properties are fixed as vibration attenuation in both the low and high frequency range would then be possible.

1.2 MR Dampers

Magnetorheological (MR) fluids are suspensions of soft magnetically permeable micron-sized particles, such as iron or cobalt, in a non-magnetic carrier fluid. In the absence of a magnetic field these particles are randomly dispersed in the fluid. However, upon application of a magnetic field, the particles form chains, aligned parallel with the magnetic flux lines, causing a significant increase in the resistance to flow in the MR fluid. In order to yield these chain structures and induce fluid flow a finite stress, called the yield stress, must be developed, where its magnitude is dependent upon several factors including the strength and distribution of the applied magnetic field, particle size, particle concentration and particle compositions. As such, the rheological properties of the fluid can be reversibly changed upon application of a magnetic field. [1,2]

MR fluids are finding success in applications where controllable damping is desired. They have been employed or proposed for: earthquake hazard mitigation [4], lag mode damping in helicopter rotors [3], and vehicle suspensions [5]. MR dampers have been designed on the basis of the operating modes of the fluid: shear mode (Couette), flow mode (Poiseuille flow), squeeze mode, and mixed mode (Poiseuille and Couette flow). In the shear mode the chains resist the relative displacement of bordering plates as can be seen in figure 1.1(a). In the flow mode, shown in figure

1.1(b), the chain structures are deformed and resist a pressure difference. In the squeeze mode the chains prevent the draining off of fluid, this is shown in figure 1.1(c) [1].

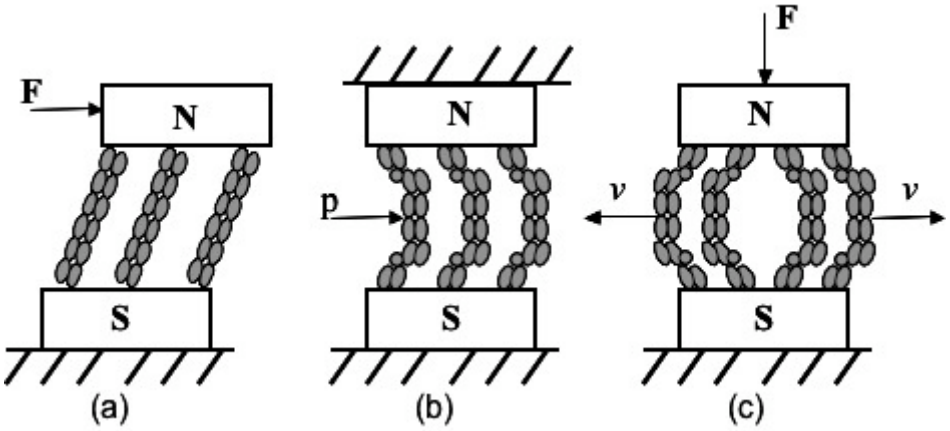

Figure 1.1 Stress modes for MR fluid (a) shear mode, (b) flow mode and (c) squeeze mode.

The operating mode of the fluid is typically chosen based upon the application parameters that the damper will encounter. Squeeze mode dampers are capable of producing large forces, however they are limited to small displacement amplitudes in order to avoid contact of the two plates. Shear mode dampers can afford large displacement amplitudes, but they require large active surface areas in order to produce large forces. Flow mode or mixed mode devices can be designed with smaller magnetic pole surface areas and are capable of large displacement amplitudes in the axial direction. From a practical design standpoint, dampers are often constructed based on flow mode or mixed mode operation to accommodate high force and long stroke.

1.3 MR Models

In 1969, Phillips showed that fluids with a variable yield stress could be modeled as an idealized Bingham plastic material [7]. This model, due to its simplicity, has been widely used to describe ER and MR fluid behavior [6,8]. The fluid is assumed to possess a yield stress, τ_y, which varies according to the applied magnetic field. As discussed in section 1.1, the onset of fluid flow does not occur until the applied shear stress reaches the yield stress. Once the material is stressed beyond this point, it begins to flow like a Newtonian fluid with a constant viscosity, μ. The constitutive equation for the shear stress of the fluid is expressed as [7]

$$\tau = \tau_y \operatorname{sgn}(u) + \mu \frac{du}{dy} \tag{1.1}$$

where u is the velocity.

The Bingham plastic model is a steady state model and assumes the fluid is in the post-yield phase flowing with a constant shear rate. In the pre-yield condition the model implies that the material is rigid. This is appropriate only for high strain rates where the onset of flow has occurred. For small strain rates below the critical yield stress, there is some elastic deformation, which the Bingham plastic model ignores. As such, other models have been proposed to account for the pre-yield behavior of the fluid, which is necessary to capture the fluids dynamic behavior. Kamath and Wereley presented a nonlinear viscoelastic-plastic model, which accounted for behavior in both the pre-yield and post-yield regimes as well as the transition through the yield phase [9]. Choi and Wereley proposed a nonlinear hysteresis model, which also captured the yielding behavior of the MR fluid [22].

In this study, the quasi-steady assumption will be made and analysis will be developed using the Bingham plastic model as well as a nonlinear hysteresis model. Furthermore, it has been shown that MR devices with flow between concentric cylinders can be approximated by flow between parallel flat-plates. Atkin showed that the error associated with this assumption is small for both flow mode and shear mode operation when the annular gap is small relative to its diameter [8].

In order to develop an effective control scheme, it is necessary to have an accurate damping force model that can capture the hysteresis behavior of the MR isolator. A common approach is to describe the isolator behavior with a network of ideal devices such as a viscous damper, elastic spring or coulomb friction element. Two such models are the Kelvin chain model and the Bingham plastic model with a spring element.

The Kelvin chain model, a linear model, uses a parallel combination of a viscous damper and an elastic spring. The damper is included to capture the viscous behavior of the MR isolator while the spring is used to simulate the elastic behavior of the MR isolator. In addition these linear elements must be used to capture the yield force behavior of the MR fluid.

The modified Bingham model uses a parallel combination of an elastic spring, a coulomb friction element and a viscous damping element. This model is essentially the Kelvin chain with a coulomb element added to account for the yield force of the MR fluid.

By appropriately identifying the ideal devices used in the previous models, it is possible to replicate the behavior of the MR isolator.

1.4 Organization

The goal of this work is to determine a suitable design of a six-degree-of-freedom MR isolator for vibration attenuation of a sensor platform and characterize its axial performance through experiments as well as theoretical modeling. Developing several MR designs begins this investigation and through experiment the most favorable is determined (Chapter 2). Next, the experimental setup and the methods used for characterization of the MR damper are discussed (Chapter 3). In Chapter 4, a theoretical model for the MR damper is developed using the Bingham plastic model. In Chapter 5, a nonlinear hysteresis model is developed using the hypertangent function. Lastly, the methods used to determine the models parameters are discussed and model results are compared to experimental results.

Chapter 2: MR Isolator Design

The initial objective of the project sought to satisfy the requirement of replacing three existing solid supports with MR isolators to lower vibration levels within a sensor platform. Three separate designs of MR isolators were considered. Due to limited volume for implementation, each design was required to be as compact as possible. A single MR isolator was allocated to fit within a volume measuring approximately 2.1 inches in length and width and 3.1 inches in height. It was desired to provide as wide a range of damping as possible while adhering to the given volume constraint.

2.1 Design 1

2.1.1 Description of Design

The first proposed MR isolator design was that of a flow mode damper, shown in figure 2.6. Using 1018 steel a bobbin and flux return were manufactured. The bobbin, shown in Figure 2.1(a) measured 15 mm in length and 28.6 mm in diameter. The flux return, shown in Figure 2.1(b) was a cup design. It was 18 mm in length and had an inside and outside diameter of 32.6 mm and 42 mm, respectively. The bobbin was wound using 24 gage insulated copper wire, and there were 119 total turns. The wound bobbin was then fastened into the flux return using a threaded bolt thus creating the magnetically active annulus through which the MR fluid would flow. The bobbin and flux return were assembled into the MR isolator according to figure 2.2. Upon completely filling the isolator with MR fluid, flow through the magnetically

active annulus is achieved when the elastomeric top experiences motion relative to the isolator base in any direction causing it to deform thus inducing fluid flow within the chamber. The diaphragm at the bottom of the fluid chamber also deforms and serves to accommodate the changing volume.

The MR fluid used in each design was supplied by Materials Modification Inc. (MMI) and is designated as 80% 90-10. This MR fluid uses silicon oil as the carrier fluid and has 80% loading by weight of solid magnetically permeable iron particles. The solid particles are 90% micron-sized particles and 10% nano-sized particles by weight.

The elastomeric top shown in figure 2.2 is a hydromount, which was purchased and then modified to allow installation into the MR device. This procedure greatly decreased the amount of design and machining required in building the MR isolators. The basis for choosing which commercially available hydromount to purchase and modify was two-fold; the hydromount had to be of appropriate size, and the hydromount had to have an elastomeric top, which could be separated and assembled into the proposed MR designs. The hydromount chosen for modification was the V250 by Contitech and is shown in figure 2.3(a). The V250 was cut and disassembled, preserving only the top rubber part and a small section of the original steel housing as seen in Figure 2.3(b). The flange was then milled down to allow placement into and a small steel outer cup—forming the exterior of the MR damper. The assembly of the modified hydromount and outer cup is shown in Figure 2.4. Four setscrews, as well as Scotch-Weld, bond the modified hydromount and outer cup together.

2.1.2 Validation of Design

In order to verify the effectiveness of the flow mode design as well as quantify the MR effect, force measurements from sinusoidal displacement cycles were recorded using a hydraulically powered MTS model 661.22 load frame. A more descriptive account of the testing rig can be found in chapter 3. The displacement amplitude was kept constant at 0.25 mm throughout the entire testing procedure while frequency was varied between 1 to 20 hz, in steps of 1hz. This was done for both zero and 1.5 amperes of applied current. The maximum force generated by the MR damper during each displacement cycle was plotted versus frequency. The results of the MTS testing are shown in figure 2.8. Upon application of current the flow mode isolator did not show an increase in maximum force. This was attributed to a complaint air bubble, resulting from an inability to completely fill the isolator with MR fluid, which hindered fluid flow within the MR device. To fill the isolator the hydromount stem was hollowed and using a syringe MR fluid was injected into the device. This technique did not allow the areas above the stem, shown in figure 2.4, to be filled with MR fluid. In order to solve this problem another MR design was proposed.

2.2 Design 2

2.2.1 Description of Design

The second design was a shear-squeeze-flow mode damper and is shown in figure 2.6. A bobbin with a diameter of 37 mm and a height of 17 mm (shown in figure 2.7) was created using aluminum, a non-magnetically permeable material. The bobbin was wound with 24 gage insulated copper wire totaling 189 turns. This wound

bobbin was attached to the stem of the modified hydromount using a steel screw, as shown in figure 2.6. The steel screw conducted the magnetic flux within the MR device and the steel outer cup served as the magnetic flux return, causing the area below the bobbin to be magnetically active. Axial motion of the elastomer—and consequently the bobbin—imposes radial flow of the fluid below the bobbin, thus creating a squeeze mode MR device. The radial flow will also cause flow along the sides of the bobbin. In this area passive shear and flow mode damping is present.

Two holes were drilled into the bottom of the outer cup to allow the isolator to be filled with MR fluid. This mitigated the filling problems found in design 1. Additionally, design 2 does not require the MR isolator to be completely filled. Damping will occur as long as the bobbin is submerged in MR fluid.

2.2.2 Validation of Design

Design 2 underwent the same testing procedure as design 1, described in section 2.1.2. Figure 2.8 shows the maximum force of the MR isolator over a displacement cycle versus frequency. Upon application of current, design 2 showed an increase in maximum force of approximately 3 Newtons. Although an MR effect was evident it was very small. In order to accomplish larger increases in force the magnetic circuit had to be improved. The conducting screw was very small and was therefore unable to accommodate the magnetic fields necessary to achieve a sufficiently high MR effect.

2.3 Design 3

2.3.1 Description of Design

In order to increase the MR effect of the shear-squeeze-flow mode design a new bobbin was manufactured. This bobbin was made from 1018 steel and had an increased thickness from that of design 2. Both of these changes would allow greater magnetic fluxes to be achieved in the MR device, as the magnetic conductor was now much larger. In addition, using a finite element model the effect of the bobbin's orientation on the magnetic field's strength and distribution was studied. Two orientations were considered. The first, seen in figure 2.9, has the bobbin installed disc side down. This is the bobbin orientation that was used in design 2. Another way to install the bobbin is disc side up, as is shown in figure 2.10. It was discovered via the FEM analysis that by installing the bobbin disc side up the area below the bobbin would generate a magnetic field strength 2.6 times higher than in the disc down configuration, thus increasing the squeeze mode effect. In addition, the section at the top of the bobbin, between the disc and the outer cylinder, became magnetically active. This allowed all of the operating modes (shear, squeeze and flow) to exploit the MR effect. For these reasons design 3 has the bobbin installed disc side up.

The new bobbin was wound using 24 gage insulated copper wire. There were 188 turns of the wire upon completion of winding. The bobbin was installed into the MR device by connecting it to the hydromount stem using a steel screw. A sectional view of design 3 is shown in figure 2.11. As in design 2, motion of the bobbin

induces fluid flow in the radial direction below the bobbin as well as flow within the annulus created by the side of the bobbin and the outer cup.

2.3.2 Validation of Design

Design 3 underwent the same testing as the previous designs. Figure 2.12 shows the maximum force versus frequency. It was found that design 3 was capable of a much greater range of damping force than design 2. Upon application of current design 3 showed an increase in maximum force of approximately 40 Newtons, while design 2 only increased by 3 Newtons, which is an order of magnitude improvement.

2.4 Results

The testing conducted on each of the isolators, summarized in Table 2.1, revealed that design 3 showed the largest dynamic range (ratio of field on to field off force) upon application of current. Design 3 was thus chosen as the superior of the proposed designs. It was desired to conduct further testing in order to fully characterize the isolator as well as develop a mathematical model of the MR isolator, which could successfully predict the isolator force.

Table 2.1 Dynamic Range of Isolator Designs

	MR Operating Modes			Maximum Force (N)		
	Shear	Squeeze	Flow	Field On	Field Off	Dynamic Range
Design 1			X	17	17	1
Design 2		X		18	15	1.2
Design 3	X	X	X	52	14	3.7

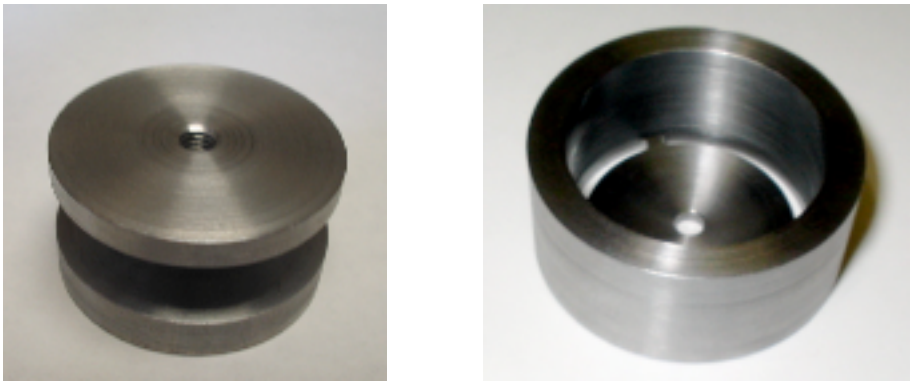

(a) (b)

Figure 2.1 Parts comprising the magnetically active annulus in design 1 (a) bobbin and (b) flux return.

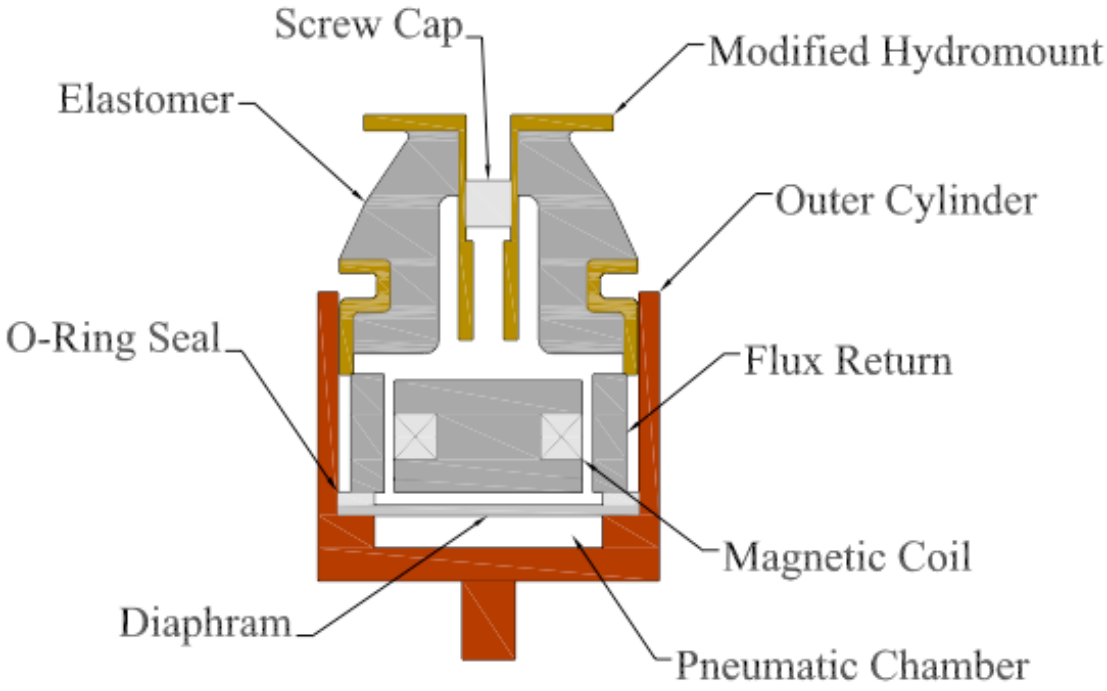

Figure 2.2 Sectional drawing of MR isolator design 1.

(a)

(b)

Figure 2.3 The V250 hydromount used in the MR isolators (a) unmodified hydromount and (b) hydromount cut and disassembled for placement into outer cup.

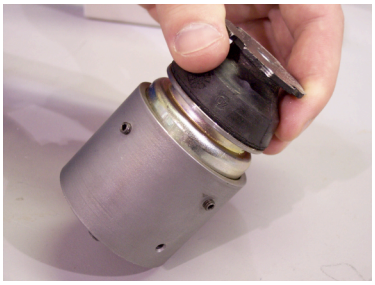

(a)

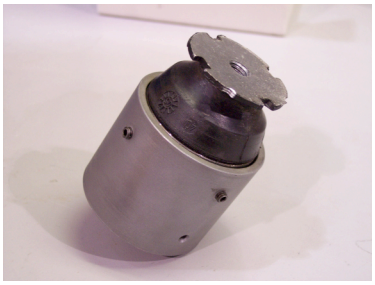

(b)

Figure 2.4 Creating the external housing of MR isolators (a) placing the modified hydromount into the outer cup and (b) the modified hydromount and outer cup bonded together.

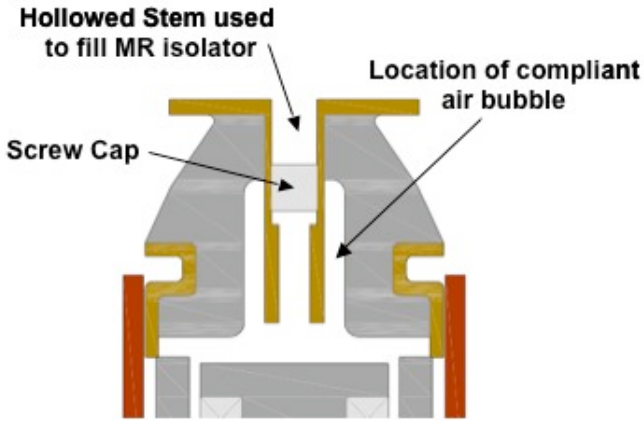

Figure 2.5 Elastomeric top of design 1 which was used to fill the isolator with MR fluid

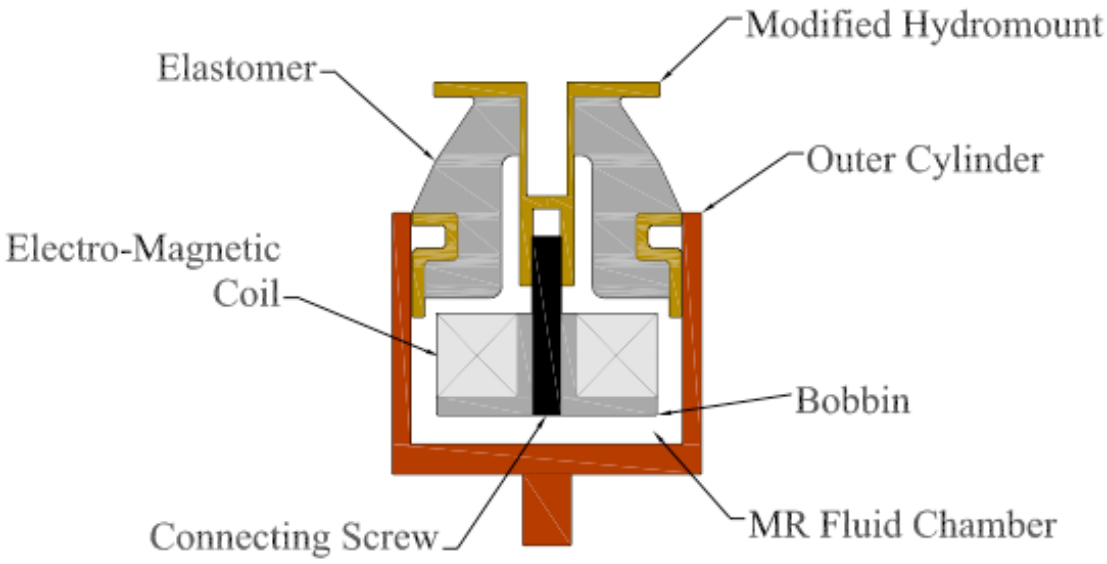

Figure 2.6 Sectional drawing of MR isolator design 2.

Figure 2.7 The bobbin manufactured for design 2

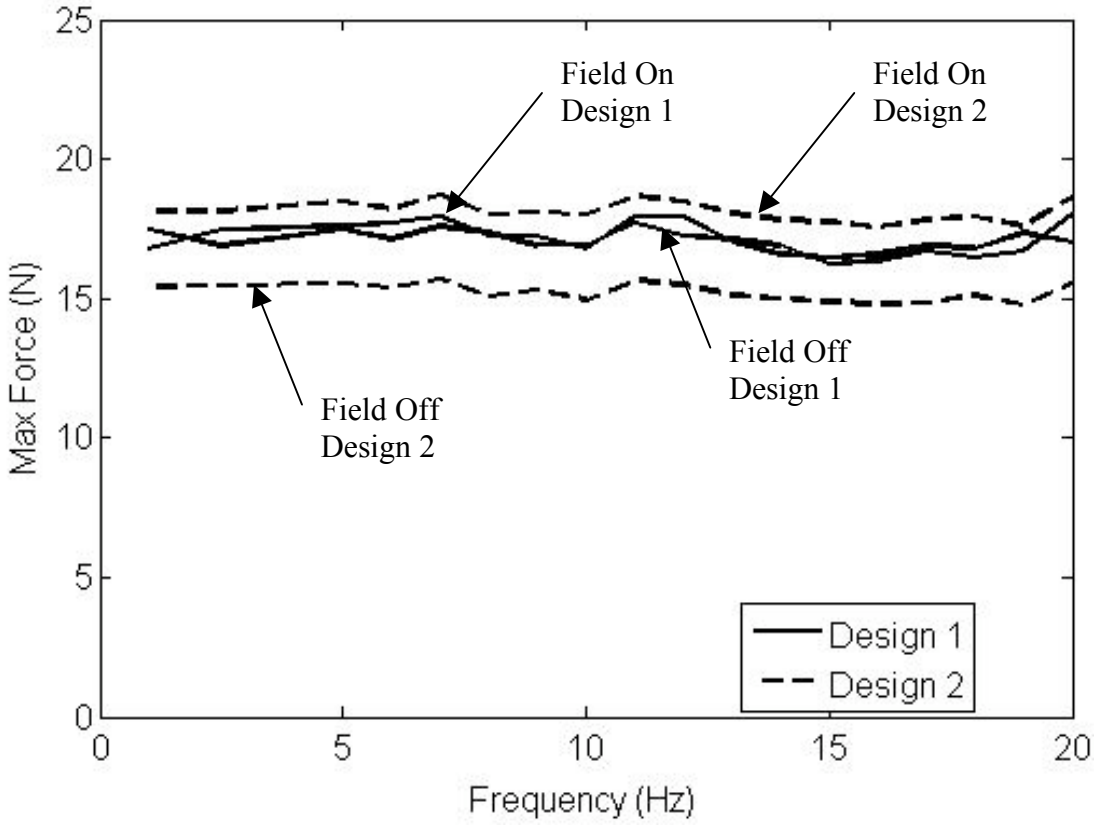

Figure 2.8 Maximum force versus frequency for designs 1 and 2 with 0 and 1.5 amperes applied current and a displacement amplitude of 0.25 mm.

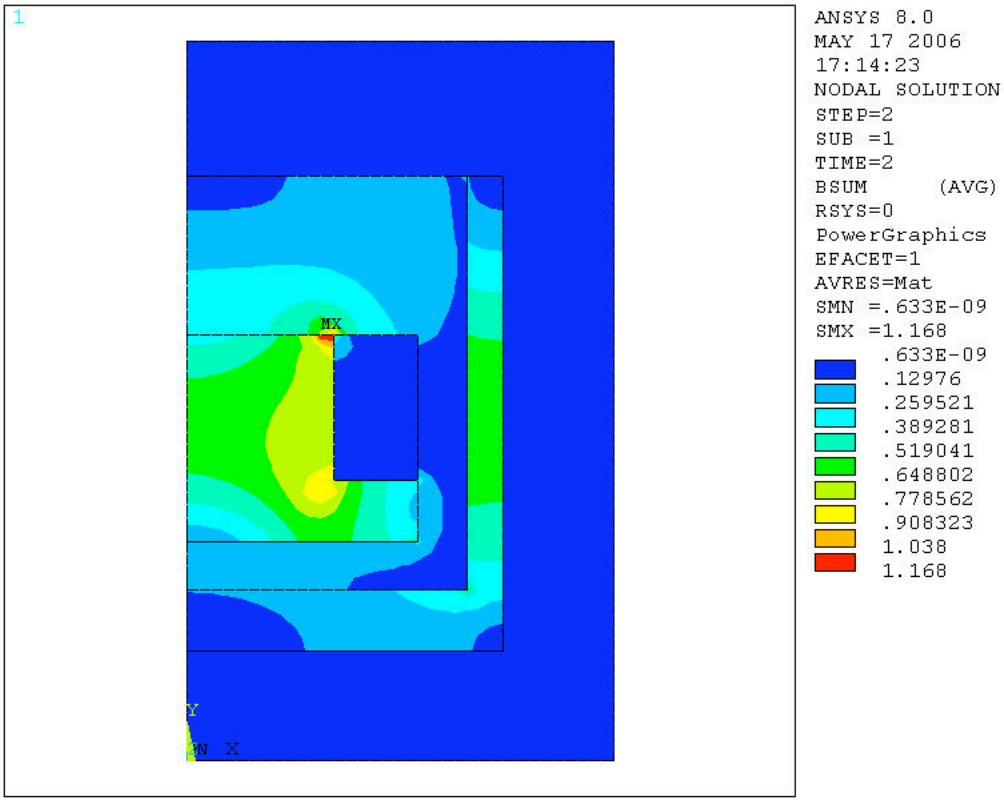

Figure 2.9 Magnetic analysis for design 3 using ANSYS for the bobbin installed disc side down.

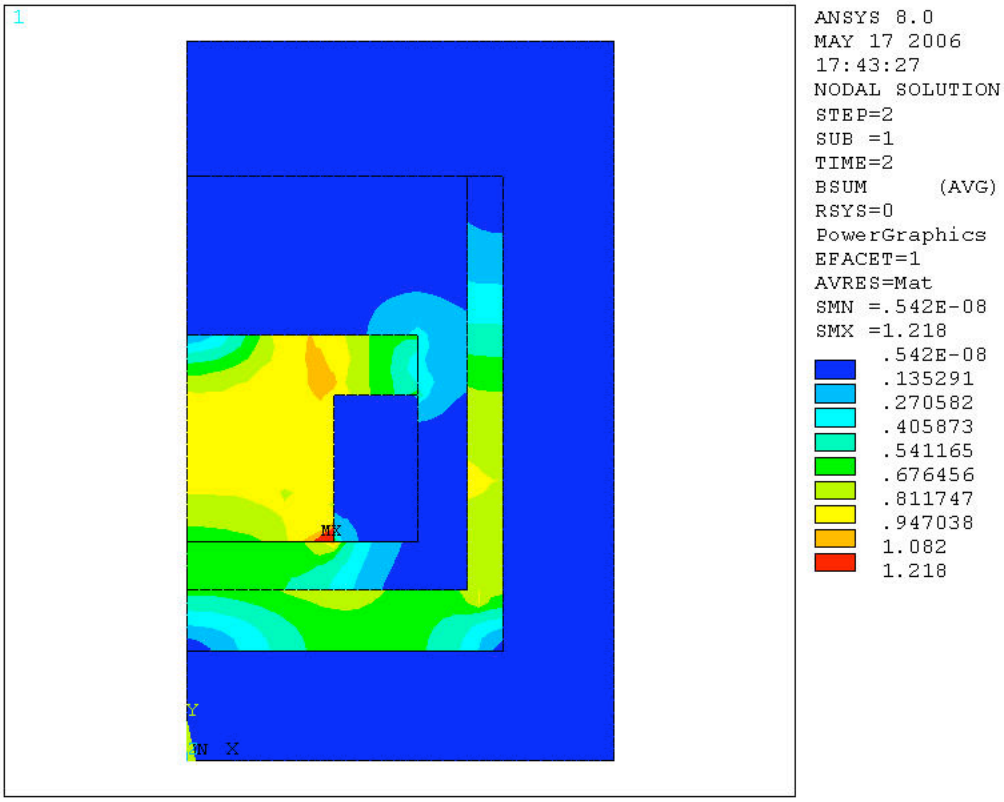

Figure 2.10 Magnetic analysis of design 3 using ANSYS for the bobbin installed disc side up.

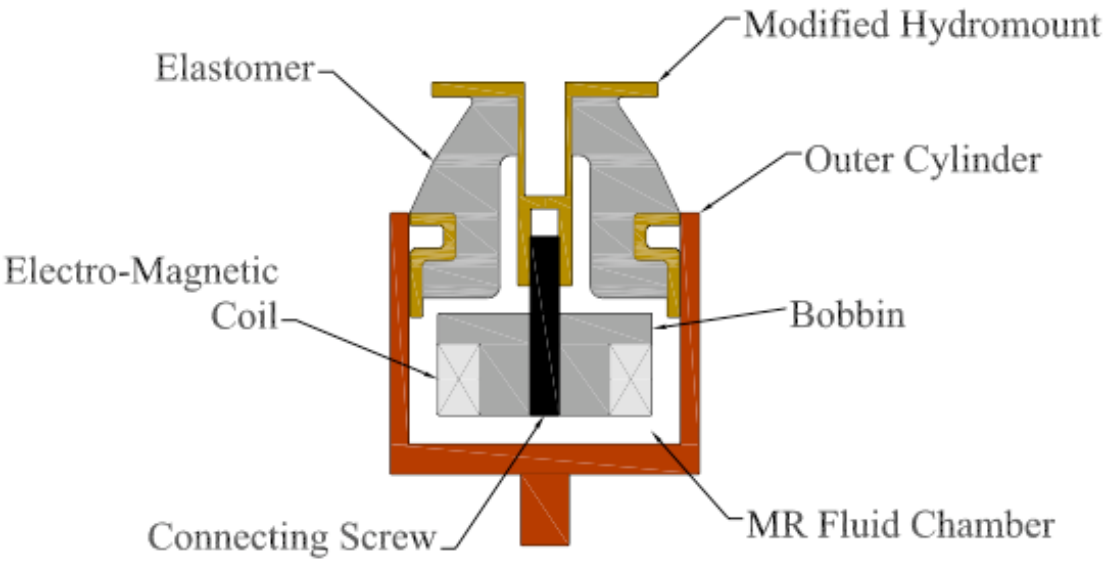

Figure 2.11 Sectional Drawing of Design 3

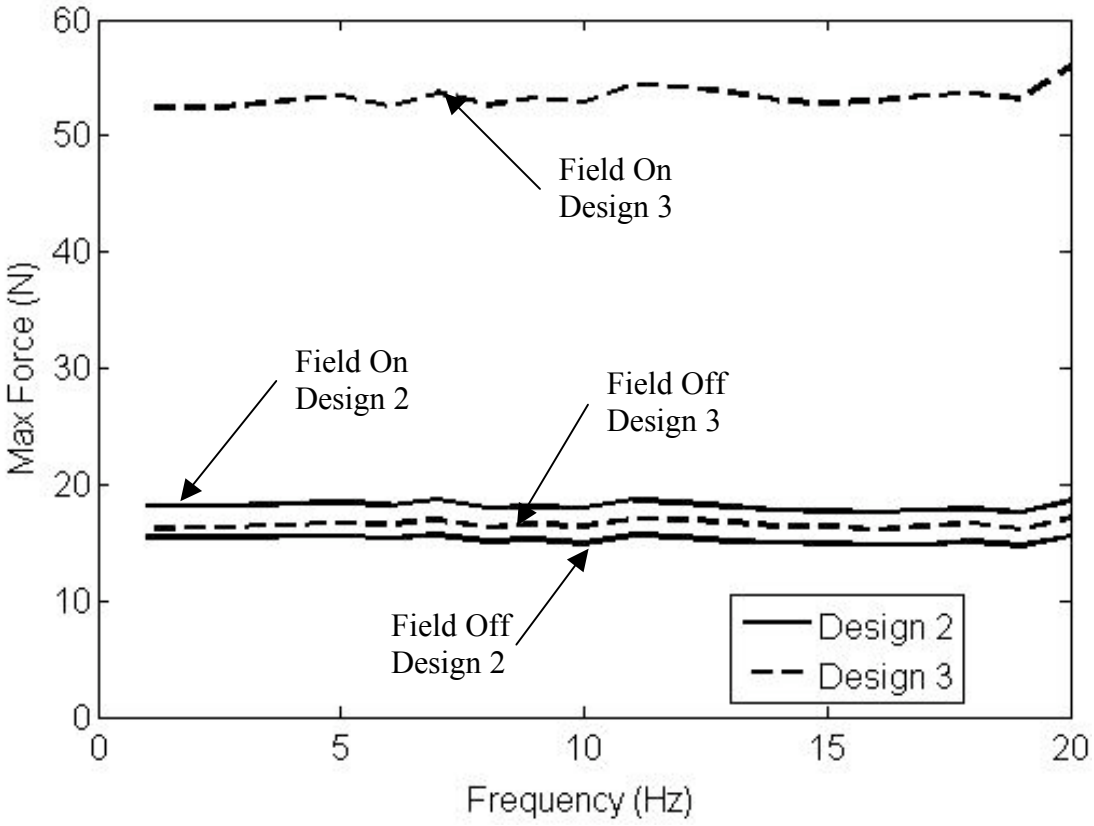

Figure 2.12 Maximum force versus frequency for designs 2 and 3 with 0 and 1.5 amperes applied current and a displacement amplitude of 0.25 mm.

Chapter 3: Testing and Characterization

For damper characterization, testing force measurements from sinusoidal displacement cycles were recorded using a hydraulically powered MTS model 661.22 load frame. The MTS system consists of a model 204.24 hydraulic actuator connected to a model 493.07 digital controller. The controller unit interfaces with testing software on a standard windows PC. The hydraulic actuator of the MTS system, shown in figure 3.1 with the MR damper mounted in the load frame, sinusoidally oscillates the base of the MR damper. Using an LVDT, which is integrated into the actuator shaft, the base displacement is measured. The resultant force due to oscillation is measured using a Honeywell, 100 lb. low-profile load cell, which was placed in series between the MR isolator and the MTS machines top hydraulic grip (also shown in figure 3.1).

A matrix of tests were conducted in order to characterize the damper. Testing included variations in frequency and amplitude of the applied displacement as well as the applied current to the MR isolator. These variations totaled 360 separate test conditions for the MR isolator. Oscillation frequency ranged from 5-20 Hz, in increments of 1 Hz as well as tests at 1 and 2.5 Hz. The oscillation amplitudes consisted of 0.1 mm, 0.25 mm, 0.5 mm, and 0.75 mm. The applied current ranged from 0-2 amperes, in increments of 0.5 amperes.

Scripts were written for the actuator control software in order to simplify the testing procedure. A separate script was written for each oscillation amplitude. There were 5 scripts in all. A script would sinusoidally oscillate the MR isolator with a fixed displacement amplitude at each frequency in sequence, collect force and displacement

data during the excitation and send it to a file. The testing procedure consisted of setting a value for the applied current to the MR isolator. Then each script would be run once—thus data would be collected for the entire range of frequencies and displacement amplitudes. Once this was complete a new value for current would be set and each script would be run again. This procedure allowed all of the characterization data to be taken in one sitting. As a result irregularities between separate tests were avoided. The text formatted multiple data files resulting from the testing procedure made post processing of the data in Matlab an efficient procedure.

3.1 Damper Characterization

The force and displacement data collected during each experiment were periodic as the independent displacement variable was sinusoidal. This made it possible to fit the displacement data with a periodic Fourier series. Through differentiations of the Fourier-fit signal, it is possible to construct a velocity signal without the use of finite difference methods. This is useful, as finite difference methods tend to accentuate noise present in the displacement signal. When possible, the measured force data was used because the damper response is nonlinear and it is not known a priori which harmonics contributed to the response. The Fourier series of the displacement is given as [18]

$$x(t) = \frac{x_0}{2} + \sum_{k=1}^{\infty}\left(x_{c,k}\cos k\omega t + x_{s,k}\sin k\omega t\right) \qquad (3.1)$$

where

$$x_{c,k} = \frac{\omega}{\pi k} \int_0^{2\pi k/\omega} x(t) \cos k\omega t dt$$
$$x_{s,k} = \frac{\omega}{\pi k} \int_0^{2\pi k/\omega} x(t) \sin k\omega t dt \qquad (3.2)$$

The higher harmonics and bias are filtered out, only the harmonics of the displacement frequency, ω, are retained. Thus the reconstructed displacement signal is [18]

$$x(t) = X_c \cos \omega t + X_s \sin \omega t \qquad (3.3)$$

Differentiation of (3.3) yields the velocity signal

$$\dot{x}(t) = -\omega X_c \sin \omega t + \omega X_s \cos \omega t \qquad (3.4)$$

Using the reconstructed displacement and velocity signals plots of MR damper force versus displacement and MR damper force vs velocity were created. Figure 3.2 shows a force-displacement plot for a 5 Hz oscillation frequency and 0.5 mm displacement amplitude. The applied currents to the MR isolator consisted of 0,1 and 2 A. With increasing current the area enclosed by the force-displacement plot increased, signifying an increase in damping. The force-displacement plot was also rotated counter clockwise as current increased, signifying an increase in isolator stiffness. Figure 3.3 shows a force-velocity plot for the same conditions. In the case when current is not applied to the MR isolator (zero field) the hysteresis plot is elliptical in shape, typical of a purely viscous damper. Upon application of current the hysteresis plots deviate from this elliptical behavior and exhibit trends consistent with the addition of a yield force as large variations in force are observed at high displacement amplitudes or upon a change in sign of velocity.

Two common approaches, equivalent viscous damping and complex stiffness, are used to characterize damper behavior [17]. Equivalent viscous damping uses the force-displacement data and equates the energy dissipated by the MR damper over a single cycle to that of a purely viscous damper. The second approach uses a complex modulus, K^*. A Fourier analysis is used to characterize the in-phase (storage stiffness) component of force and the quadrature component of the force (damper force).

3.1.1 Equivalent Viscous Damping

The first characterization technique is that of equivalent viscous damping. This is a standard linearization technique that can be applied to a nonlinear damper to find an equivalent viscous damping force proportional to velocity. This damping force, $f_d(t)$, is given as [17]

$$f_d(t) = C_{eq}\dot{x}(t) \tag{3.5}$$

The equivalent viscous damping, C_{eq}, is computed by equating the energy dissipated over a single cycle, E, at a given frequency, ω. The expression for the energy dissipated per cycle of vibration is of the form [17]

$$E = \int_{cycle} F dx = \int_{0}^{2\pi/\omega} F\dot{x} dt \tag{3.6}$$

For a viscous damper the dissipated energy is found to be of the form [17]

$$E = C_{eq}\pi\omega X^2 \tag{3.7}$$

Equating energies gives an equation for C_{eq} of the following

$$C_{eq} = \frac{E}{\pi \omega X^2} \tag{3.8}$$

The equivalent viscous damping was calculated for each test run using the above methods. Figure 3.4 shows equivalent damping versus amplitude of sinusoidal excitation, ranging from 0.1 to 0.75mm at a frequency of 5 Hz. The equivalent damping coefficient decreases with increasing displacement amplitude. For zero field the damping coefficient is seen to vary only slightly with amplitude. Figures 3.5-3.8 show equivalent damping versus frequency for displacement amplitudes of 0.1mm, 0.25 mm, 0.5 mm and 0.75 mm respectively. As is evident from these plots, the equivalent damping is strongly dependent on the oscillation frequency of excitation as the damping decreases over this range. Again, at zero field the damping does not vary greatly over the frequency range tested in comparison to the cases when there is current applied to the MR isolator.

3.1.2 Complex Stiffness

The second characterization technique is the complex stiffness approach. This is a linearization technique in the frequency domain, which replaces the nonlinear hysteresis loop with an equivalent ellipse. In this approach the complex damper stiffness, K^*, is characterized as an in-phase or storage stiffness, K', which is a measure of the energy stored over a cycle and a quadrature stiffness, K'', which is a measure of the energy dissipated over a period. This model can be represented as the Kelvin chain (a spring and viscous damper in parallel). The complex stiffness is expressed as

$$K^* = K' + jK'' = K'(1 + j\eta) \tag{3.9}$$

where η is the loss factor. Alternatively, K' is the equivalent stiffness and K'' is related to the equivalent viscous damping in an approximate way by

$$C_{eq} = \frac{K''}{\omega} \tag{3.10}$$

This relation is only approximate because the complex stiffness considers only the harmonic of the displacement frequency, ω, as is shown below. To find expressions for the storage stiffness and quadrature stiffness, the damper force is reconstructed as a Fourier series

$$\begin{aligned} f(t) &= F_c \cos(\omega t) + F_s \sin(\omega t) \\ &= K' x(t) + \frac{K''}{\omega} \dot{x}(t) \end{aligned} \tag{3.11}$$

Where F_c and F_s are the cosine and sine Fourier coefficients of $f(t)$ at frequency ω.

$$\begin{aligned} F_c &= \frac{\omega}{\pi} \int_0^{2\pi/\omega} f(t) \cos \omega t dt \\ F_s &= \frac{\omega}{\pi} \int_0^{2\pi/\omega} f(t) \sin \omega t dt \end{aligned} \tag{3.12}$$

The sinusoidal displacement, $x(t)$, is given by equation (3.3). Substituting (3.3) into the force equation (3.11) and equating the sine and cosine terms yields expressions for the storage stiffness as well as the quadrature stiffness

$$\begin{aligned} K' &= \frac{F_c X_c + F_s X_s}{X_c^2 + X_s^2} \\ K'' &= \frac{F_c X_s + F_s X_c}{X_c^2 + X_s^2} \end{aligned} \tag{3.13}$$

The storage stiffness, quadrature stiffness and loss factor were calculated for each test run using the above methods. Figure 3.9 is a plot of storage stiffness versus displacement amplitude at 5 Hz frequency. Figures 3.10-3.13 show how the storage stiffness varies with frequency for displacement amplitudes of 0.1 mm, 0.25 mm, 0.5 mm and 0.75 mm, respectively. It can be seen that storage stiffness decreases with increasing displacement amplitude. Similarly, storage stiffness decreases with increasing frequency. The storage stiffness showed significant increases when the magnetic fields in the MR isolator were activated. At the lowest displacement amplitude of 0.1mm this increase was over 200 N/mm. At the highest displacement amplitude the MR effect was less pronounced as an increase of 30 N/mm was found.

The quadrature stiffness was found to decrease with increasing displacement amplitude, this is seen in figure 3.14. Figures 3.15-3.18 show how quadrature stiffness varies with frequency for displacement amplitudes of 0.1 mm, 0.25 mm, 0.5 mm and 0.75 mm. In each case the quadrature stiffness increased with increasing frequency.

The loss factor is a ratio of quadrature stiffness to storage stiffness; generally it is desired to have a high loss factor over a wide range of displacement amplitudes. In figure 3.19 the loss factor increases over the entire range of amplitudes upon application of current. At zero field the loss factor is found to be around 0.2. However, at 2 A of applied current, the maximum current tested, the loss factor is increased to over 1. Over the frequency spectrum the quadrature stiffness increases while the storage stiffness decreases with increasing frequency. This trend is evident

in figures 3.20-3.23; the loss factor increases with frequency for each of the tested displacement amplitudes.

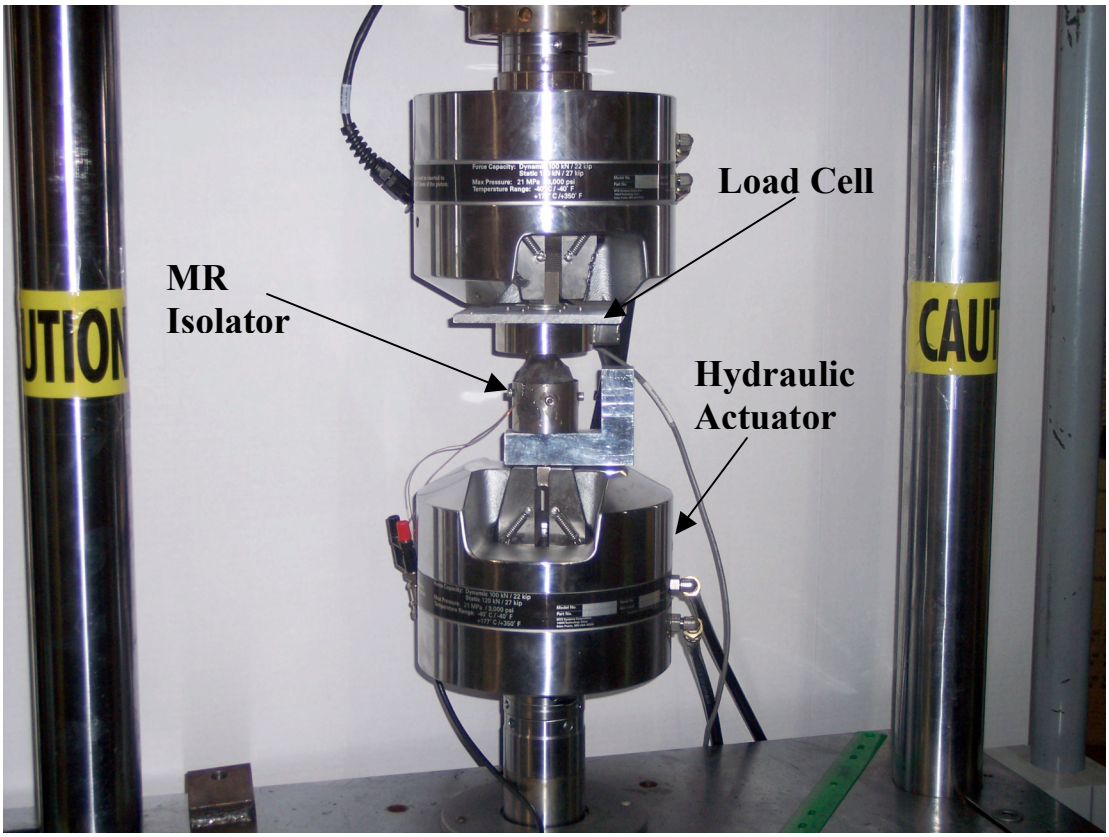

Figure 3.1 MR isolator in the MTS machine for sinusoidal testing

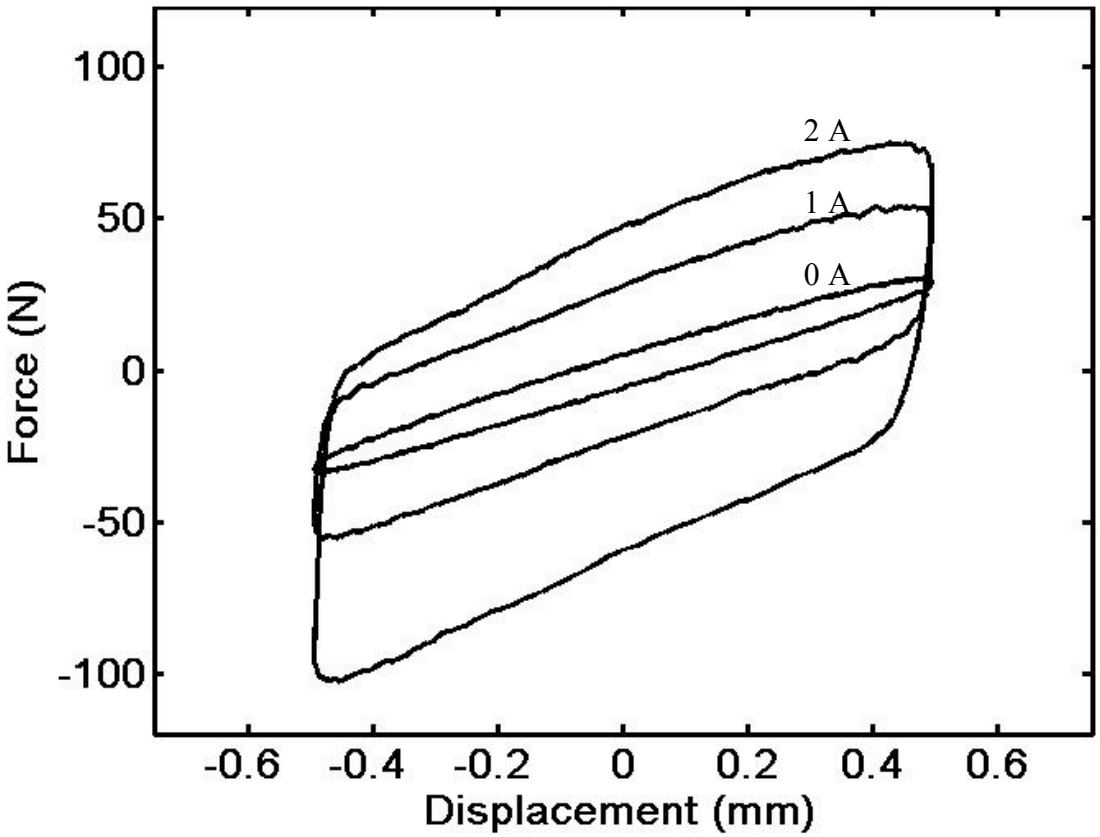

Figure 3.2 Experimental force vs displacement for excitation frequency of 5 Hz, displacement amplitude of 0.5mm and applied electric fields of 0 A, 1 A and 2 A.

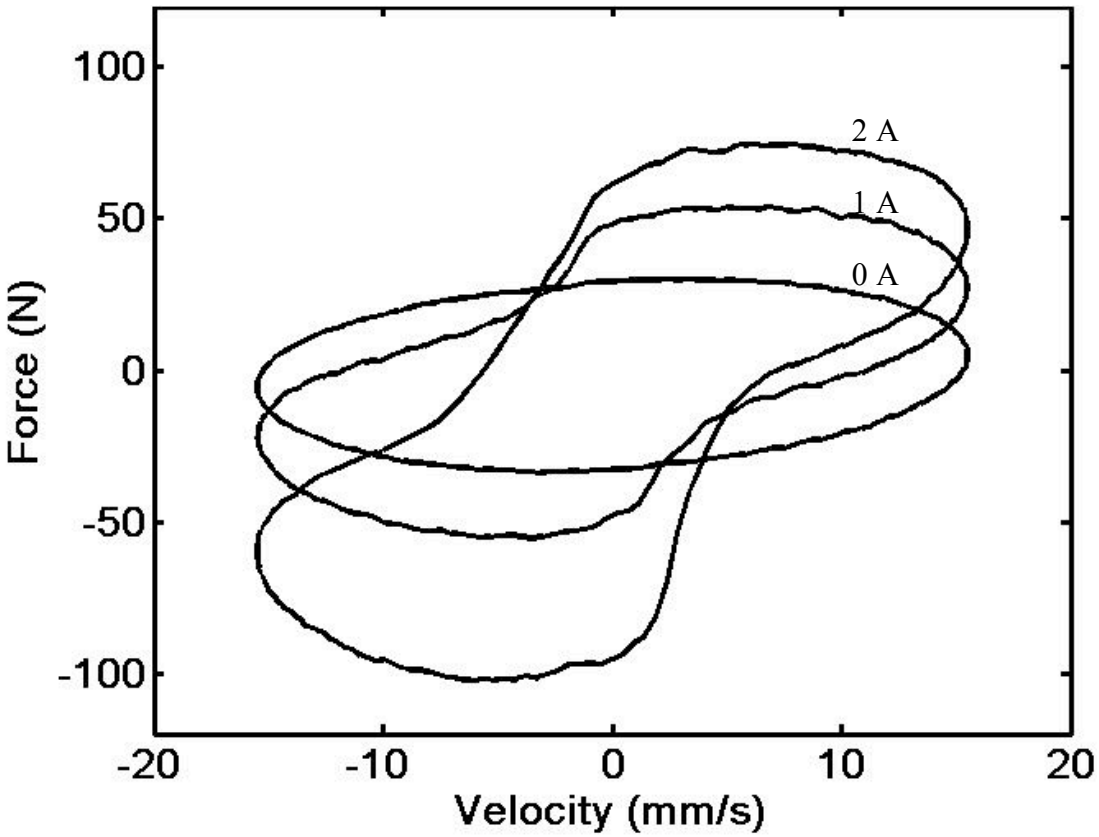

Figure 3.3 Experimental force vs velocity for excitation frequency of 5 Hz, displacement amplitude of 0.5mm and applied electric fields of 0 A, 1 A and 2 A.

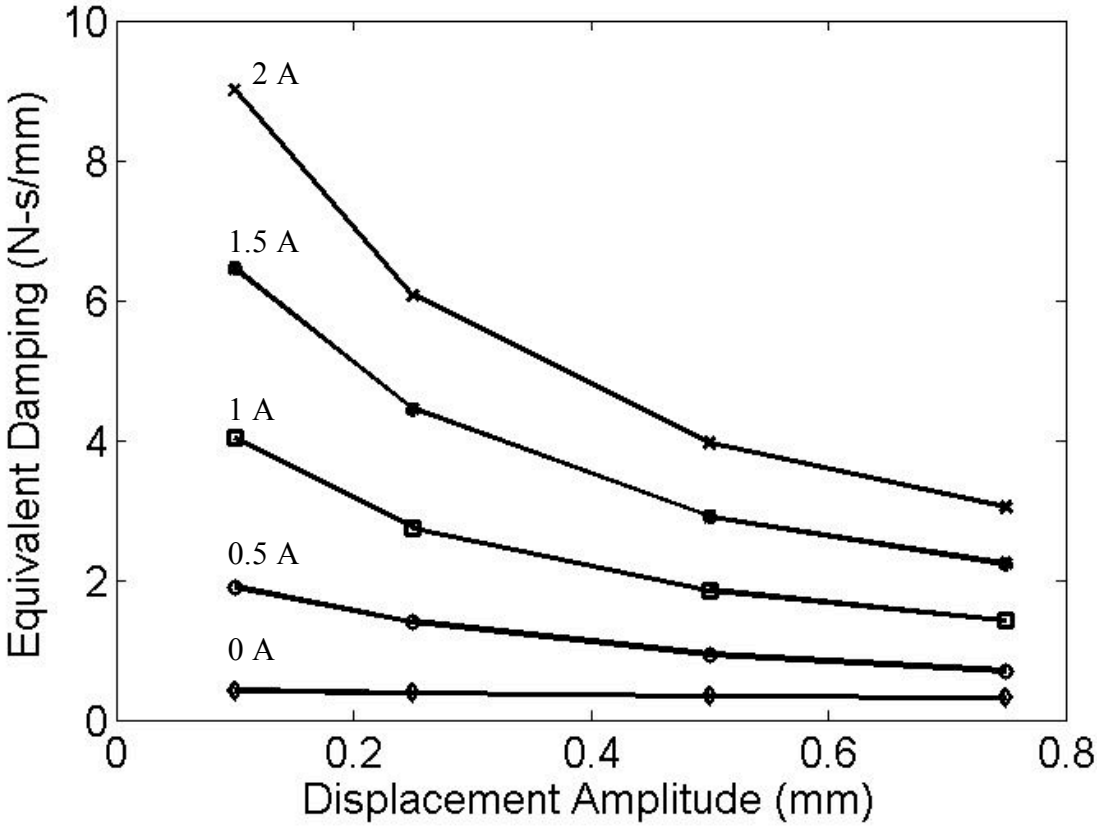

Figure 3.4 Experimental equivalent damping coefficient versus displacement amplitude for excitation frequency of 5 Hz and varying applied current.

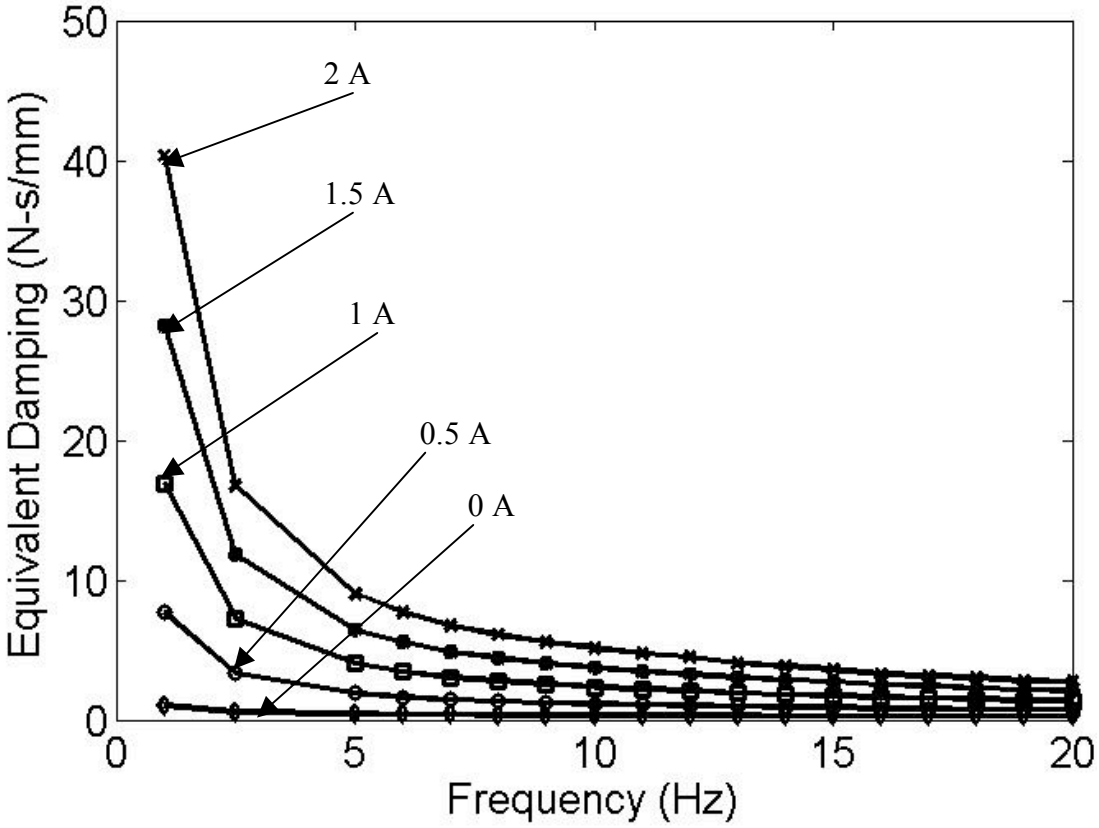

Figure 3.5 Experimental equivalent damping coefficient versus frequency for displacement amplitude of 0.1 mm and varying applied current

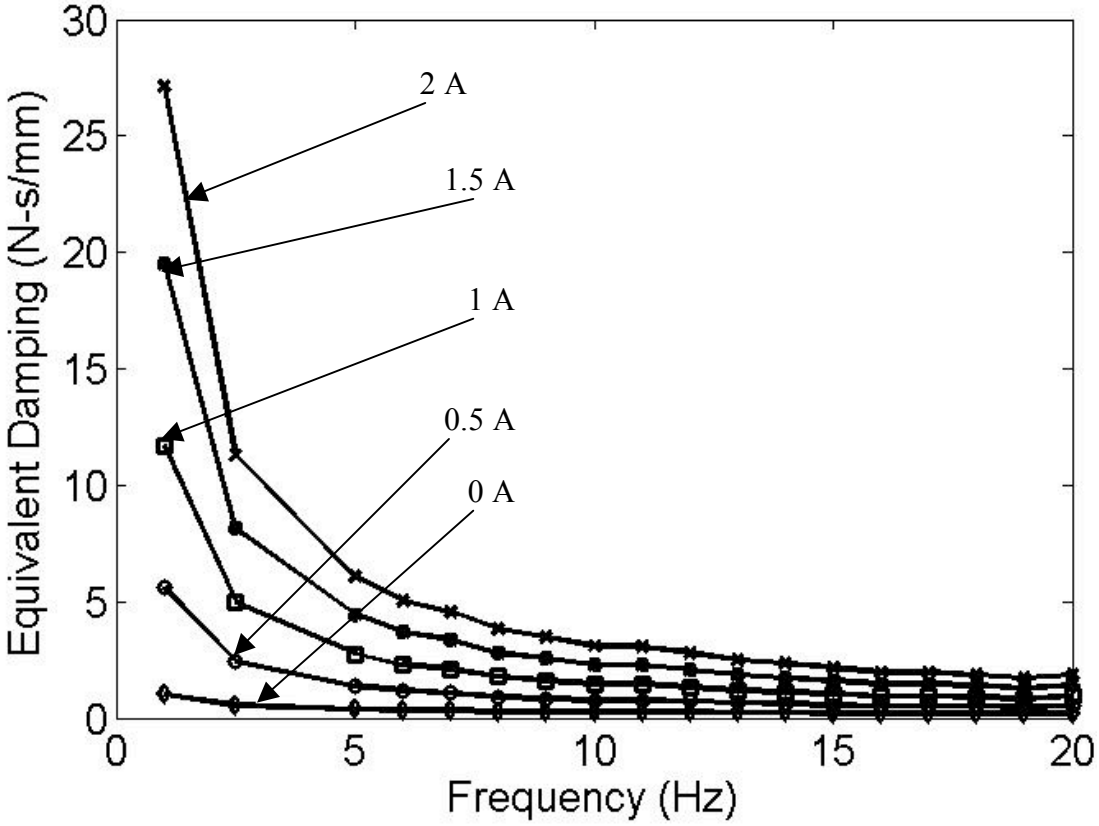

Figure 3.6 Experimental equivalent damping coefficient versus frequency for displacement amplitude of 0.25 mm and varying applied current

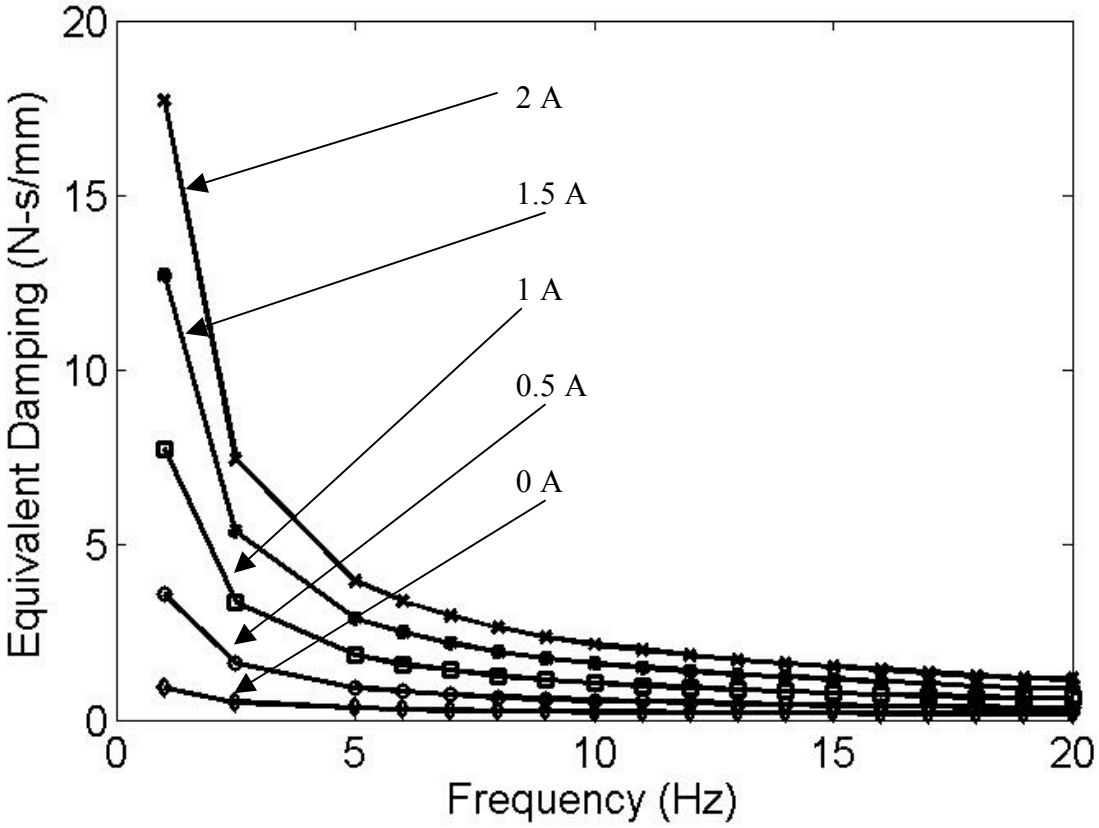

Figure 3.7 Experimental equivalent damping coefficient versus frequency for displacement amplitude of 0.5 mm and varying applied current

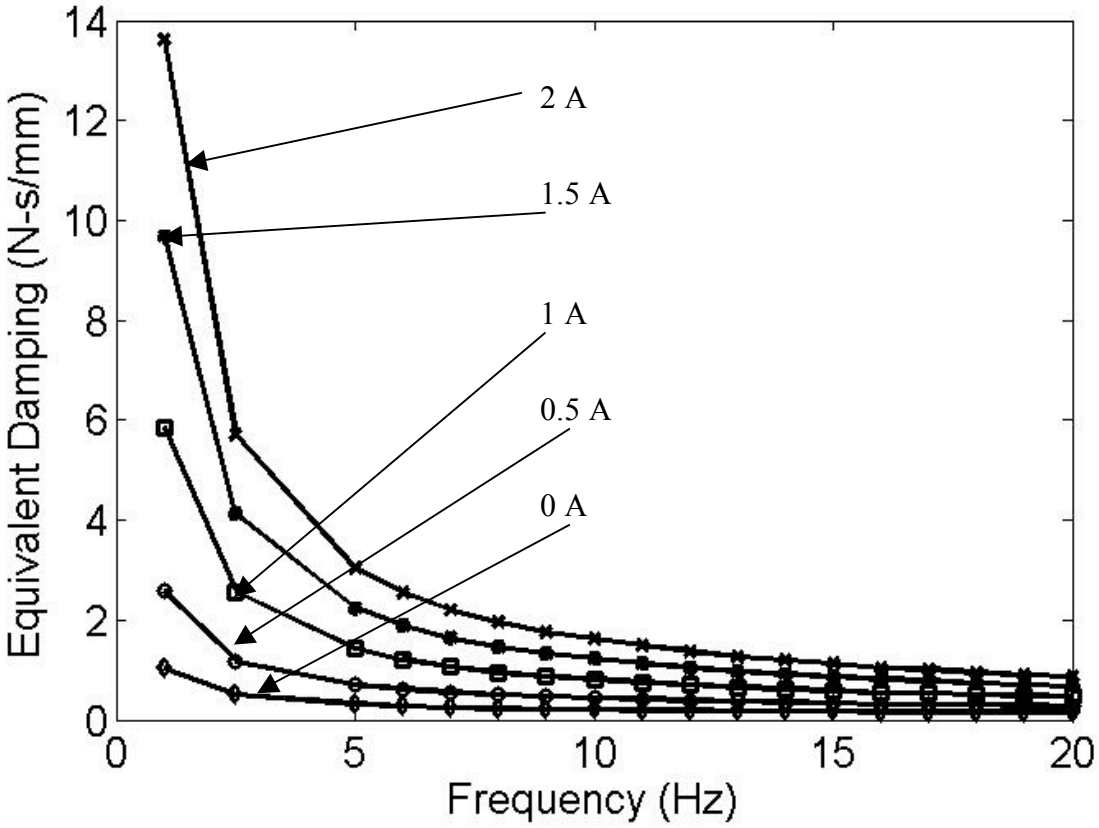

Figure 3.8 Experimental equivalent damping coefficient versus frequency for displacement amplitude of 0.75 mm and varying applied current

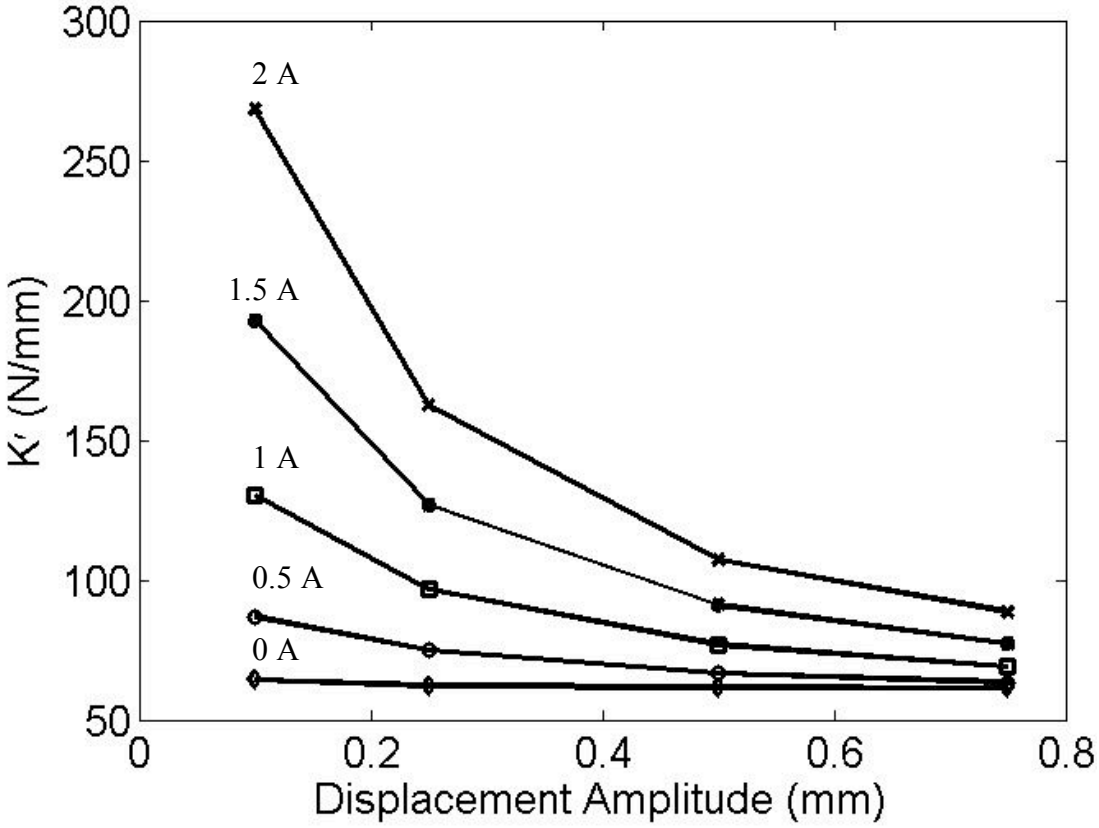

Figure 3.9 Experimental storage stiffness versus displacement amplitude for excitation frequency of 5 Hz and varying applied current

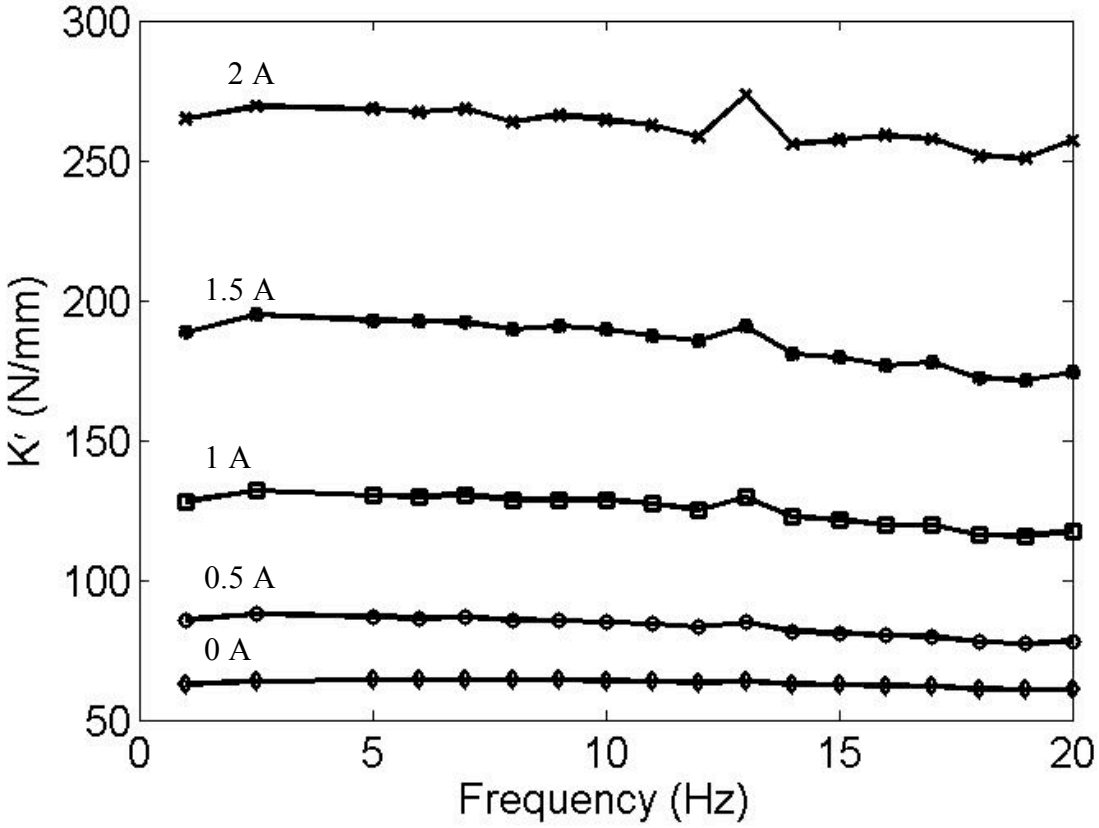

Figure 3.10 Experimental storage stiffness versus frequency for displacement amplitude of 0.1 mm and varying applied current

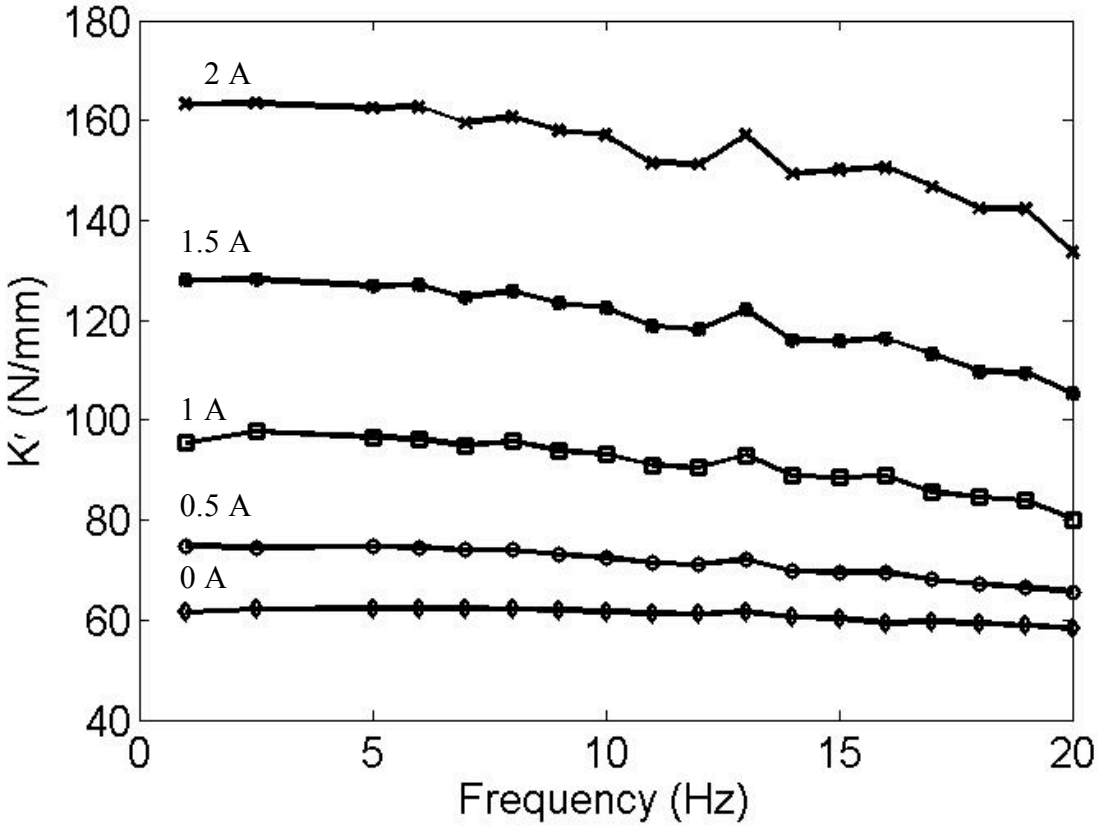

Figure 3.11 Experimental storage stiffness versus frequency for displacement amplitude of 0.25 mm and varying applied current

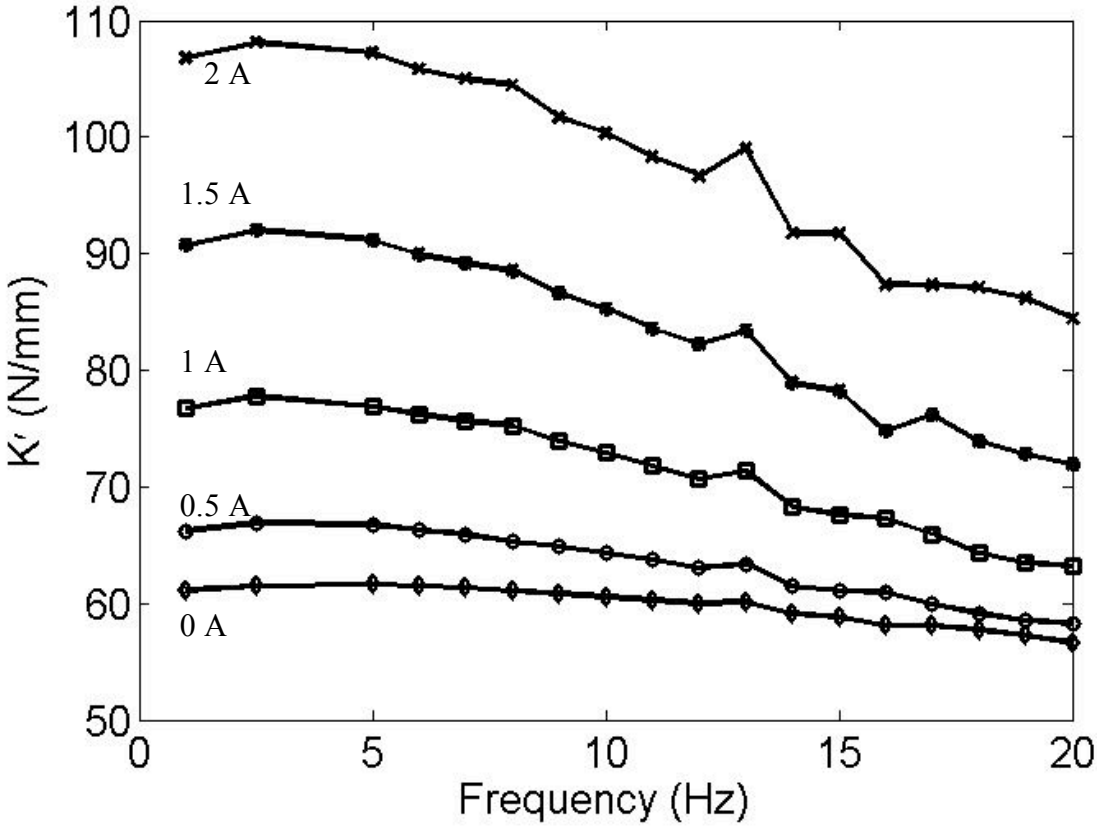

Figure 3.12 Experimental storage stiffness versus frequency for displacement amplitude of 0.5 mm and varying applied current

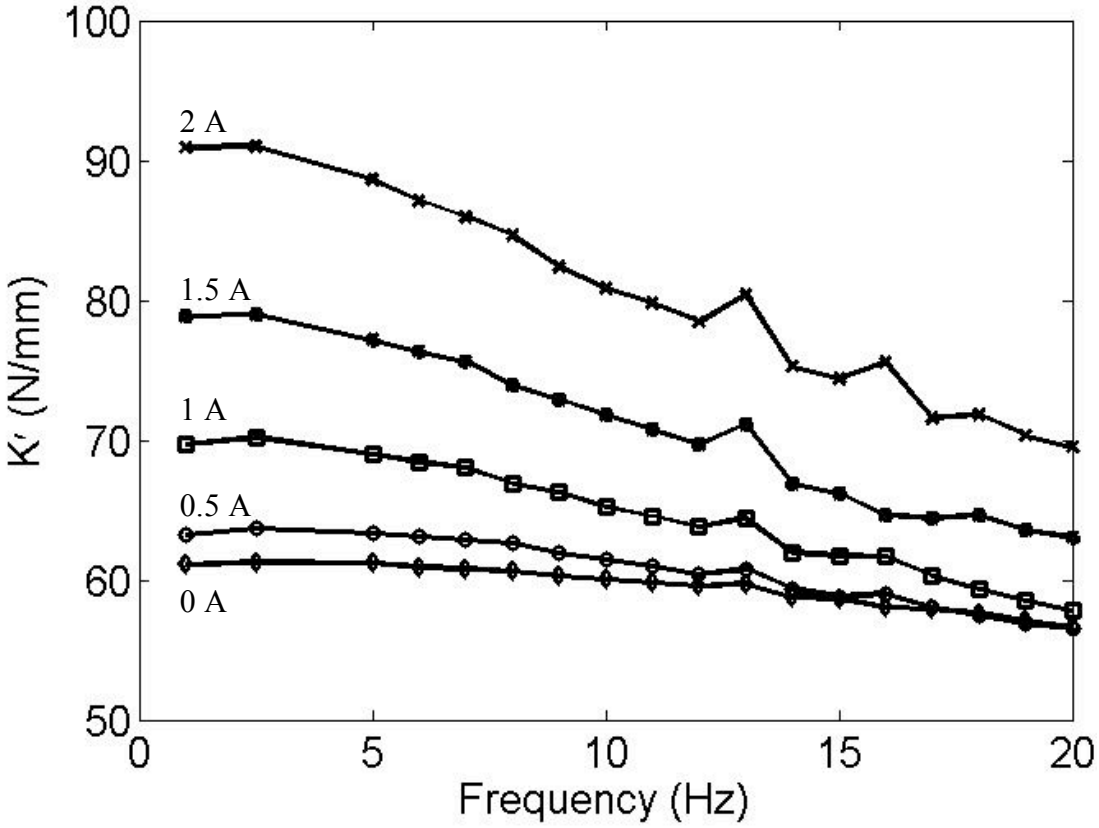

Figure 3.13 Experimental storage stiffness versus frequency for displacement amplitude of 0.75 mm and varying applied current

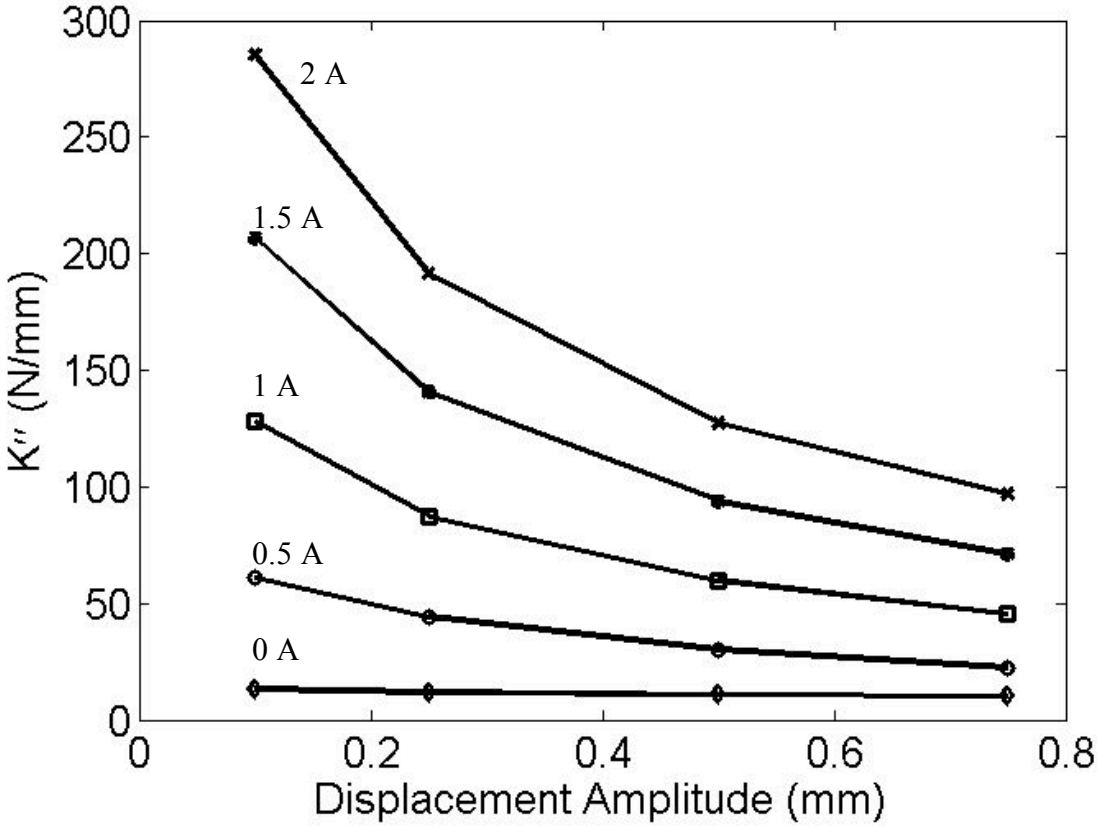

Figure 3.14 Experimental quadrature stiffness versus displacement amplitude for an excitation frequency of 5 Hz and varying applied current

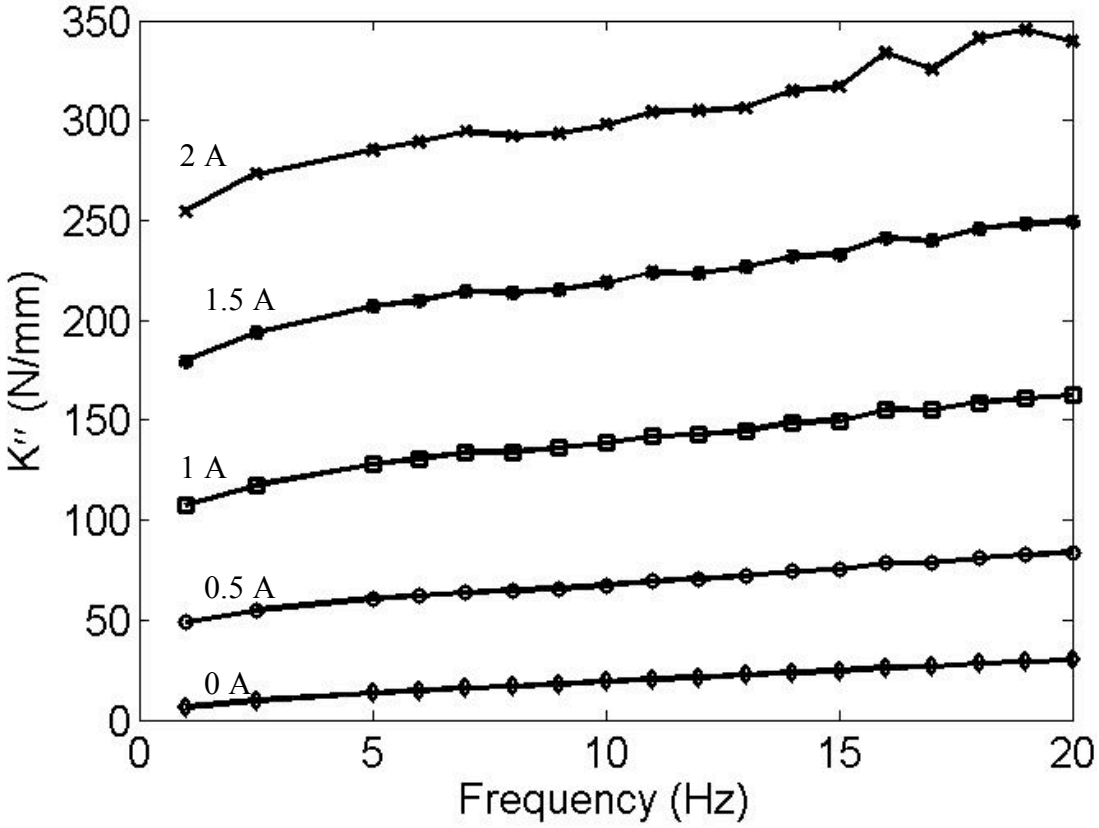

Figure 3.15 Experimental quadrature stiffness versus frequency for displacement amplitude of 0.1 mm and varying applied current

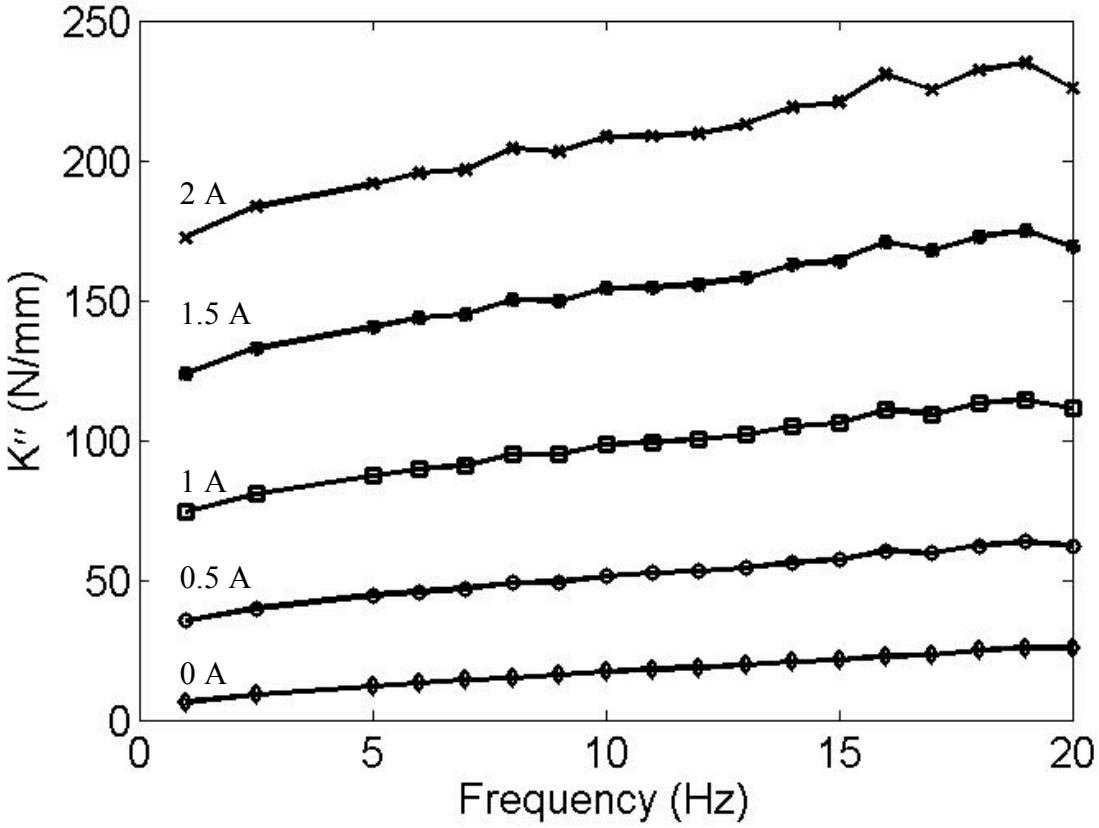

Figure 3.16 Experimental quadrature stiffness versus frequency for displacement amplitude of 0.25 mm and varying applied current

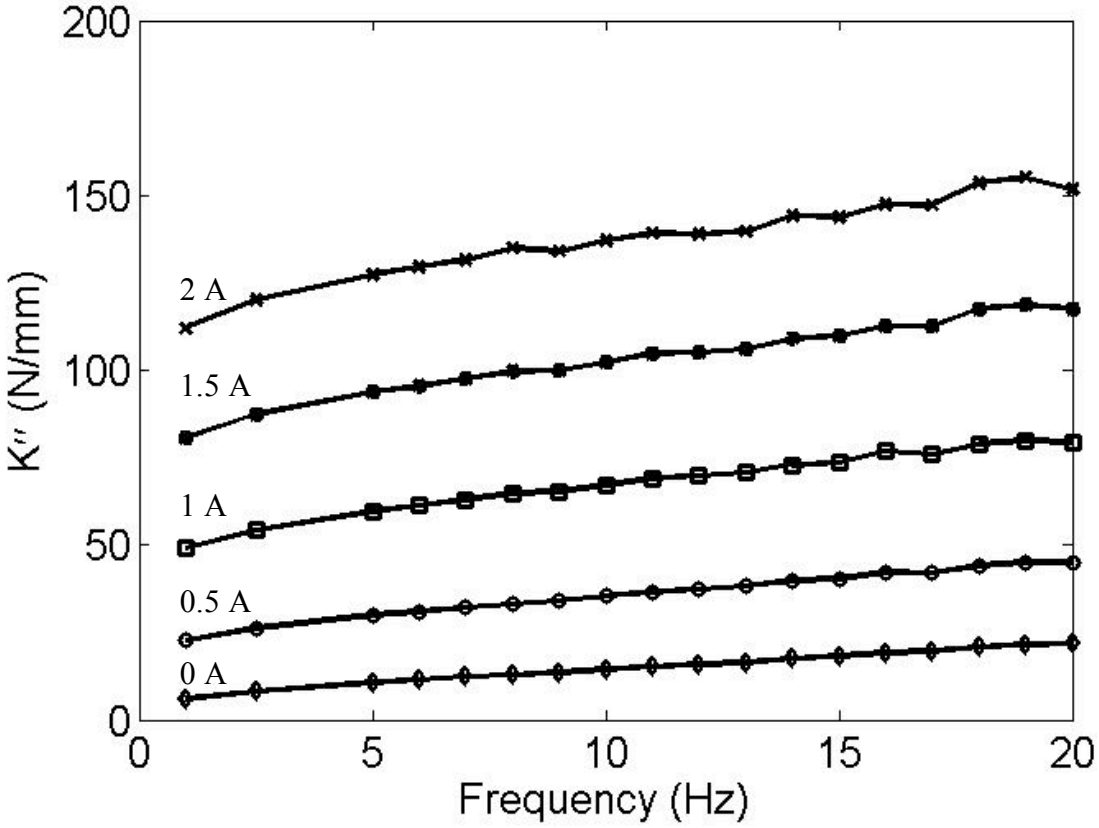

Figure 3.17 Experimental quadrature stiffness versus frequency for displacement amplitude of 0.5 mm and varying applied current

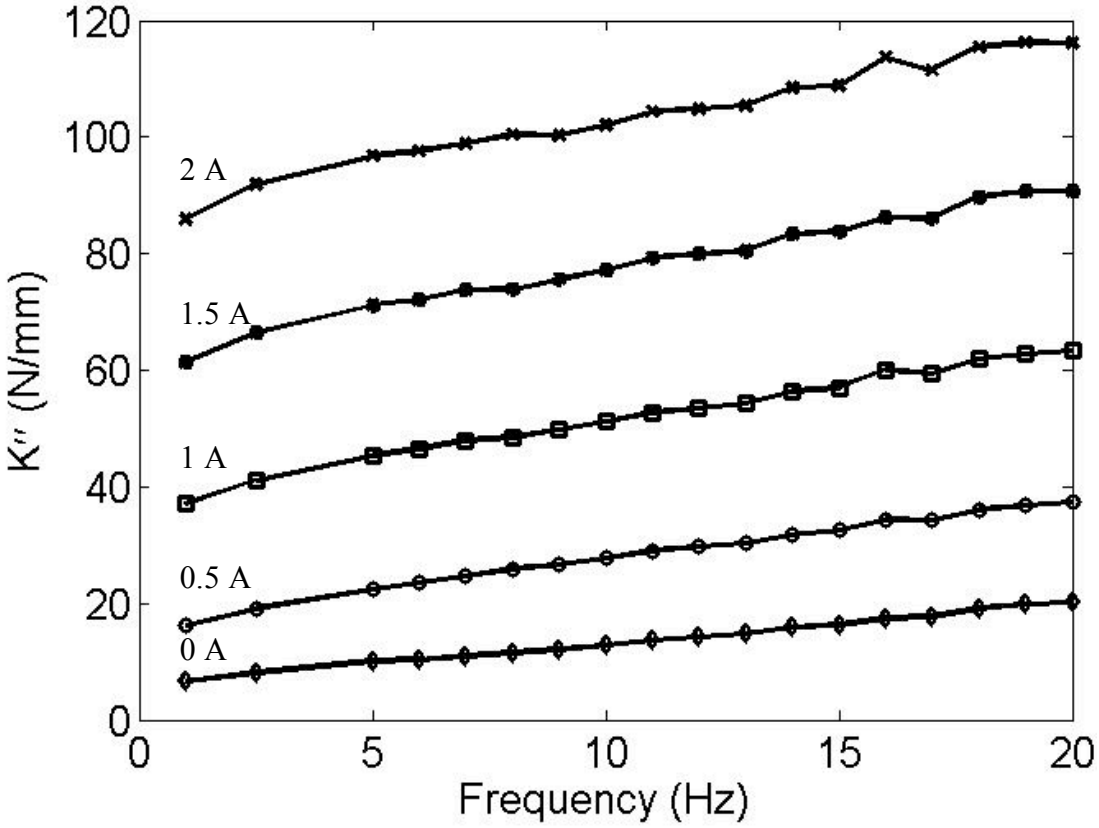

Figure 3.18 Experimental quadrature stiffness versus frequency for displacement amplitude of 0.75 mm and varying applied current

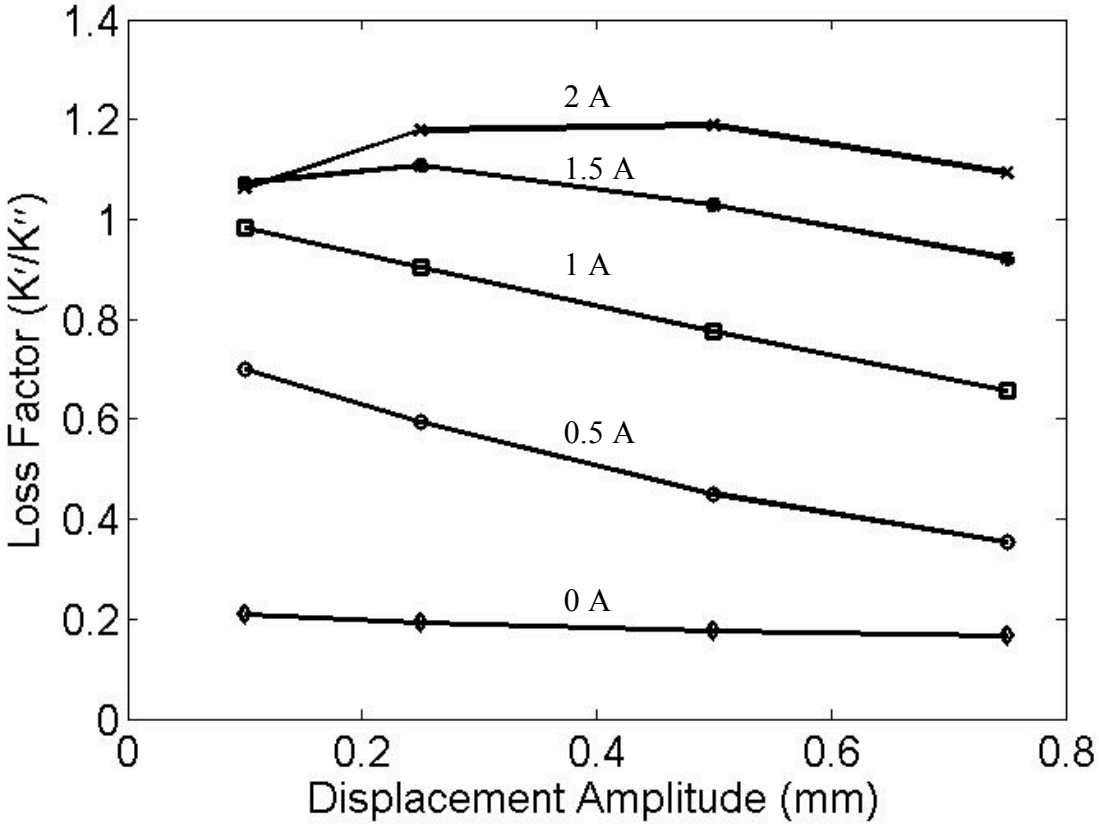

Figure 3.19 Experimental loss factor versus displacement Amplitude for excitation frequency of 5 Hz and varying applied current

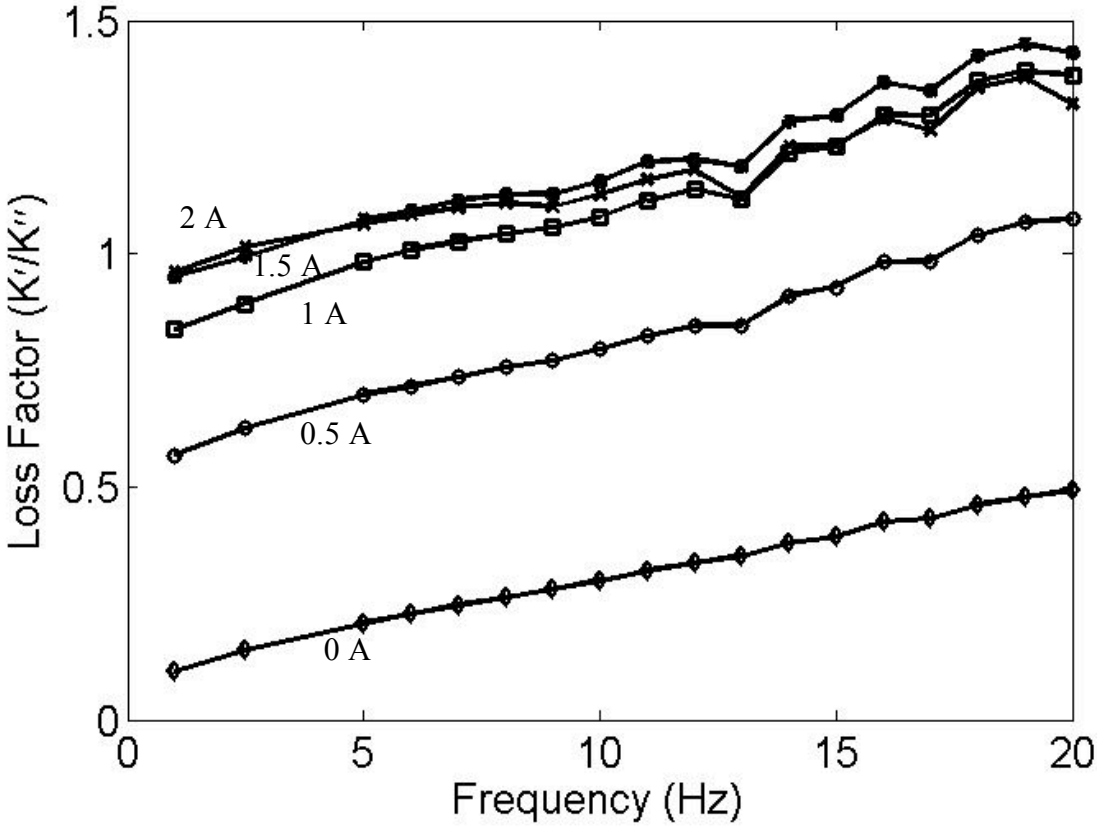

Figure 3.20 Experimental loss factor versus frequency for displacement amplitude of 0.1 mm and varying applied current

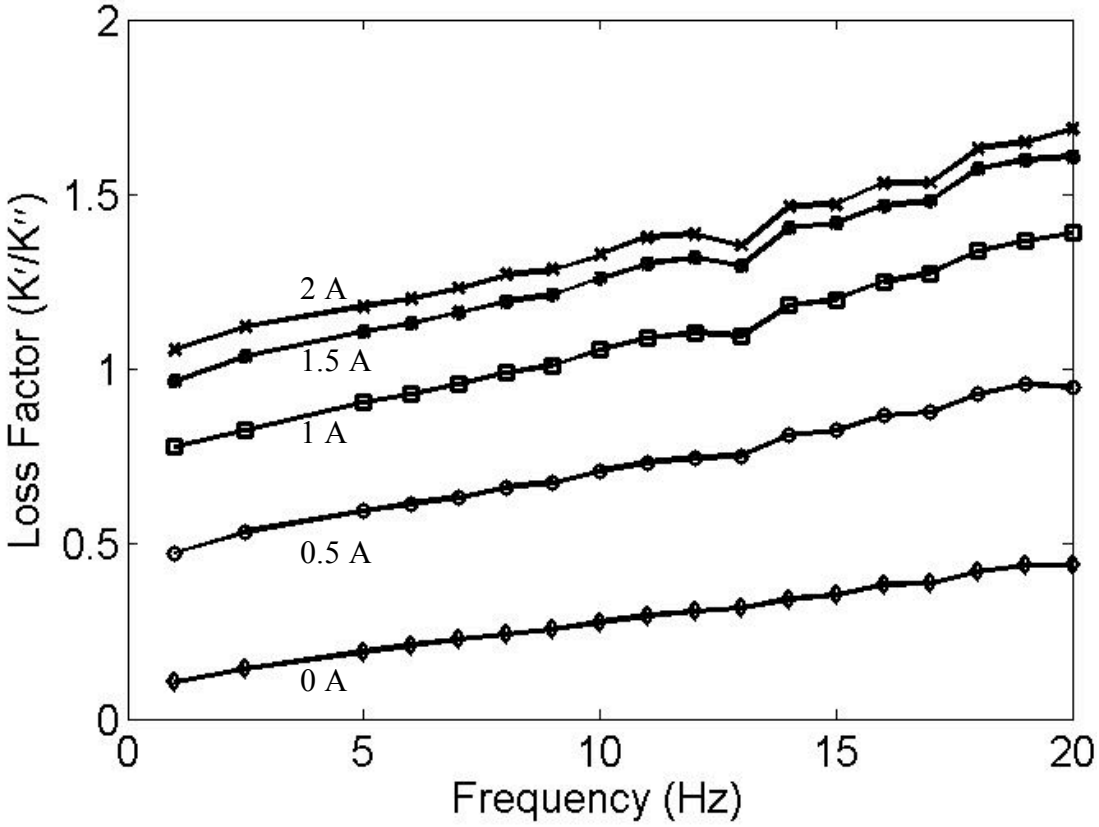

Figure 3.21 Experimental loss factor versus frequency for displacement amplitude of 0.25 mm and varying current

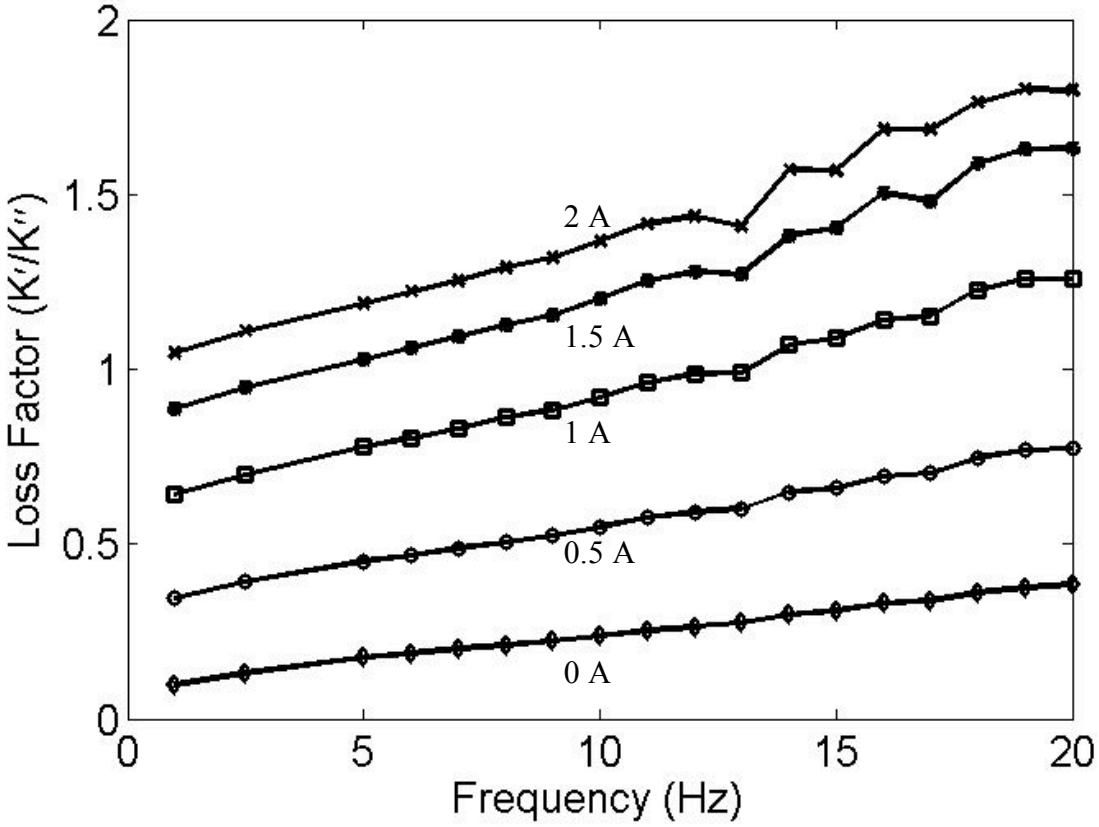

Figure 3.22 Experimental loss factor versus frequency for displacement amplitude of 0.5 mm and varying current

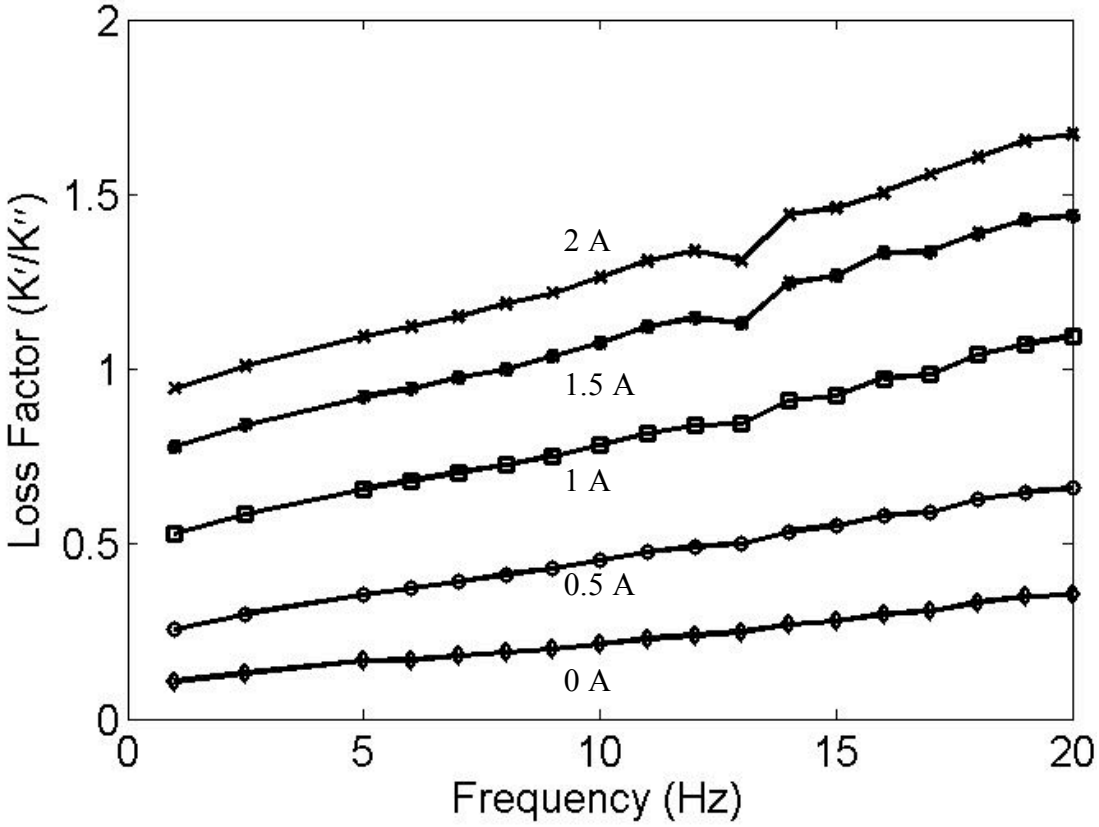

Figure 3.23 Experimental loss factor versus frequency for displacement amplitude of 0.75 mm and varying current

Chapter 4: Bingham Isolator Model

The constitutive model for the MR isolator used in this project is that of the Bingham plastic model with additional stiffness and damping terms, which were included to account for the elastic behavior as well as the elastomeric damping of the MR isolator. The Bingham model describes the shear stress in the fluid as a combination of a yield stress term and a flow term with a constant viscosity. As discussed in section 1.3, this model assumes quasi-steady flow. Also, the pre-yield regime is not accounted for making this model less suitable for dynamic purposes. Beginning with the Bingham relation for the shear stress in the fluid, it is possible to build a relation between the forces exerted by the MR isolator given a prescribed motion.

The models developed for the isolator force use the parallel plate approximation in the areas that have an axisymmetric geometry. This approximation has been shown to be valid when the annular gap is small in comparison with its radius [8].

The MR damper has two regions of fluid flow resulting from axial motion of the bobbin. In the gap between the bottom of the bobbin and the bottom of the outer cylinder, motion of the bobbin compresses the fluid and flow in the radial direction results. This region behaves as a squeeze-mode damper. In the annulus between the side of the bobbin and the walls of the outer cylinder fluid flow is imposed by a combination of (1) a pressure differential developed through the annulus due to motion of the bobbin and (2) a direct shearing of the fluid as the bobbin moves relative to the outer cylinder. This region behaves as a combination shear and flow

mode damper. Figure 4.1 depicts the bobbin of design 3 and defines some of the geometric parameters used in the model of the MR isolator.

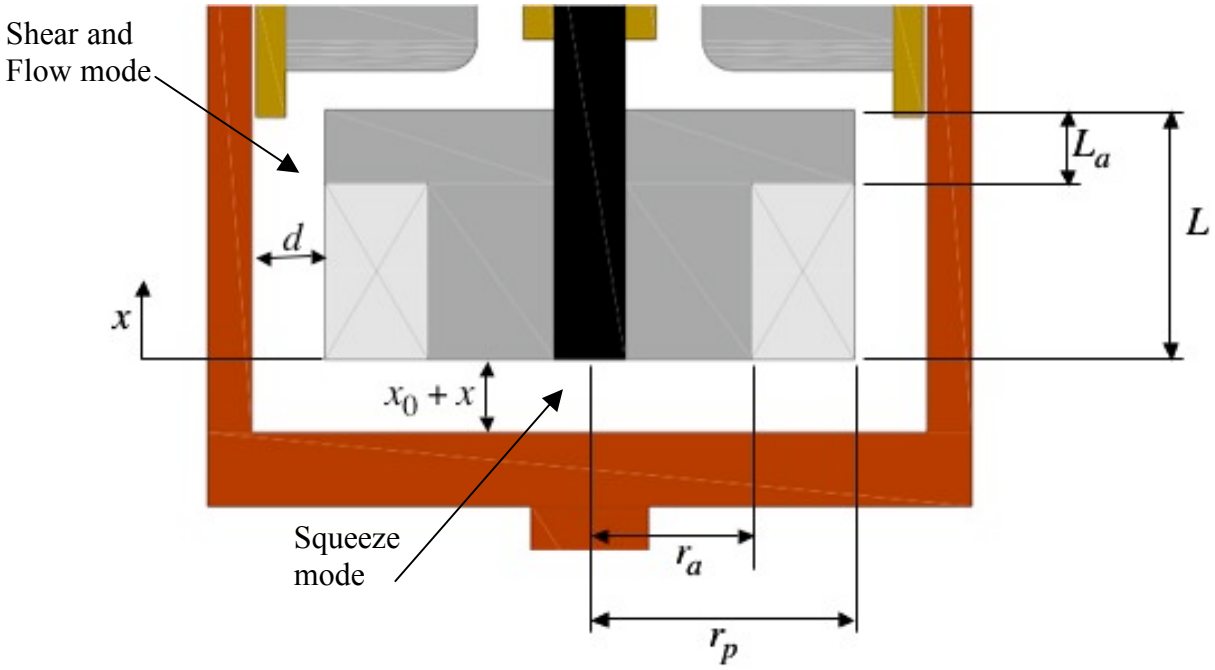

Figure 4.1 Geometric parameters used to model the MR isolator

The total force of the isolator will be a superposition of the damping force developed by each operating mode of the fluid as well as the stiffness and damping forces contributed by the elastomer. The elastomer is modeled as a spring-damper, its force is given by

$$F_{elastomer} = K_{el}x + C_{el}\dot{x} \tag{4.1}$$

4.1 Squeeze Mode

The force of the damper due to squeeze film behavior is modeled as a combination of viscous and MR effects [14]. Upon application of a magnetic field

there is an active region, where viscosity and MR effects are present as well as a passive region where only viscosity effects are present.

Compression of the fluid, which has a nominal thickness of x_0, initiates radial flow. The pressure of the fluid is the sum of the pressure contributions due to viscosity, P_μ, and magnetic field effects, P_{MR} [14].

$$P(r) = P_\mu + P_{MR} \tag{4.2}$$

The resulting force due to the fluid film is found by integrating the pressure over the respective passive and active bobbin areas.

$$F_{squeeze} = 2\pi \int P(r) r dr = 2\pi \int_0^{r_p} P_\mu(r) r dr + 2\pi \int_0^{r_a} P_{MR}(r) r dr \tag{4.3}$$

where, r_p is the radius of the passive area and r_a is the radius of the active area.

4.1.1 Viscous Pressure

To model the viscous pressure of the squeeze mode damper the radial flow is approximated by laminar flow in a wide rectangular channel with a width, $b(r)$, and height, $h(x)$. In this case, $b(r)$ is the circumference of the circle enclosing the fluid flow in the radial direction, at a radius r from the center of the bobbin and $h(x)$ is the gap height. These are given as [14]

$$\begin{aligned} b(r) &= 2\pi r \\ h(x) &= x_0 + x \end{aligned} \tag{4.4}$$

The volume flow rate through the channel, assuming $b(r) >> h(x)$, is given by [13]

$$Q(r) = \frac{b(r)h(x)^3}{12\mu}\frac{\partial P}{\partial r} \tag{4.5}$$

The flow rate through a given radius is equal to the flow rate due to the bobbin motion [14]

$$Q(r) = \pi r^2 \dot{x} \tag{4.6}$$

Substituting (4.4) and (4.6) into (4.5) and rearranging gives the viscous pressure differential as

$$\frac{\partial P}{\partial r} = \frac{6\mu r\dot{x}}{(x_o + x)^3} \tag{4.7}$$

Integration with respect to r yields

$$\int_0^r \frac{\partial P}{\partial r}dr = \int_0^r \frac{6\mu r\dot{x}}{(x_o + x)^3}dr$$

$$P_\mu(r) = \frac{3\mu r^2}{(x_0 + x)^3}\dot{x} \tag{4.8}$$

4.1.2 Pressure Due to MR Effect

The pressure gradient due to the yield force of the MR fluid is expressed using the Bingham plastic model. As this model assumes the fluid is in the post-yield phase, the pressure gradient due to the MR effect is equal to the pressure gradient required to initiate flow. This critical value is expressed in terms of the induced yield stress, $\tau_{y,sq}$, and the gap thickness, $x_0 + x$. It is given by [7]

$$\frac{\partial P_{MR}}{\partial r} = \frac{2\tau_{y,sq}}{(x_0 + x)}\operatorname{sgn}(\dot{x}) \tag{4.9}$$

Integration of (2.8) with respect to r yields

$$P_{MR} = \frac{2\tau_{y,sq} r}{(x_0 + x)}\operatorname{sgn}(\dot{x}) \tag{4.10}$$

Substitution of equations (4.8) and (4.10) into (4.3) and integrating yields the total squeeze mode force [14]

$$F_{squeeze} = 2\pi\int_0^{r_p} \frac{3\mu r^2}{(x_0 + x)^3}\dot{x} r dr + 2\pi\int_0^{r_a} \frac{2\tau_{y,sq} r}{(x_0 + x)}\operatorname{sgn}(\dot{x}) r dr$$

$$F_{squeeze} = \frac{3\pi\mu r_p^4}{2(x_0 + x)^3}\dot{x} + \frac{4\pi\tau_{y,sq} r_a^3}{3(x_0 + x)}\operatorname{sgn}(\dot{x})$$

$$F_{squeeze} = C_{sq}(x)\dot{x} + F_{y,sq}(x)\operatorname{sgn}(\dot{x}) \tag{4.11}$$

where

$$C_{sq} = \frac{3\pi\mu r_p^4}{2(x_0 + x)^3} \tag{4.11a}$$

$$F_{y,sq} = \frac{4\pi\tau_{y,sq} r_a^3}{3(x_0 + x)} \tag{4.11b}$$

The squeeze mode force is comprised of a displacement dependent viscous damping term as well as a displacement dependent yield force term. As both vary with changes in gap thickness there is a coupling between the force developed in the squeeze mode and the stiffness of the MR isolator.

4.2 Flow Mode

The damper consists of a cylindrical bobbin fitted inside a tubular outer cup. The space between the bobbin and outer cup forms an annulus through which the MR fluid flows. In the flow mode, the damper develops rate dependent damping forces due to the pressure drop through the annulus as velocity is applied to the damper bobbin. The MR fluid is activated by the magnetic field created by the bobbin. As in the case of the squeeze mode model, there are regions of passive and active damping along the length of the bobbin.

The pressure drop through the annulus (and resultant damping force) is due to a viscous term from Newtonian flow of the fluid, as well as an additional pressure drop due to the MR effect. Each of these two cases is considered separately.

4.2.1 Newtonian flow

First the balance of forces on a fluid element is considered. The flow is assumed laminar and fluid inertial terms are neglected. Using the parallel plate approximation the governing equation is given as [16]

$$\frac{\partial \tau}{\partial y} = -\frac{\partial p}{\partial z} \tag{4.12}$$

The pressure gradient is assumed to vary linearly along the length of the bobbin. Thus equation (4.11) can be rewritten as [16]

$$\frac{\partial \tau}{\partial y} = -\frac{\Delta P}{L} \tag{4.13}$$

In the case of Newtonian flow, the shear mechanism is [7]

$$\tau = \mu \frac{du}{dy} \tag{4.14}$$

Differentiating (4.14) with respect to y and plugging into (4.13) yields the governing equation for the flow field within the annulus [16]

$$\mu \frac{d^2u}{dy^2} = -\frac{\Delta P}{L} \tag{4.15}$$

Direct integration of equation (4.14) yields the velocity profile in the annulus. This is found to be [16]

$$u(y) = -\frac{\Delta P}{2\mu L} y^2 + C_1 y + C_2 \tag{4.16}$$

Where, C_1, C_2 are constants of integration to be solved by appropriate boundary conditions. The velocity boundary conditions for Newtonian shear flow at the outer cylinder, $y = 0$, and the bobbin, $y = d$, are

$$\begin{aligned} u(0) &= 0 \\ u(d) &= 0 \end{aligned} \tag{4.17}$$

Applying the boundary conditions (4.17) to equation (4.16) leads to the following velocity profile [16]

$$u(y) = \frac{-\Delta P}{2\mu L}(y^2 - dy) \tag{4.18}$$

Using the equation for the velocity profile in the annulus, it is possible to solve for the force due to the viscous effect. To do this, the volume flux through the annulus, Q, is equated to the volume flux displaced by the bobbin, Q_B. It is also noted that the

pressure difference across the annulus can be expressed as $\Delta P = F/A_P$ [6]. The volume fluxes are [16]

$$Q = b\int_0^d u(y)dy = \frac{bFd^3}{12A_P\mu L} \qquad (4.19)$$
$$Q_B = A_P\dot{x}$$

Equating the volume Fluxes leads to the following [16]

$$F_\mu = \frac{12A_P\mu L}{bd^3}\dot{x} \qquad (4.20)$$

4.2.2 MR Effect

As in section 3.1.2, the Bingham plastic model is used to find the pressure gradient required to initiate flow. From this the damping force due to the MR effect is found and summed with the viscous force to yield an expression for the total force due to fluid flow through the annulus.

The pressure differential is as follows [7]

$$\frac{\partial p}{\partial z} = \frac{\Delta P}{L_a} = \frac{2\tau_{y,fl}}{d}\mathrm{sgn}(\dot{x}) \qquad (4.21)$$

Where L_a is the magnetically active length within the annulus. This leads to the following expression for the force due to the MR effect. Again noting that, $\Delta P = F/A_P$.

$$F_{MR} = \frac{2A_P L_a \tau_{y,fl}}{d}\mathrm{sgn}(\dot{x}) \qquad (4.22)$$

Summing equations (4.22) and (4.20) gives the total force due to fluid flow through the annulus as [16]

$$F_{flow} = \frac{12A_P^2\mu L}{bd^3}\dot{x} + \frac{2A_P L_a \tau_{y,fl}}{d}\operatorname{sgn}(\dot{x})$$

$$F_{flow} = C_{flow}\dot{x} + F_{y,flow}\operatorname{sgn}(\dot{x}) \tag{4.23}$$

where,

$$C_{flow} = \frac{12A_P^2\mu L}{bd^3} \tag{4.23a}$$

$$F_{y,flow} = \frac{2A_P L_a \tau_{y,fl}}{d} \tag{4.23b}$$

The force developed in the flow mode is comprised of a viscous damping term and a yield force term. The viscous damping term is dependent on the geometry of the isolator and the velocity of the bobbin. The Yield force term is dependent on the geometry of the isolator, the sign of the velocity as well as the yield stress of the MR fluid, which varies with the strength of the magnetic field in the MR isolator.

4.3 Shear Mode

Here the approximate parallel plate analysis of the shear mode damper is presented. In this mode of operation, fluid flow and consequently damping force is a result of the direct shearing of the fluid as the bobbin moves relative to the wall of the outer cylinder. A balance of forces on a fluid element yields the following governing equation [7]

$$\frac{\partial \tau}{\partial y} = 0 \tag{4.24}$$

The Bingham model yields the following equation for the shear stress in the fluid [7]

$$\tau = \mu \frac{du}{dy} + \tau_{y,sh} \operatorname{sgn}\left(\frac{du}{dy}\right) \tag{4.25}$$

Differentiation of (4.25) with respect to y and plugging the result into (4.24) yields the following governing equation.

$$\mu \frac{d^2 u}{dy^2} = 0 \tag{4.26}$$

Direct integration and applying the boundary conditions, $u(0) = 0$, and $u(d) = \dot{x}$, leads to the velocity profile in the annular gap

$$u(y) = \frac{\dot{x}}{d} y \tag{4.27}$$

Plugging (4.27) into (4.25) results in an expression for the shear stress profile in the annular gap

$$\tau = \mu \frac{\dot{x}}{d} + \tau_{y,sh} \operatorname{sgn}(\dot{x}) \tag{4.28}$$

As would be expected the shear stress is independent of y and thus constant throughout the fluid. The force due to the shear flow is found by multiplying the shear stress by the effective bobbin area. The applied magnetic field is present over part of the bobbin length. This length is given as L_a. The total force due to the shear flow is given as [20]

$$F_{shear} = \frac{\mu b L}{d} \dot{x} + b L_a \tau_{y,sh} \operatorname{sgn}(\dot{x})$$

$$F_{shear} = C_{shear} \dot{x} + F_{y,shear} \operatorname{sgn}(\dot{x}) \tag{4.29}$$

where

$$C_{shear} = \frac{\mu b L}{d} \tag{4.29a}$$

$$F_{y,shear} = bL_a \tau_{y,sh} \tag{4.29b}$$

The force due to the shear mode has viscous and yield force components both of which depend on the geometry of the MR isolator.

4.4 Total Isolator Force

The total force of the isolator is the summation of the forces due to the elastomer as well as the forces due to the different modes of MR fluid operation. As discussed before, shear and flow mode damping occurs along the side of the bobbin while squeeze mode damping occurs in the area below the bobbin. As these damping modes occur in separate areas of the MR device, the strength of the magnetic field could vary between these areas, causing the yield stress of the fluid for the shear and flow modes ($\tau_{y,sh}, \tau_{y,fl}$) to be different than that of the squeeze mode, $\tau_{y,sq}$. It is not known a priori how the strength of the magnetic field within the MR device varies. It was not possible to obtain an accurate measurement of the strength of the magnetic field because any measurement would have required modifications to the MR device. Using a finite element model to obtain the strength of the magnetic field was also ruled out because a B-H curve for the MR fluid, which is required for a finite element magnetic analysis, was not available. For these reasons it was assumed that the magnetic field was equal in the two areas and that the yield stress of the fluid in the squeeze mode effect would be the same as the yield stress of the fluid in the shear and flow mode effect, $\tau_{y,sh} = \tau_{y,fl} = \tau_{y,sq} = \tau_y$. By summing equations 4.1, 4.11, 4.23, and 4.29, the total force of the MR isolator is given as

$$F_{damper} = F_{elastomer} + F_{flow} + F_{shear} + F_{squeeze}$$

$$F_{damper} = K_{el}x + C_{el}\dot{x} + C_{flow}\dot{x} + F_{y,flow}\,\mathrm{sgn}(\dot{x}) + C_{sq}(x)\dot{x} + F_{y,sq}\,\mathrm{sgn}(\dot{x}) + C_{shear}\dot{x} + F_{y,shear}\,\mathrm{sgn}(\dot{x})$$

$$F_{damper} = K_{el}x + \left(C_{el} + C_{flow} + C_{sq}(x) + C_{shear}\right)\dot{x} + \left(F_{y,flow} + F_{y,shear} + F_{y,sq}\right)\mathrm{sgn}(\dot{x})$$

$$F_{damper} = K_{el}x + \dot{x}\left(C_{el} + \frac{12A_pL\mu}{bd^3} + \frac{bL\mu}{d} + \frac{3\pi\mu r_p^4}{2(x_0+x)^3}\right) + \tau_y\,\mathrm{sgn}(\dot{x})\left(\frac{2A_pL_a}{d} + bL_a + \frac{4\pi r_a^3}{3(x_0+x)}\right)$$

$$F_{damper} = Kx + C\dot{x} + F_y\,\mathrm{sgn}(\dot{x}) \tag{4.30}$$

where,

$$K = K_{el} \tag{4.30a}$$

$$C = \left(C_{el} + \frac{12A_pL\mu}{bd^3} + \frac{bL\mu}{d} + \frac{3\pi\mu r_p^4}{2(x_0+x)^3}\right) \tag{4.30b}$$

$$F_y = \tau_y\left(\frac{2A_pL_a}{d} + bL_a + \frac{4\pi r_a^3}{3(x_0+x)}\right) \tag{4.30c}$$

The total force of the isolator is equivalent to a parallel combination of a spring, a viscous damper and a coulomb element. The spring element simulates the elastic behavior of the MR isolator, the damper captures the viscous effects of the MR damper and the coulomb element accounts for the yield force of the MR fluid.

4.5 Identification of Model Parameters

Implementation of the isolator model requires knowledge of the isolator geometry, the fluid properties, μ and τ_y, the damping of the elastomer, C_{el}, and

the stiffness of the isolator, and K. Variation of these variables allows the damping levels produced by the MR device to be changed over time. The damper geometry is known. However, accurate knowledge of the material properties: fluid viscosity, μ; yield stress of the fluid, τ_y; storage stiffness, K; and elastomer damping coefficient, C_{el}, are harder to obtain.

Ideally μ is constant in the fluid. It's value found through experimental measurements, or as quoted by a manufacturer. τ_y is an abstract fluid property that varies with applied magnetic field. The magnetic field of the MR isolator is controlled through an applied current, so it is often convenient to express the yield stress as a function of the applied current. One drawback being this makes $\tau_y(i)$ specific to the particular geometry of the isolator. Several methods to find $\tau_y(i)$ are often employed. Using a rheometer it is possible to find the yield stress of the fluid for a given magnetic field strength, $\tau_y(H)$. In order to apply this information to a particular isolator geometry the variation of magnetic field strength in the MR isolator with applied current must be found. Another approach is to measure the force of the MR isolator for a given applied current. Using the measurements of force it is possible to calculate the yields stress of the MR fluid. One drawback to this method is $\tau_y(i)$ is specific to the particular geometry of the isolator as well as to the analytical model used for the isolator.

4.5.1 Passive Damping Identification

From the force-displacement plot shown in Chapter 3, figure 3.2, it can be seen that in the absence of applied current the plots are elliptical in shape and upon

application of current the plots deviate from this elliptical nature, they become rectangular in shape. In the case when no current is applied to the isolator the damping force is due only to the elastomeric damping coefficient, C_{el}, and the fluid viscosity coefficient, μ. Upon application of current the yield force of the fluid accounts for the increase in the damping force of the MR isolator. The elastomeric damping coefficient, C_{el}, and the fluid viscosity, μ, are chosen to match the behavior of the MR isolator in the absence of applied current.

The plots of the equivalent damping coefficient versus displacement as well as the equivalent damping coefficient versus frequency, figures 3.4-3.8, show that in the case when current is not applied to the isolator the amount of damping does not vary greatly over the testing range, thus C_{el} and μ are chosen as constants.

A value for fluid viscosity specific to the MR fluid used in this project was not readily available, as the required experimental testing had not yet been completed. Instead the fluid viscosity of a similar MR fluid, MRF-336AG, was used. This fluid, a product of Lord Corporation, is also a silicone oil based fluid and is 82% solid by weight. The viscosity of MRF-336AG as quoted by Lord Corp. is 0.09 Pa-s.

Using results from the damper characterization, the elastomeric damping coefficient was chosen. The damping coefficient was chosen as the average value of the equivalent viscous damping coefficient over the testing range for 0 A applied current. Using this method C_{el} was found to be 300 N-s/m.

4.5.2 Storage Stiffness and Yield Stress Identification

The force versus displacement plot from Chapter 3, figure 3.2, gives insight to the nature of the properties τ_y and K. It is apparent that upon application of current the area enclosed by each plot increases, signifying an increase in damping. This increase is accounted for by the additional force produced due to the yield stress of the MR fluid, which increases with increasing current. A more careful observation of the force-displacement plots shows that upon an increase in current the plot will also undergo a slight rotation counter clockwise. This is evident of an increase in stiffness. This varying stiffness is accounted for by assuming the storage stiffness, K, changes as a function of applied current and therefore applied magnetic field. It is also assumed that these variables will be dependent upon oscillation frequency as well as displacement amplitude, that is $K = K(\omega, A, H)$ and $\tau_y = \tau_y(\omega, A, H)$. The ability of the model to represent the experimental data depends greatly on the proper identification of these two parameters.

4.5.2.1 Complex Modulus Identification

The first technique used to identify these parameters incorporated the storage stiffness found in the complex modulus approach of damper characterization as well as an optimization technique to find the yield stress. The stiffness of the elastomer at a given frequency, ω, a given displacement amplitude, X, and a given magnetic field strength, H, was assumed to be equal to the calculated storage stiffness

$K(\omega,X,H) = K'(\omega,X,H)$. Then, using an optimization technique the yield stress of the fluid, $\tau_y(\omega,X,H)$ was calculated to minimize the objective function

$$f = \sum_{t=0}^{t=t_{final}} \left(F_{experimental}(\omega,X,H,t) - F_{damper}(\omega,X,H,t)\right)^2 \qquad (4.31)$$

Using this technique, the stiffness of the isolator model, K, is represented as having the same stiffness as a spring element used in a Kelvin chain model, which consists of a spring and viscous damper in parallel. Using the Kelvin chain model the yield force of the fluid is simulated by the spring and damper, thus the stiffness will include MR effects and may not be suitable for implementation into the isolator model. The predicted isolator force using this technique is shown in figure 4.2.

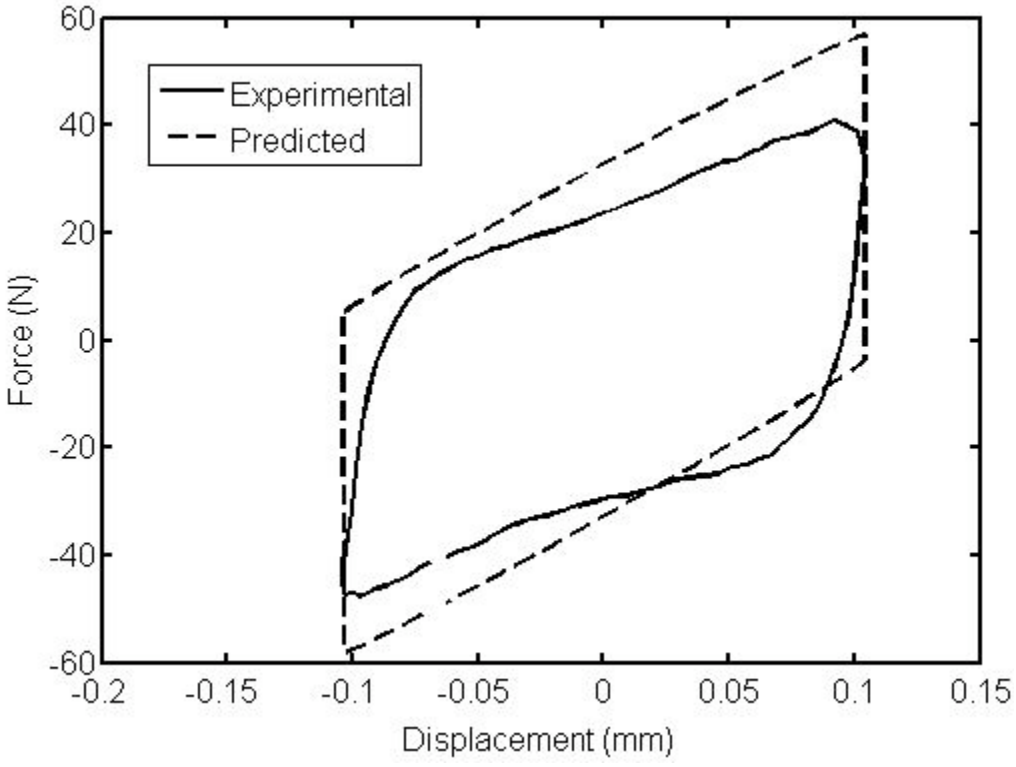

Figure 4.2 Predicted force using storage stiffness from the isolator characterization and experimental force versus displacement for excitation frequency of 5 Hz

4.5.2.2 Displacement Averaged Stiffness and Velocity Averaged Damping

Another way to identify the parameters K and τ_y is through a separation of the experimental force output data into a linearized stiffness force and a linearized damping force, then using these components of force extracting information about the isolator's stiffness and damping behavior. In order to demonstrate this technique consider the simple model of an MR isolator

$$F = F_k + F_d + F_y = K_1 x + C_1 \dot{x} + F_{\tau_y,1} \operatorname{sgn}(\dot{x}) \qquad (4.32)$$

Under sinusoidal excitation, $x = \sin(wt)$, the force-displacement and force-velocity plots are shown in figures 4.3 and 4.4. It can be seen in figure 4.3 that for the force-displacement plot the stiffness force, F_k, varies linearly with displacement. On the other hand the total damping force, $F_d + F_y$, which is dependent on velocity, is of an elliptical nature and is symmetric about the force axis = 0. The average of the damping force over a cycle for a given value of displacement will equal zero. Thus by averaging the total force (which is a summation of the stiffness and total damping forces) for a given value of displacement over a single cycle (signified by the points on figure 4.3), the total damping force will be canceled leaving only the stiffness force.

In the force-velocity plot, figure 4.4, exactly the opposite is true. By averaging the total force for a given value of velocity over a single cycle the stiffness force will be canceled leaving only the total damping force.

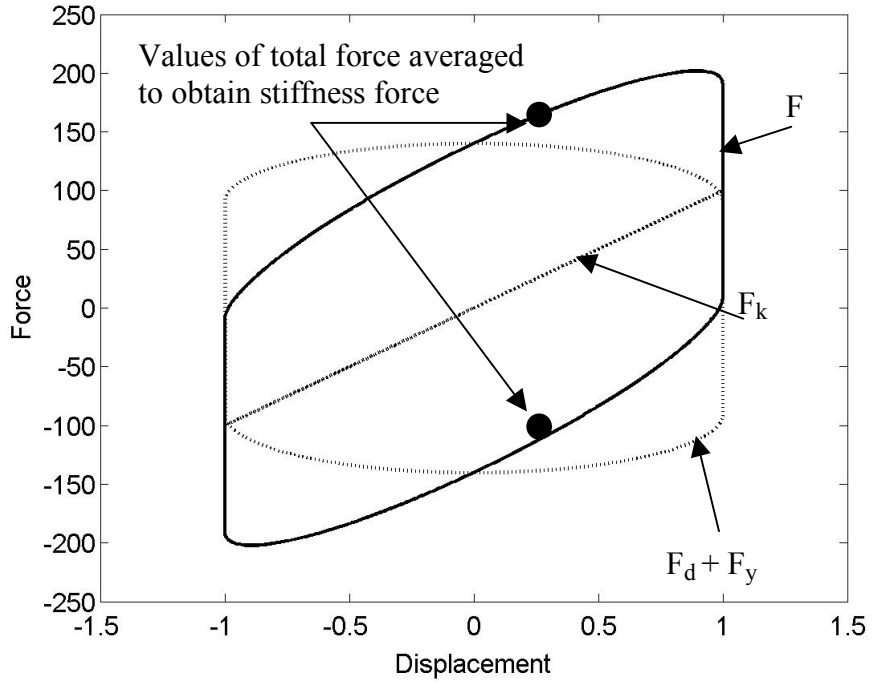

Figure 4.3 Total force, stiffness force and total damping force versus displacement for a simple MR isolator example

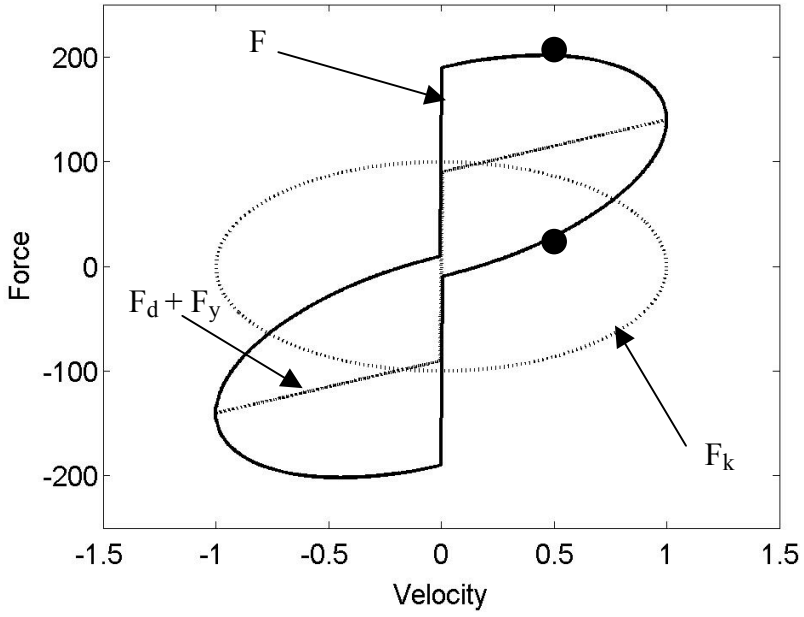

Figure 4.4 Total force, stiffness force and total damping force versus velocity for a simple MR isolator example

The slope of the displacement averaged stiffness force in the force-displacement plane yields the stiffness of the isolator as

$$F_k = K_1 x \tag{4.33}$$

The value of the total damping force for any known velocity, $\dot{x}$, can be used to extract the yield force of the MR isolator as

$$F_d + F_y = C_1 \dot{x} + F_{\tau_y,1} \operatorname{sgn}(\dot{x}) \tag{4.34}$$

or upon rearranging

$$F_{\tau_y,1} = \frac{F_d + F_y - C_1 \dot{x}}{\operatorname{sgn}(\dot{x})} \tag{4.35}$$

In order to extend this process to the experimental force output data an approach taken by Hu and Wereley [18] is followed. From the reconstructed displacement signal the displacement phase angle, $\phi(t)$, at an arbitrary time t can be known. Re-writing the reconstructed displacement signal given in equation (3.3) as

$$x(t) = \sqrt{X_c^2 + X_s^2} \sin\left[\phi(t)\right] \tag{4.36}$$

where,

$$\phi(t) = \omega t + \arctan\left(\frac{X_c}{X_s}\right) \tag{4.37}$$

Starting from the start time t_0, when $\phi(t_0) = \frac{\pi}{2}$, the stiffness force has the same phase angle as the displacement $\phi(t)$ and the damping force is $\frac{\pi}{2}$ ahead of the phase angle $\phi(t)$. The stiffness force, F_s, can be obtained as

$$F_s\left[\phi(t)\right] = \frac{1}{2}\left(F\left[\phi(t)\right] + F\left[2\pi - \phi(t)\right]\right) \qquad (4.38)$$

and

$$\begin{aligned} &F_s\left[2\pi - \phi(t)\right] = F_s\left[\phi(t)\right] \\ &\phi(t) = \phi(t_0),\ldots,\phi(t_0) + \pi \end{aligned} \qquad (4.39)$$

Similarly, from a different start time t_0' when $\phi(t_0') = 0$, the damping force, F_d, is obtained as follows

$$F_d\left[\phi(t)\right] = \frac{1}{2}\left(F\left[\phi(t)\right] + F\left[2\pi - \phi(t)\right]\right) \qquad (4.40)$$

and

$$\begin{aligned} &F_d\left[2\pi - \phi(t)\right] = F_d\left[\phi(t)\right] \\ &\phi(t) = \phi(t_0'),\ldots,\phi(t_0') + \pi \end{aligned} \qquad (4.41)$$

In figures 4.5 and 4.6 the linearized stiffness and linearized damping forces resulting from the above technique are shown. The displacement excitation is 5Hz oscillation frequency and 0.5mm displacement amplitude with 2 amperes of current applied to the MR isolator.

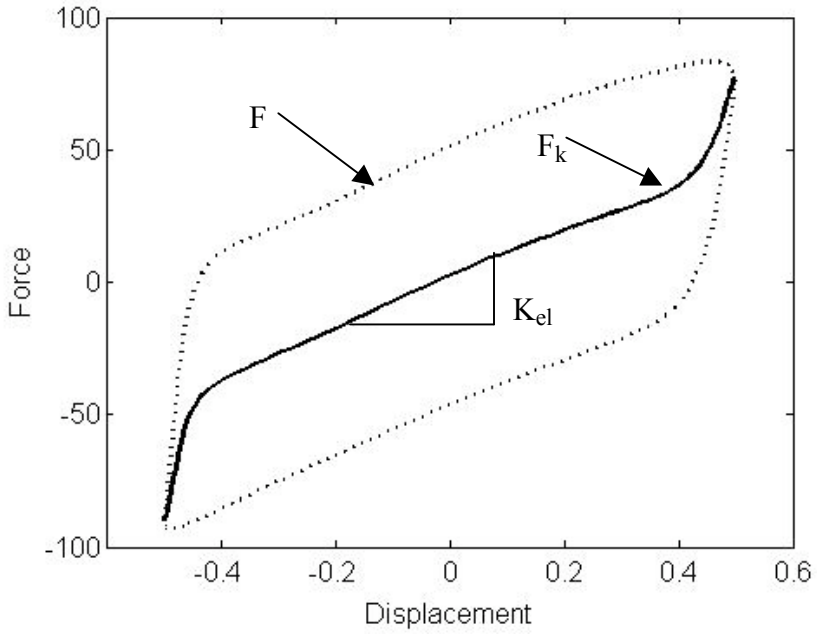

Figure 4.5 Displacement averaged stiffness force and experimental force versus displacement

In order to find the stiffness of the MR isolator the linearized stiffness force is used. The nonlinear effects of the stiffness force found near the maximum and minimum values of displacement, which are due to a transition of the yield stress in the fluid as velocity changes sign, are ignored. For a displacement amplitude of The truncated stiffness force is curve fit using a first order polynomial function. $F_s = C_0 + C_2 x$. Any bias is filtered so only the slope of the stiffness curve remains.

$$F_s = C_2 x \qquad (4.42)$$

Setting (4.42) equal to the displacement dependent portion of the model damper force (4.30) gives

$$F_s = C_2 x = K_{el} x \qquad (4.43)$$

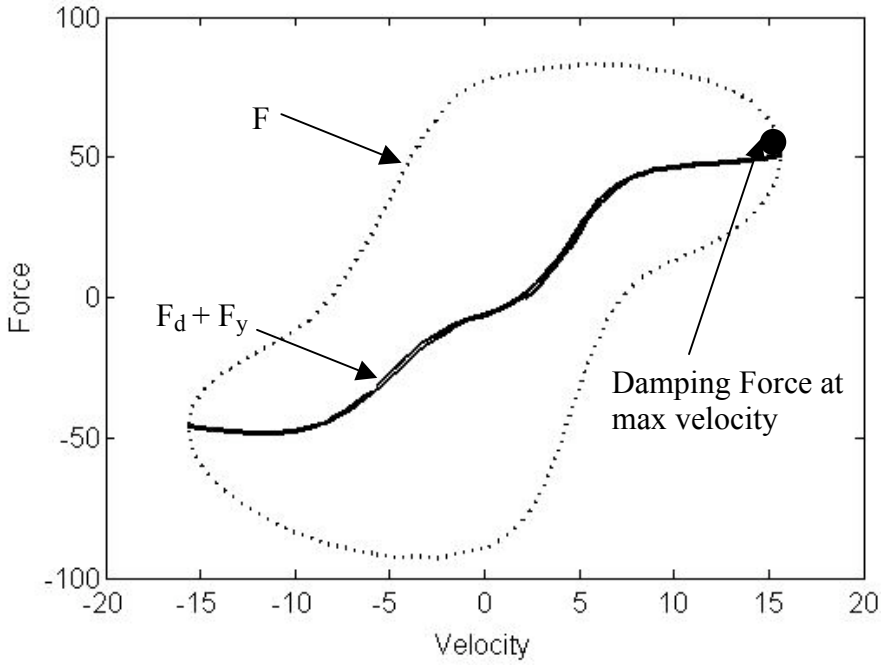

Figure 4.6 Velocity averaged damping force and experimental force versus velocity

To find the yield force of the MR fluid the value of linearized damping force at maximum velocity, $\dot{x}_{\max}$, as well as minimum velocity, $\dot{x}_{\min}$, are used. It is noted that maximum and minimum velocity occur when displacement, x, is zero. The elastomeric damping and viscous effects are subtracted from the damping force in order to obtain the component of the damping force resulting from the fluids yield force

$$\begin{aligned} F_{\tau_y}\left(\dot{x}_{\max}\right) &= \left(F_d + F_y\right)_{\dot{x}_{\max}} - C\big|_{x=0}\,\dot{x}_{\max} \\ F_{\tau_y}\left(\dot{x}_{\min}\right) &= \left(F_d + F_y\right)_{\dot{x}_{\min}} - C\big|_{x=0}\,\dot{x}_{\min} \end{aligned} \tag{4.44}$$

Setting the average yield force, $F_{\tau_y} = \dfrac{\left|F_{\tau_y}\left(\dot{x}_{\max}\right)\right| + \left|F_{\tau_y}\left(\dot{x}_{\min}\right)\right|}{2}$, equal to the predicted yield force given by (4.30) and rearranging gives

$$\tau_y = \frac{F_{\tau_y}}{\left(\frac{2A_pL_a}{d} + bL_a + \frac{4\pi r_a^3}{3(x_0)}\right)} \tag{4.45}$$

The reconstructed force-displacement cycle using this technique is shown in figure 4.7.

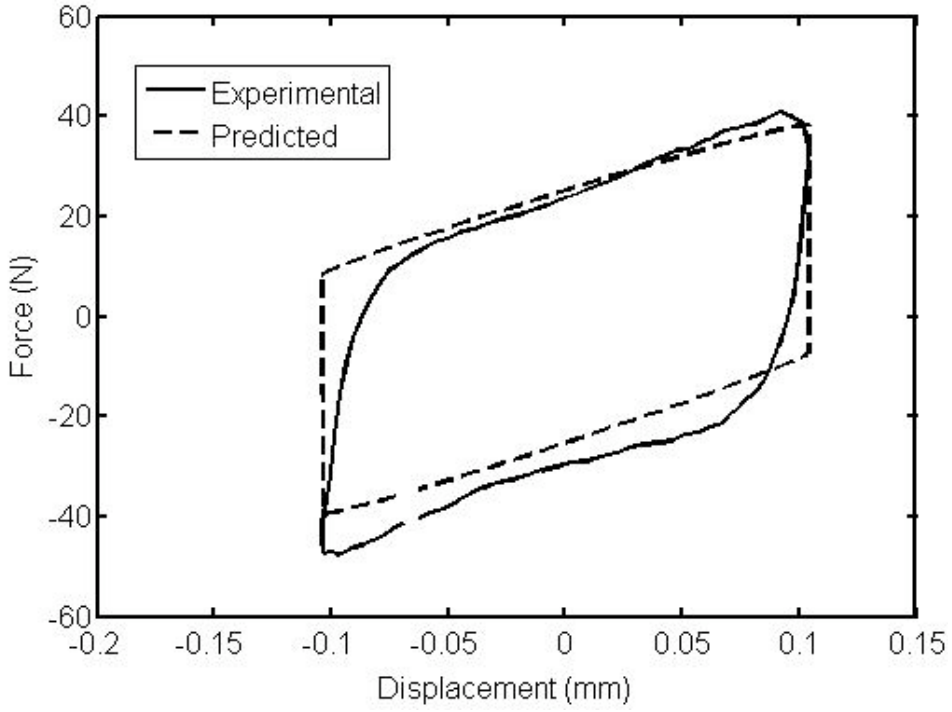

Figure 4.7 Predicted force using displacement averaged stiffness and velocity averaged damping techniques and experimental force versus displacement for excitation frequency of 5 Hz

4.5.3 Evaluation of Parameter Identification Methods

In order to compare the isolator models resulting from the different methods used for parameter identification an error metric was used. The complex correlation coefficient (CCF) is a numerical method, which compares the perimeters of 2D

objects to assess their similarity. In this case, the CCF was used to compare the force-displacement cycle generated by the isolator models with the force-displacement cycle from the experimental data. The CCF is valuable because it is a quantitative measure of the shape of the force-displacement cycle as well as a measure of the ability of the model to predict the force values. Therefore, both the magnitude and the phase of the model with respect to the experimental data are considered. The boundary functions of the force versus displacement cycle are given by

$$h(t) = x(t) + jf(t) \tag{4.46}$$

$$\hat{h}(t) = x(t) + j\hat{f}(t) \tag{4.47}$$

here h is the boundary function for the experimental data consisting of the reconstructed displacement and the measured force. Here $\hat{h}$ is the boundary function for each model, which consists of the reconstructed displacement and predicted damper force. The CCF is given by the expression

$$CCF = \frac{\int h(t)\hat{h}^*(t)dt}{\left[\left(\int h(t)h^*(t)dt\right)\left(\int \hat{h}(t)\hat{h}^*(t)dt\right)\right]^{1/2}} \tag{4.48}$$

where $h^*(t)$ and $\hat{h}^*(t)$ are the complex conjugates of $h(t)$ and $\hat{h}(t)$ respectively. If the hysteresis cycles being compared are identical, then the CCF will equal 1.

The CCF versus displacement amplitude for the different models is shown in figure 4.8. The oscillation frequency was kept constant at 10 Hz. The CCF results show that the parameter identification using the linearized stiffness and damping technique gives the best correlation with the experimental data for 3 out of the 4 displacements tested. The only case where the complex modulus approach yielded

better results was for the smallest amplitude tested (0.1mm). The model using the displacement averaged stiffness and velocity averaged damping technique is better able to predict the isolator force. A further comparison between the isolator forces predicted from the linearized stiffness model as well as that obtained experimentally is made in the following section.

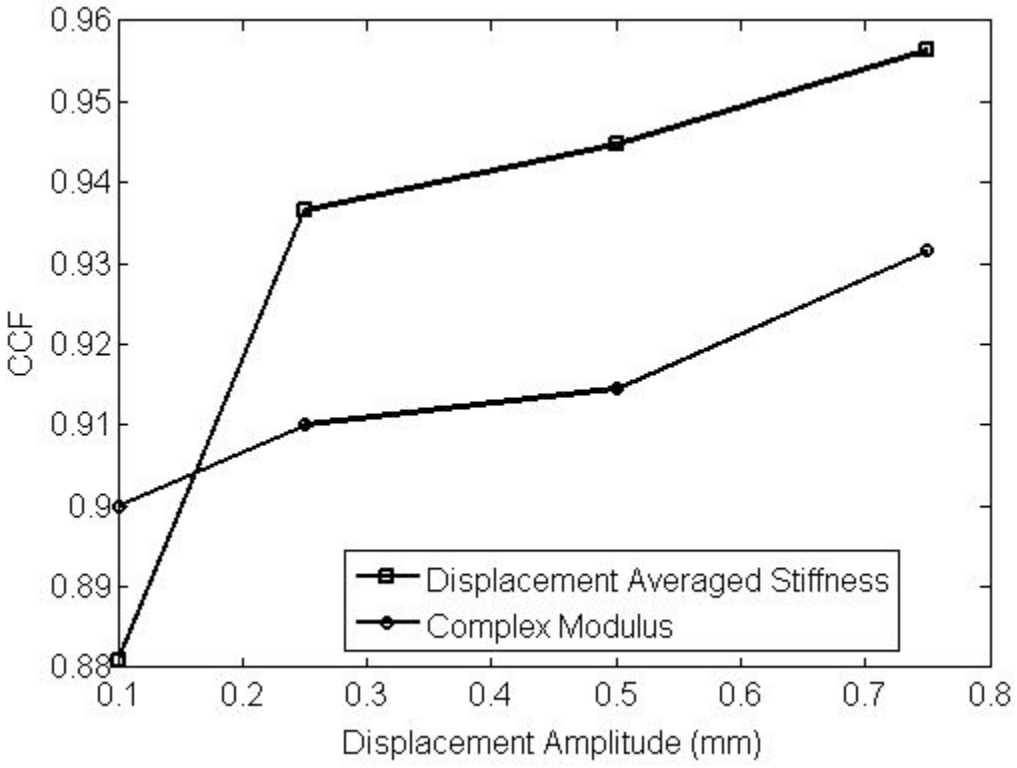

Figure 4.8 Complex Correlation Coefficient versus displacement amplitude for excitation frequency of 10 Hz and applied current of 2 A.

4.6 Model Results

The variation of the elastomeric stiffness, K_{el}, which was calculated using the displacement averaged stiffness technique, is shown in figures 4.10-4.13. The elastomeric stiffness is strongly dependent upon displacement amplitude as well as applied current. It is relatively constant with frequency. The variation of the yield

shear stress, τ_y, which was calculated using the velocity averaged damping technique, is shown in figures 4.14-4.17. Like the stiffness the yield shear stress is dependent upon displacement amplitude and applied current. The yield shear stress is also frequency dependent.

The performance of the Bingham model was first judged qualitatively by plotting the model predictions for a sinusoidal displacement input with the experimental test data. Figures 4.18-4.21 show the force-displacement plots at 5 Hz oscillation frequency for displacement amplitudes of 0.1mm, 0.25mm, 0.5mm and 0.75mm, respectively. Generally, the results look the model is able to approximate the experimental force-displacement plots. Figures 4.22-4.25 show force-velocity plots at 5 Hz oscillation frequency for displacement amplitudes of 0.1mm, 0.25mm, 0.5mm and 0.75mm, respectively. The solid lines stand for experimental data and the dashed line is the predicted data generated from the model. The Bingham-plastic model cannot predict the low-speed velocity characteristics of the MR isolator. Even though the Bingham model is unable to capture the hysteresis loop, it is still able to predict the magnitude of the damping force.

The ability of the model to predict damping performance is assessed through a comparison of the predicted equivalent damping coefficient and the predicted quadrature stiffness to those found experimentally. Figure 4.26 shows the equivalent damping coefficient versus displacement amplitude for an oscillation frequency of 5 Hz. Figures 4.27-4.30 show the equivalent damping coefficient versus frequency for displacement amplitudes of 0.1 mm, 0.25 mm, 0.5 mm, and 0.75 mm, respectively. Figure 4.31 shows the variation of quadrature stiffness with displacement amplitude

at 5 Hz frequency while figures 4.32-4.35 show the variation of quadrature stiffness with frequency for displacement amplitudes of 0.1 mm, 0.25 mm, 0.5 mm, and 0.75 mm, respectively. The predicted equivalent damping coefficient and quadrature stiffness correlate well with those found experimentally. The Bingham model is able to capture the damping behavior of the MR isolator for varying frequency and displacement amplitude.

The Bingham model was not able to accurately predict the storage stiffness of the MR isolator. This is reflected in figure 4.36, which shows the storage stiffness versus displacement amplitude at 5 Hz oscillation frequency, as well as in figures 4.37-4.40, which show the variation of storage stiffness with frequency for displacement amplitudes of 0.1 mm, 0.25 mm, 0.5 mm, and 0.75 mm, respectively. The model does not capture the behavior of the storage stiffness as the experimental stiffness tends to decrease with increasing frequency. This trend is not exhibited by the predicted storage stiffness.

In order to study the ability of the model to predict the MR isolators force quantitatively the complex correlation coefficient (CCF) was used, which compares the shape and phase of the model fit. A CCF of 1 indicates a perfect model fit. Figures 4.41-4.44 show the CCF versus frequency of excitation. As can be seen the lowest CCF is CCF=0.85 and occurs for a displacement amplitude of 0.1mm. As amplitude of displacement increases the correlation is found to increase as well. The best correlation between the model and experiment was found for low values of applied current and high values of displacement.

Using the model it is possible to obtain the relative contribution of force from each of the MR fluid operating modes as well as that from the elastomer. Figure 4.9 is a table showing the maximum force during a single sinusoidal displacement cycle for each contributor to the total isolator force over a range of displacement amplitudes. The oscillation frequency is constant at 5 Hz and the applied current is a constant 2 A. The main contributors to total force are the elastomer and the squeeze mode effect of the MR fluid. The flow mode and shear contribute only small amounts of force. These two modes do not significantly contribute to the total force because the amplification ratio, a measure comparing the cross-sectional area of the annular gap to the area of the bobbin, is relatively small. The width of the bobbin is 36mm and the gap width is 3.5mm. This leads to an amplification ration of approximately 2.5, which is well below ratios typically used in flow mode MR devices.

Maximum force during a cycle of sinusoidal displacement (N)				
	0.1mm	0.25mm	0.5mm	0.75mm
Elastomer	14.40	29.27	45.92	58.54
Squeeze Mode	17.24	29.67	43.23	55.18
Flow Mode	4.93	8.14	11.04	12.98
Shear Mode	1.36	2.24	3.01	3.53

Figure 4.9 Contributions of force for the MR fluid operating modes as well as the elastomer for varying displacement amplitude, excitation frequency of 5 Hz and applied current of 2 A.

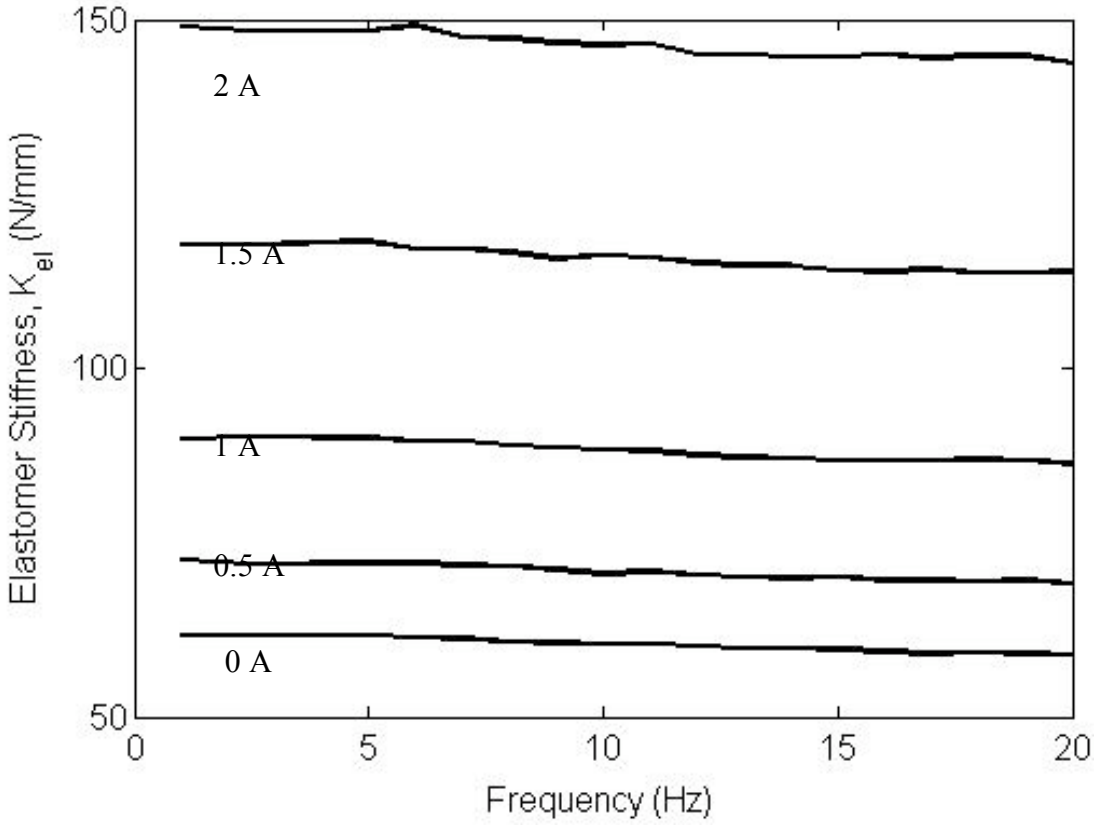

Figure 4.10 Stiffness coefficient using the displacement averaged stiffness technique versus frequency for displacement amplitude of 0.1 mm and varying applied current.

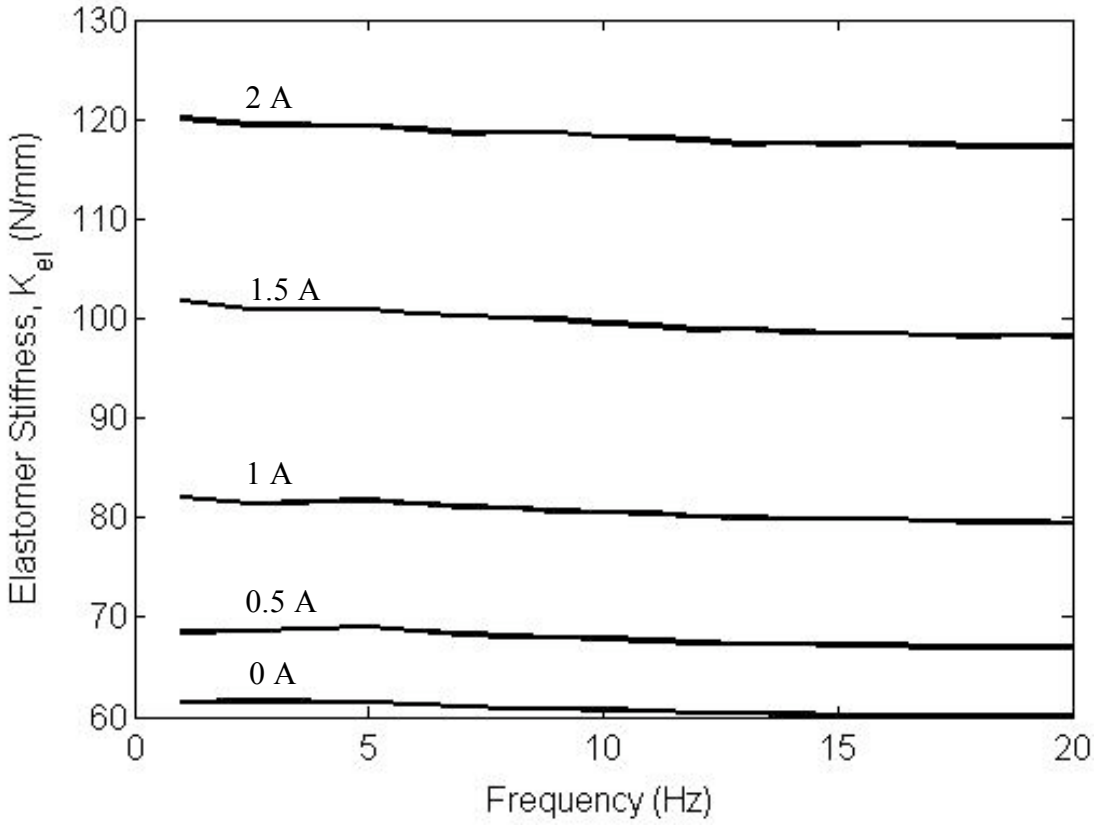

Figure 4.11 Stiffness coefficient using the displacement averaged stiffness technique versus frequency for displacement amplitude of 0.25 mm and varying applied current.

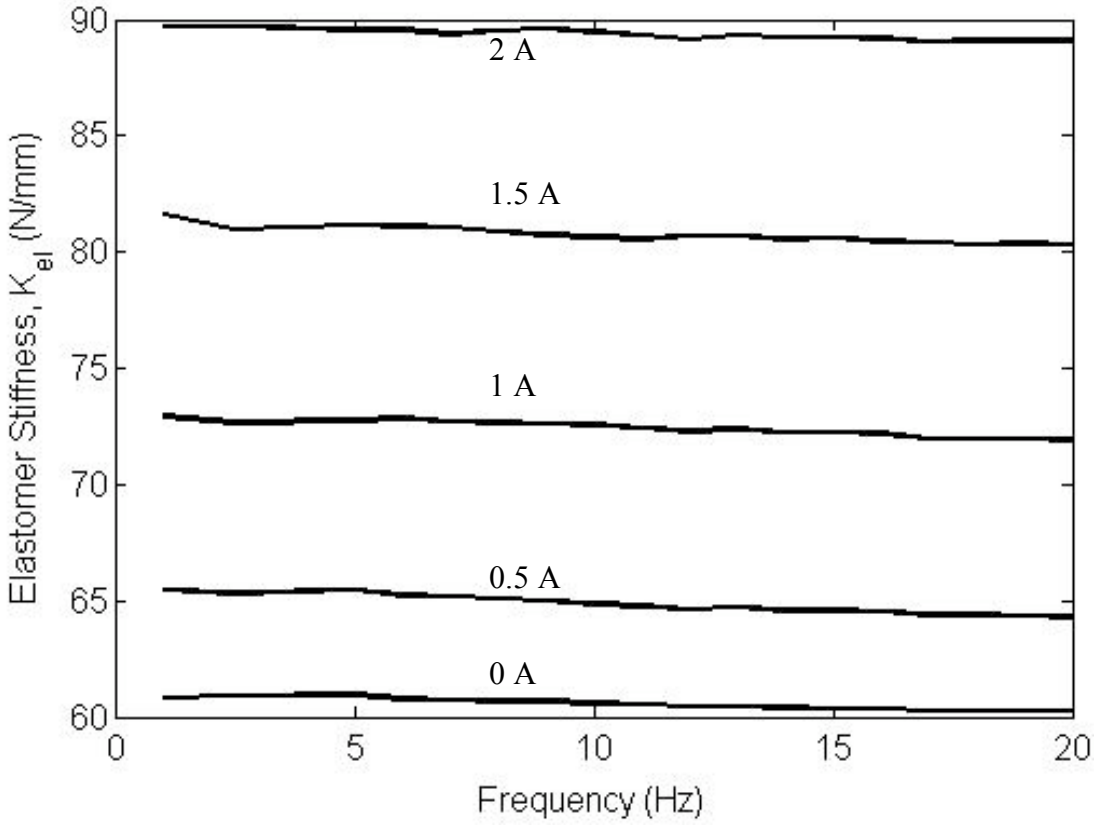

Figure 4.12 Stiffness coefficient using the displacement averaged stiffness technique versus frequency for displacement amplitude of 0.5 mm and varying applied current.

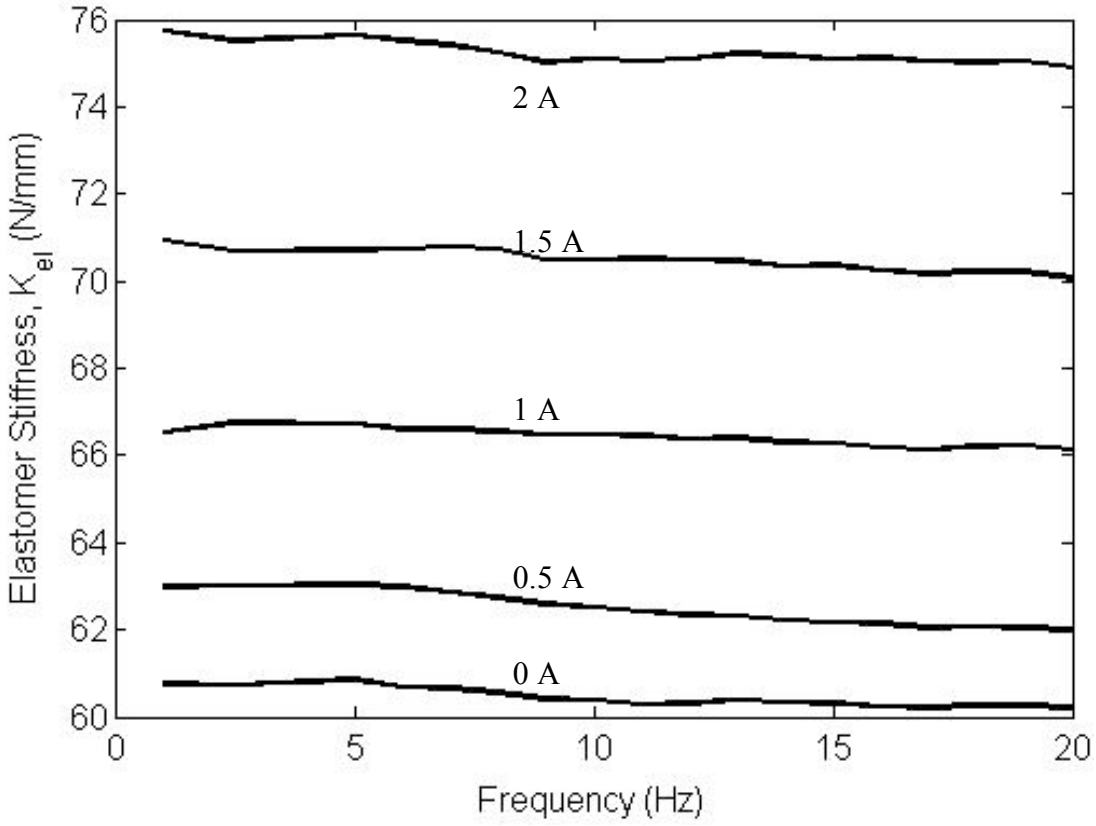

Figure 4.13 Stiffness coefficient using the displacement averaged stiffness technique versus frequency for displacement amplitude of 0.75 mm and varying applied current.

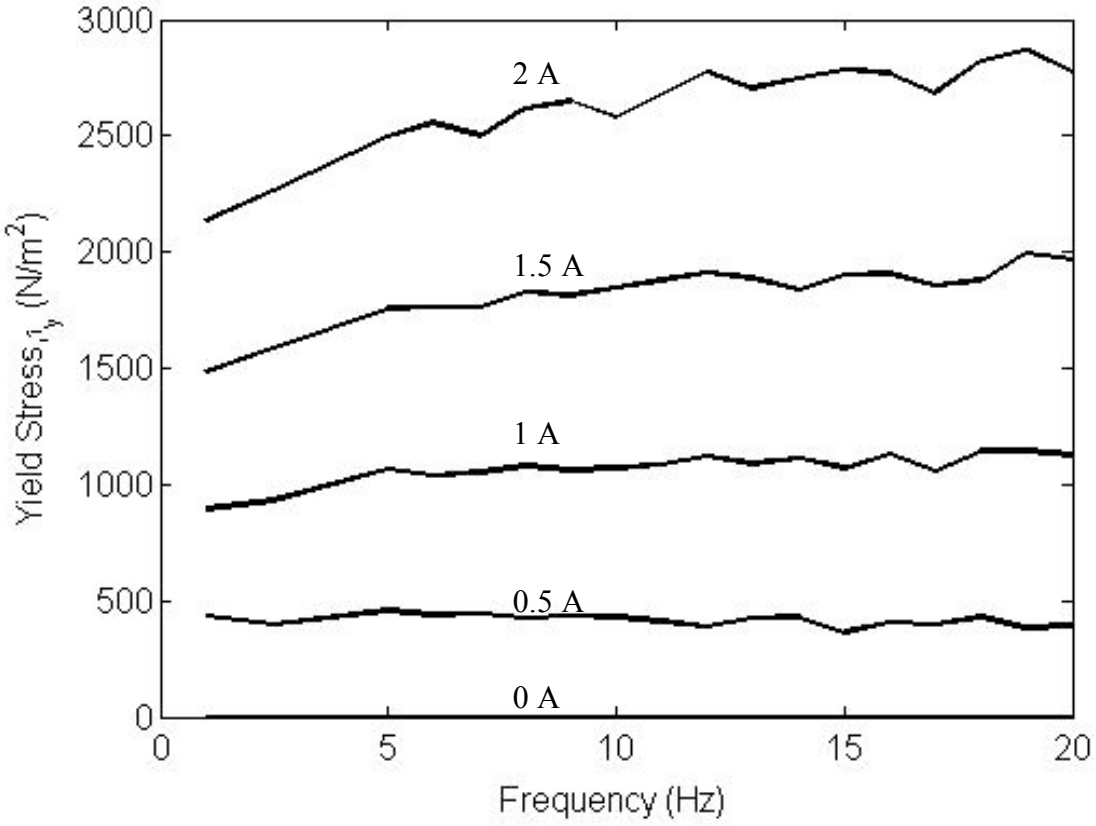

Figure 4.14 Yield shear stress using velocity averaged damping technique versus frequency for displacement amplitude of 0.1 mm and varying applied current.

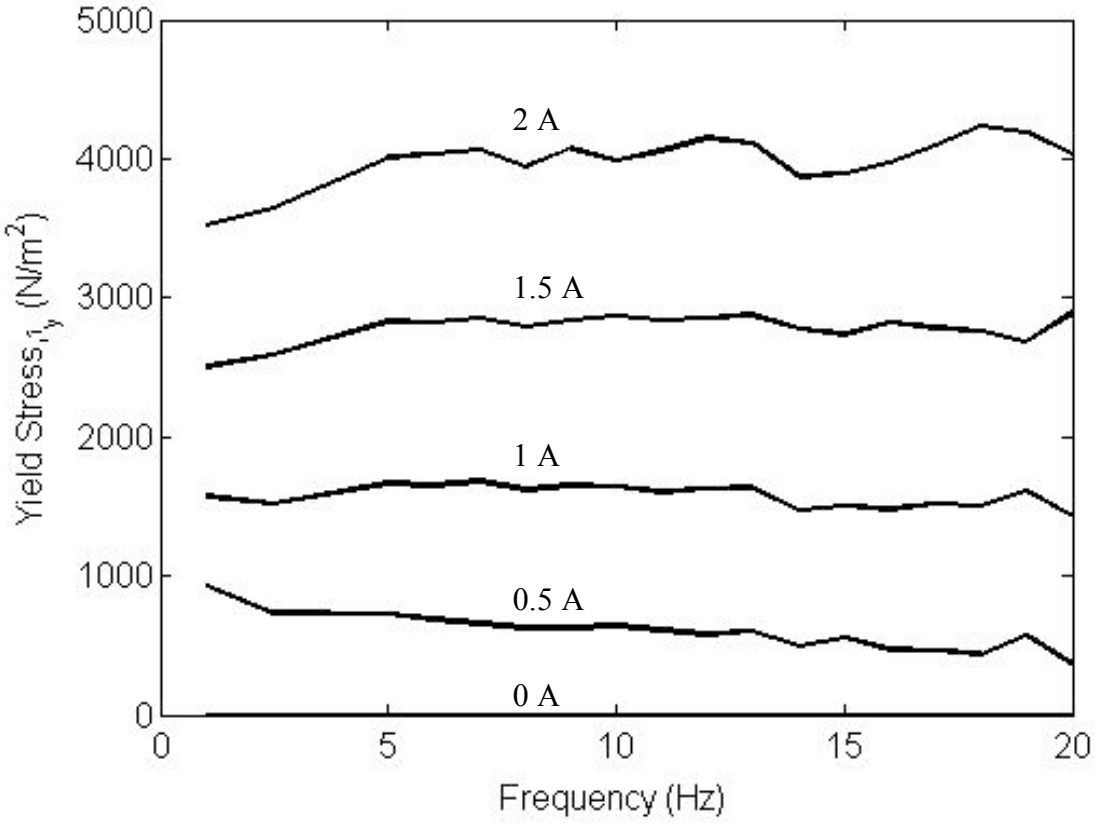

Figure 4.15 Yield shear stress using velocity averaged damping technique versus frequency for displacement amplitude of 0.25 mm and varying applied current.

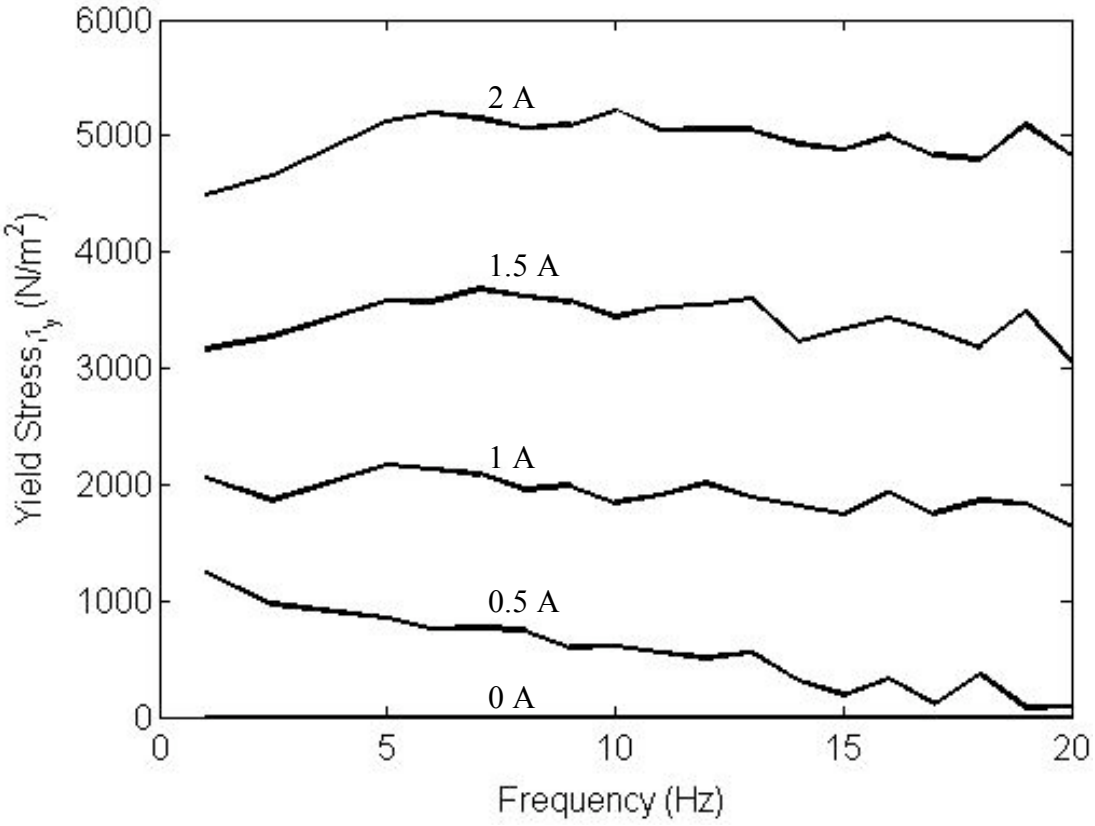

Figure 4.16 Yield shear stress using velocity averaged damping technique versus frequency for displacement amplitude of 0.5 mm and varying applied current.

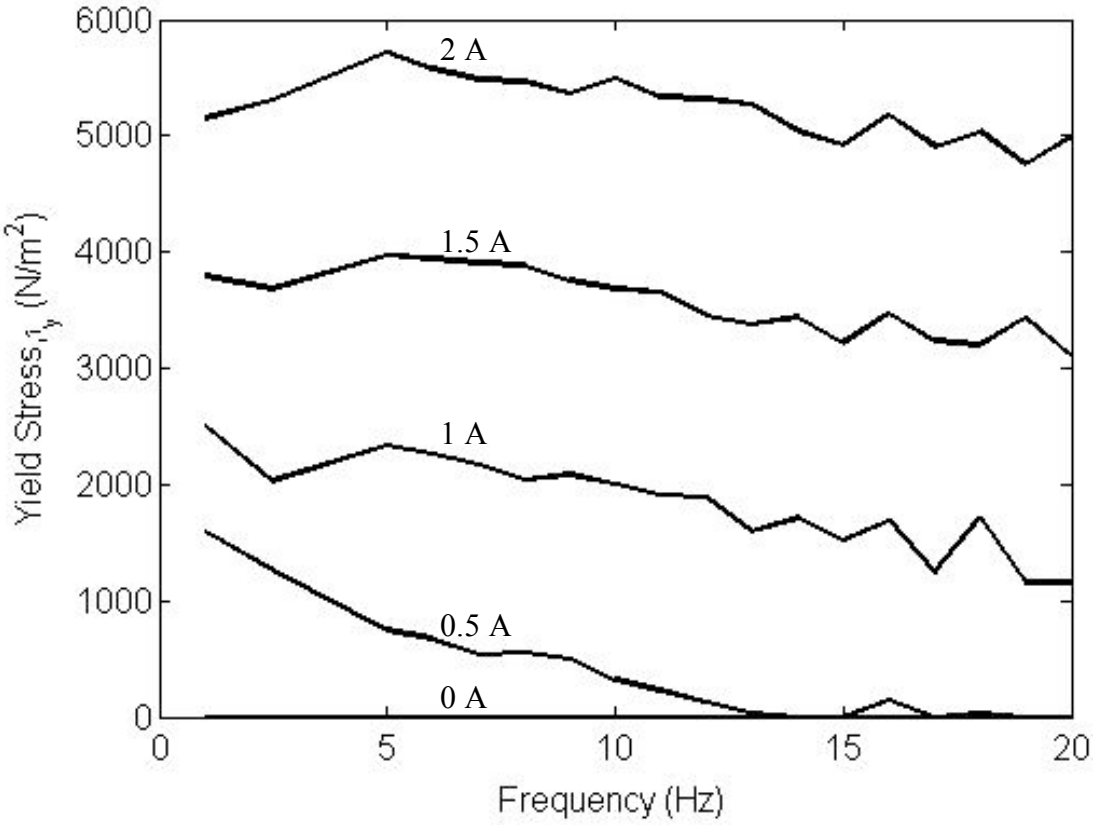

Figure 4.17 Yield shear stress using velocity averaged damping technique versus frequency for displacement amplitude of 0.75 mm and varying applied current.

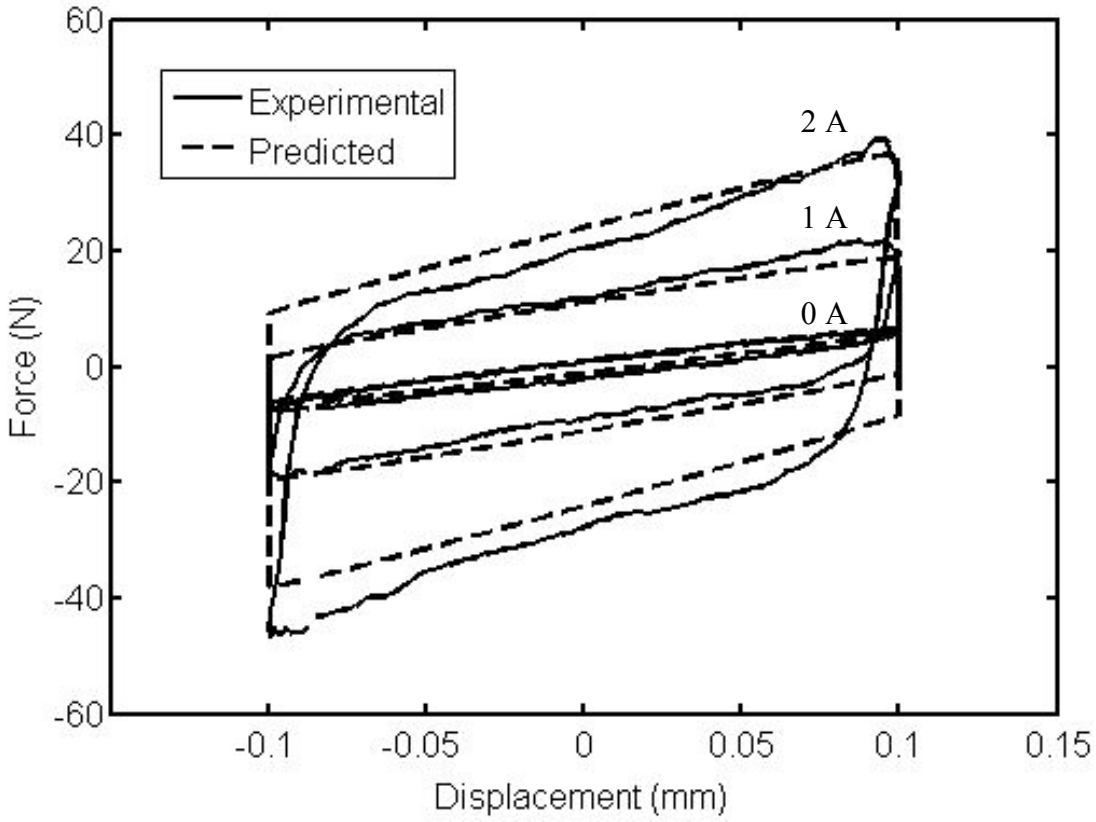

Figure 4.18 Predicted force using Bingham model and experimental force versus displacement for displacement amplitude of 0.1 mm, excitation frequency of 5 Hz and varying applied current.

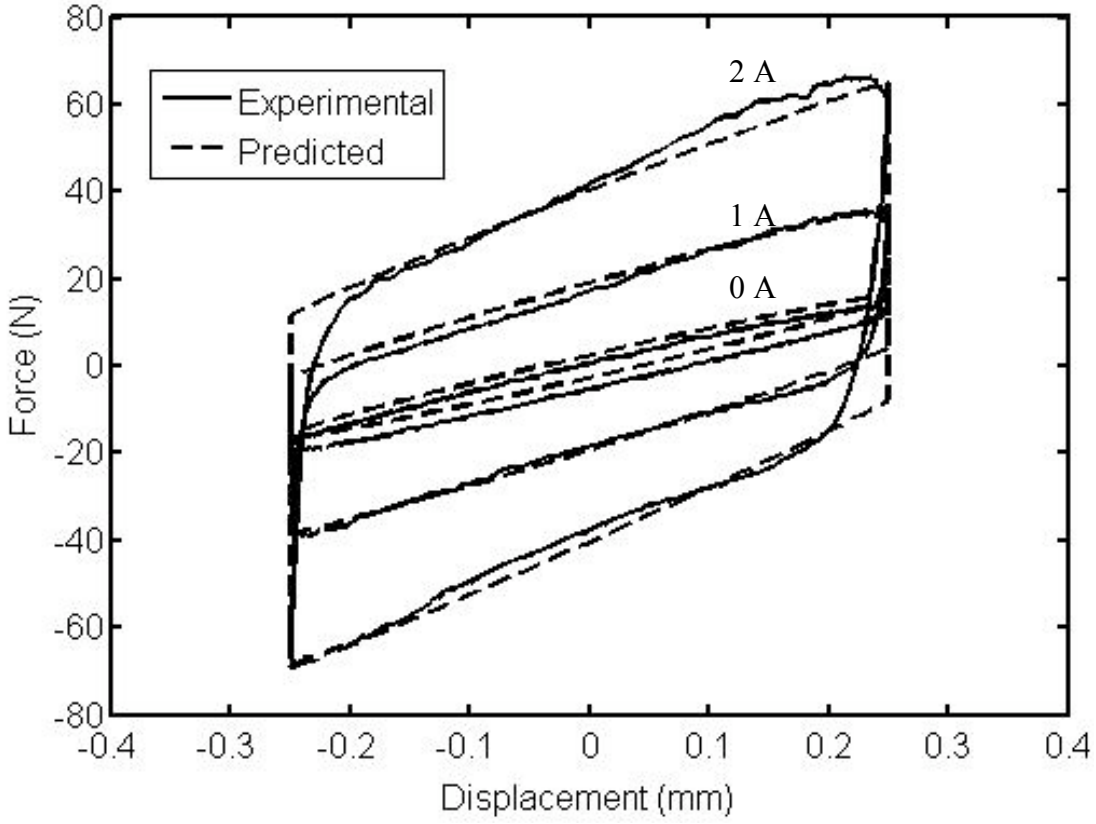

Figure 4.19 Predicted force using Bingham model and experimental force versus displacement for displacement amplitude of 0.25 mm, excitation frequency of 5 Hz and varying applied current.

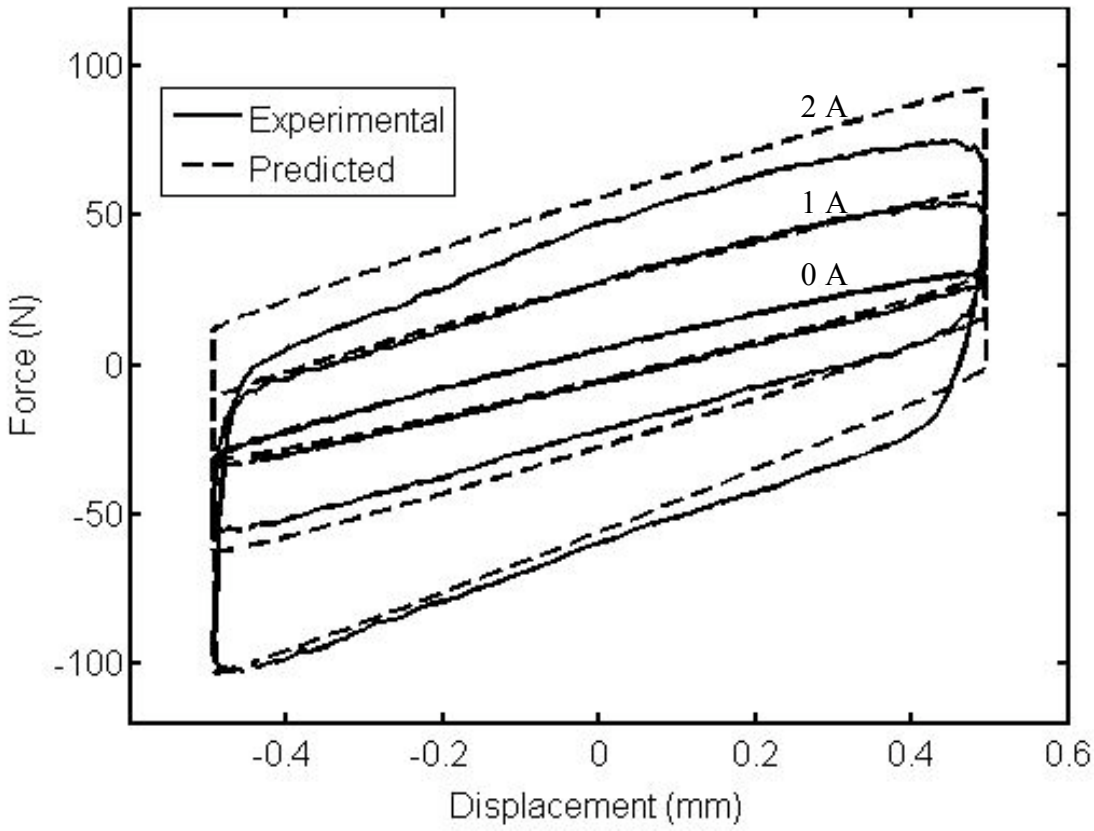

Figure 4.20 Predicted force using Bingham model and experimental force versus displacement for displacement amplitude of 0.5 mm, excitation frequency of 5 Hz and varying applied current.

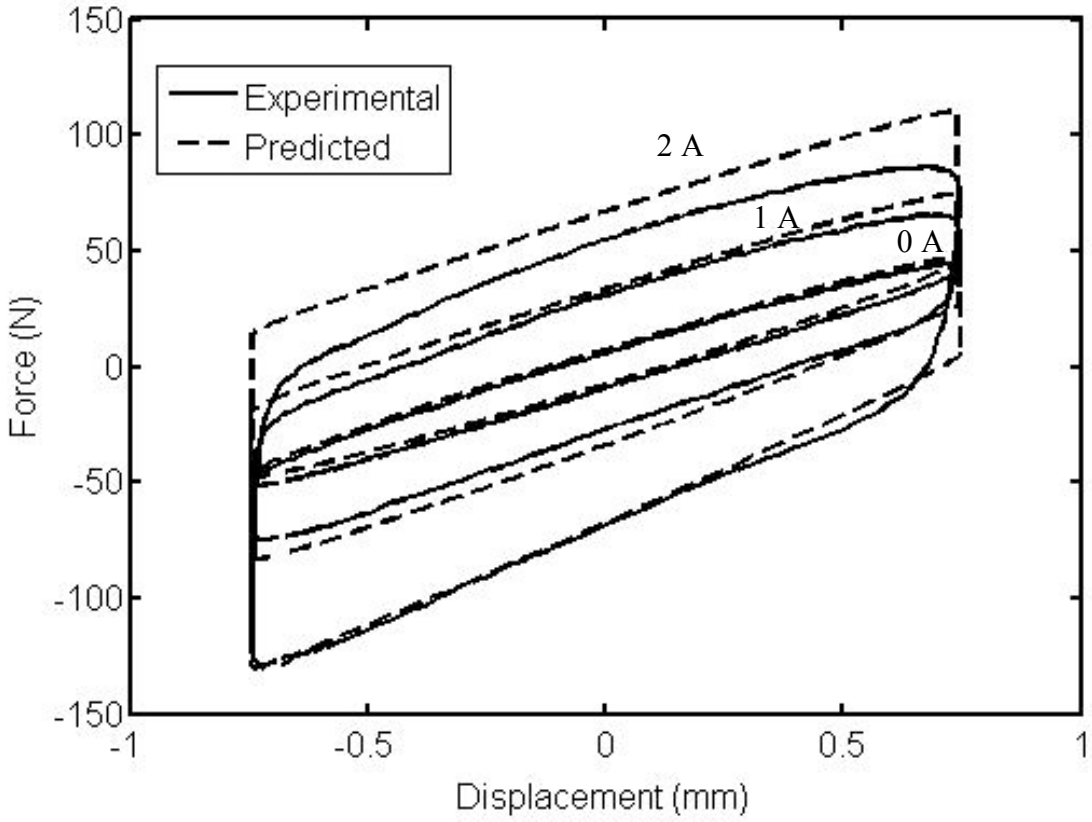

Figure 4.21 Predicted force using Bingham model and experimental force versus displacement for displacement amplitude of 0.75 mm, excitation frequency of 5 Hz and varying applied current.

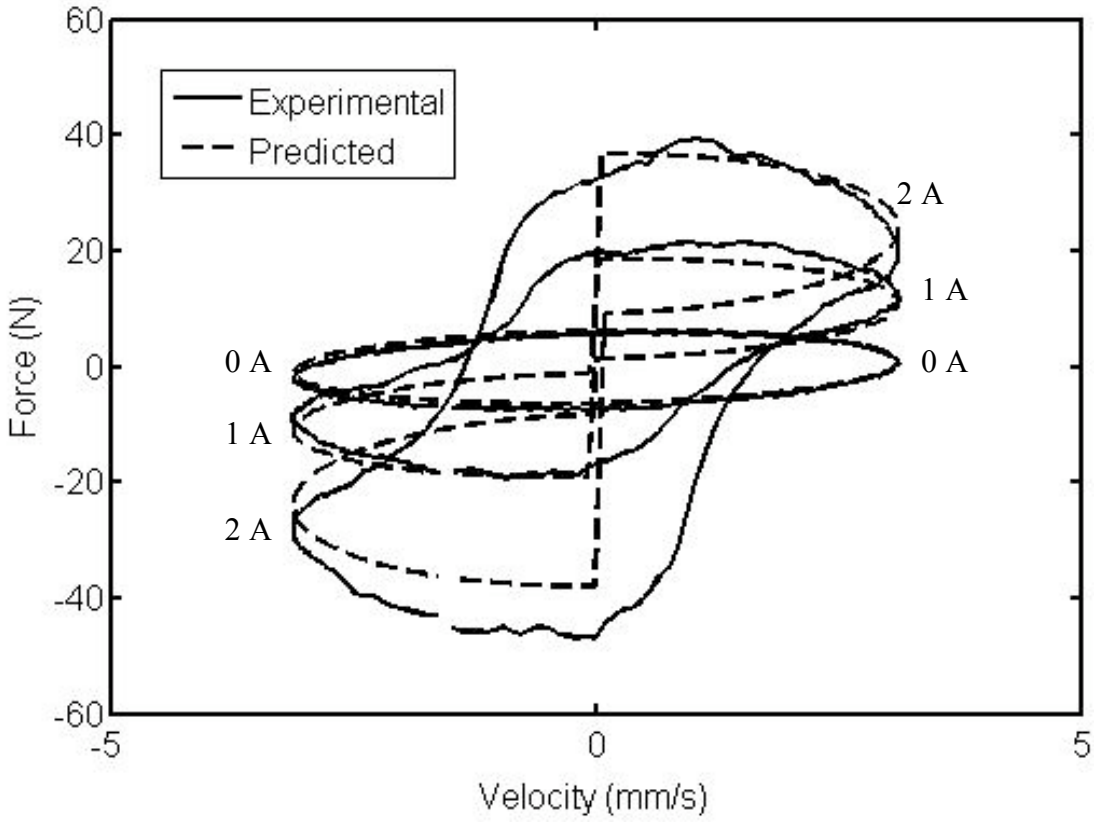

Figure 4.22 Predicted force using Bingham model and experimental force versus velocity for displacement amplitude of 0.1 mm, excitation frequency of 5 Hz and varying applied current.

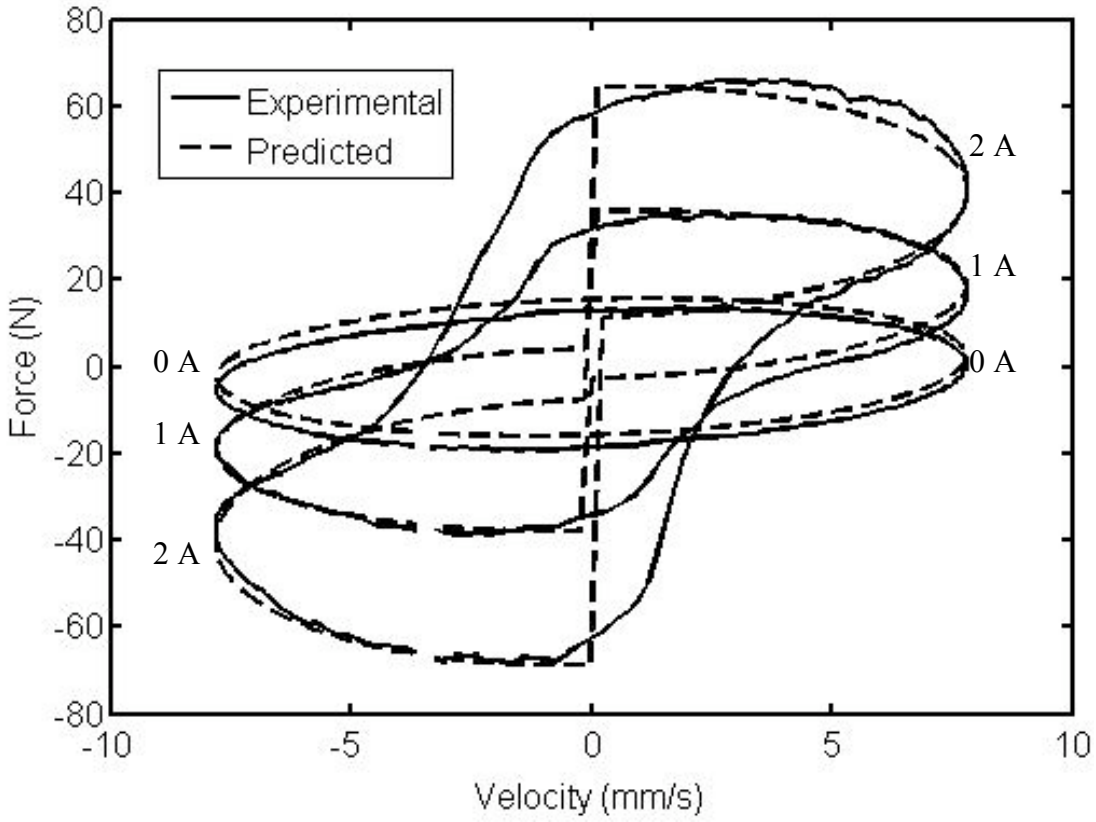

Figure 4.23 Predicted force using Bingham model and experimental force versus velocity for displacement amplitude of 0.25 mm, excitation frequency of 5 Hz and varying applied current.

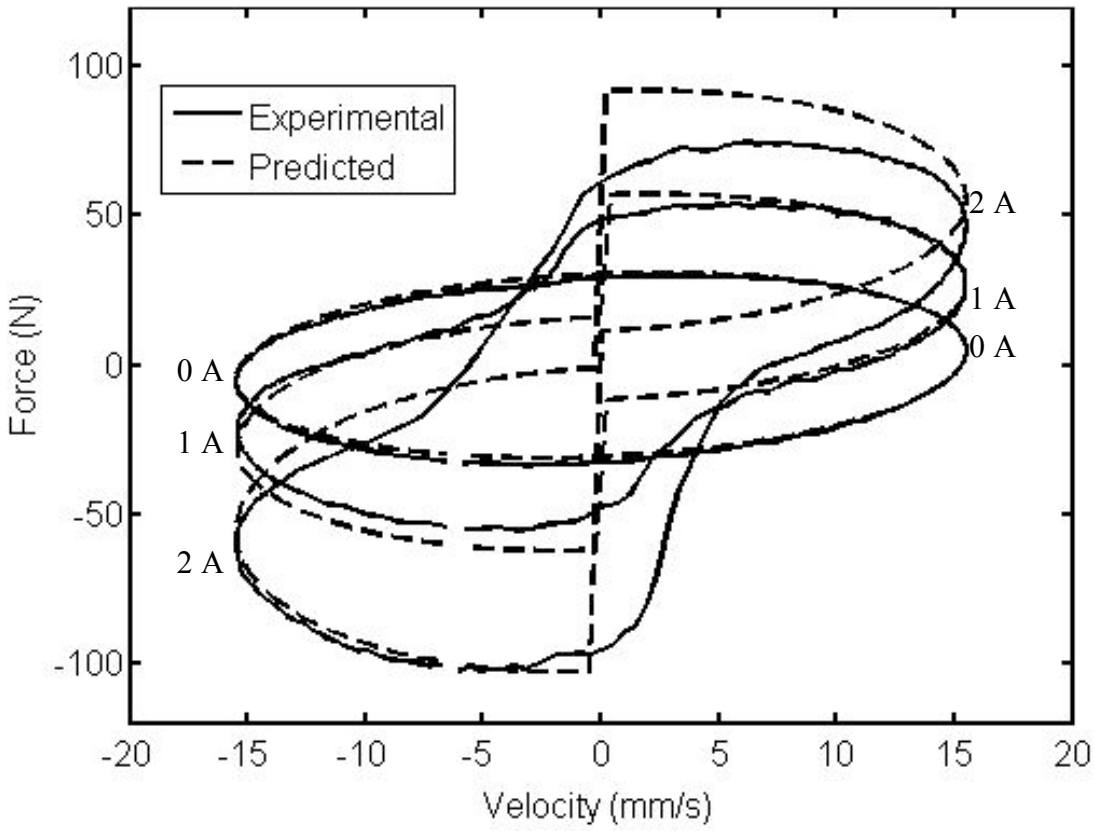

Figure 4.24 Predicted force using Bingham model and experimental force versus velocity for displacement amplitude of 0.5 mm, excitation frequency of 5 Hz and varying applied current.

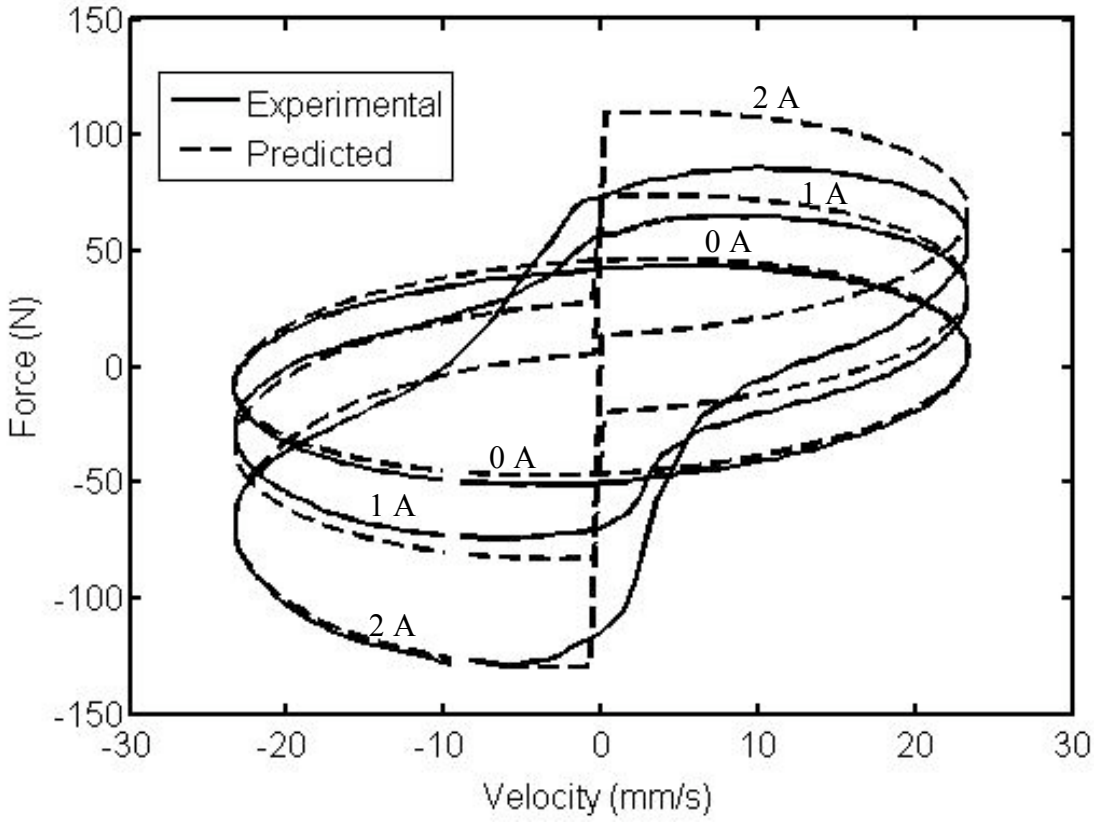

Figure 4.25 Predicted force using Bingham model and experimental force versus velocity for displacement amplitude of 0.75 mm, excitation frequency of 5 Hz and varying applied current.

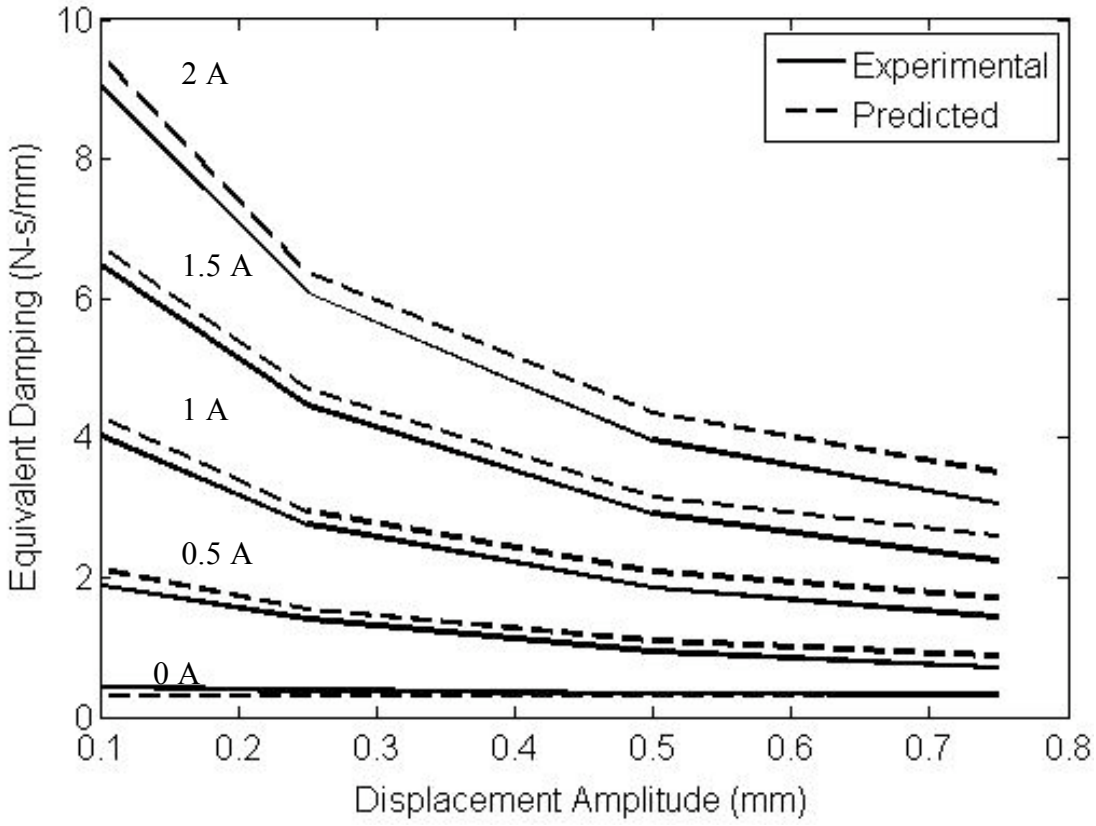

Figure 4.26 Predicted equivalent damping coefficient using Bingham model and experimental equivalent damping coefficient versus displacement for excitation frequency of 5 Hz and varying applied current.

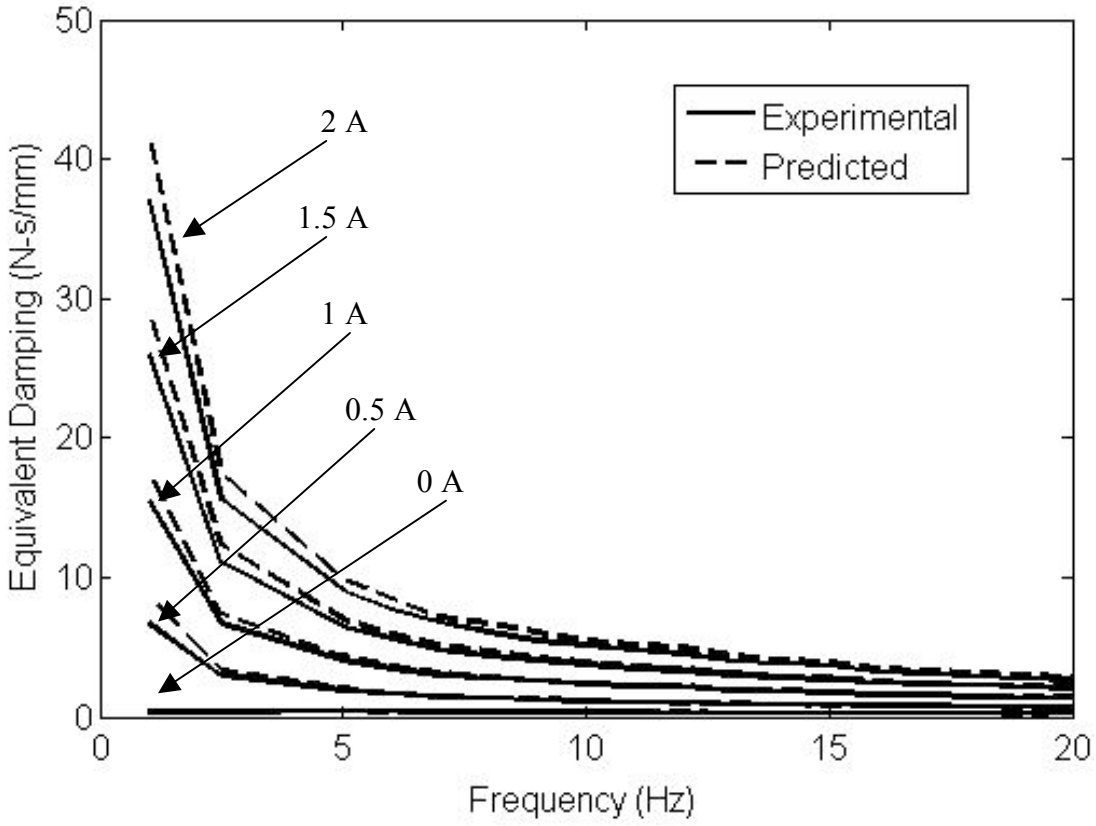

Figure 4.27 Predicted equivalent damping coefficient using Bingham model and experimental equivalent damping coefficient versus frequency for displacement amplitude of 0.1 mm and varying applied current.

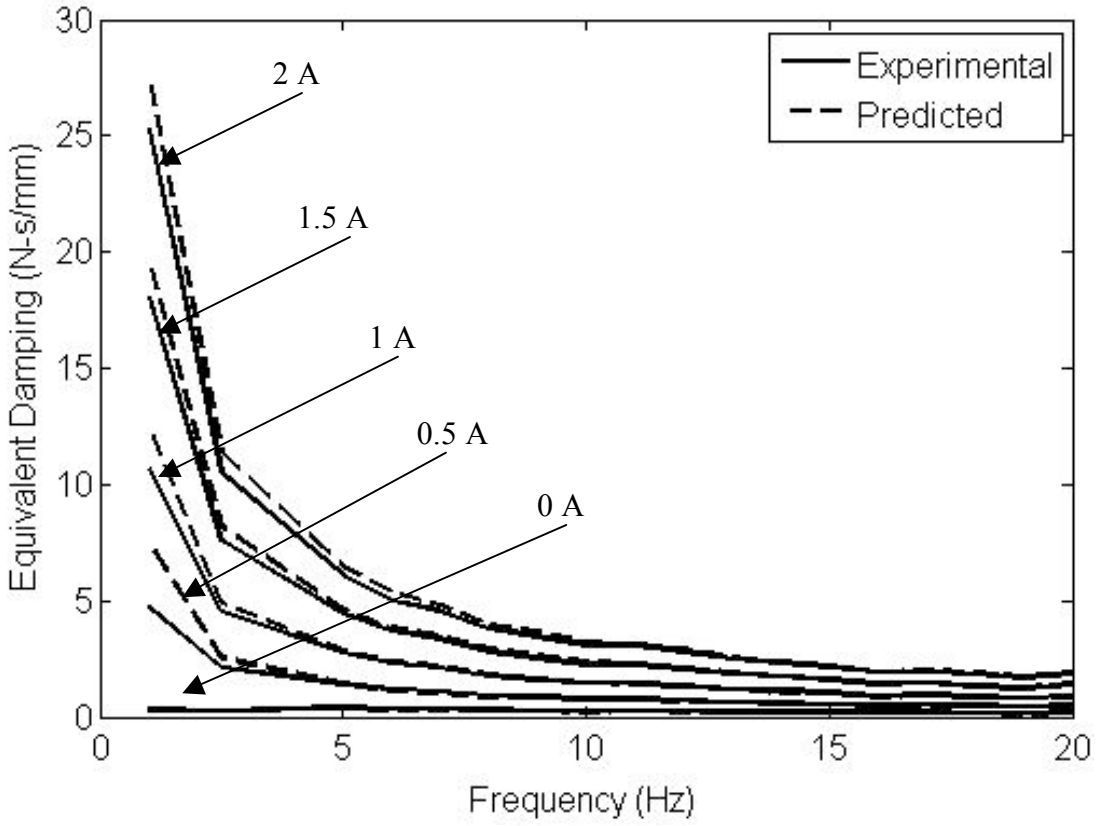

Figure 4.28 Predicted equivalent damping coefficient using Bingham model and experimental equivalent damping coefficient versus frequency for displacement amplitude of 0.25 mm and varying applied current.

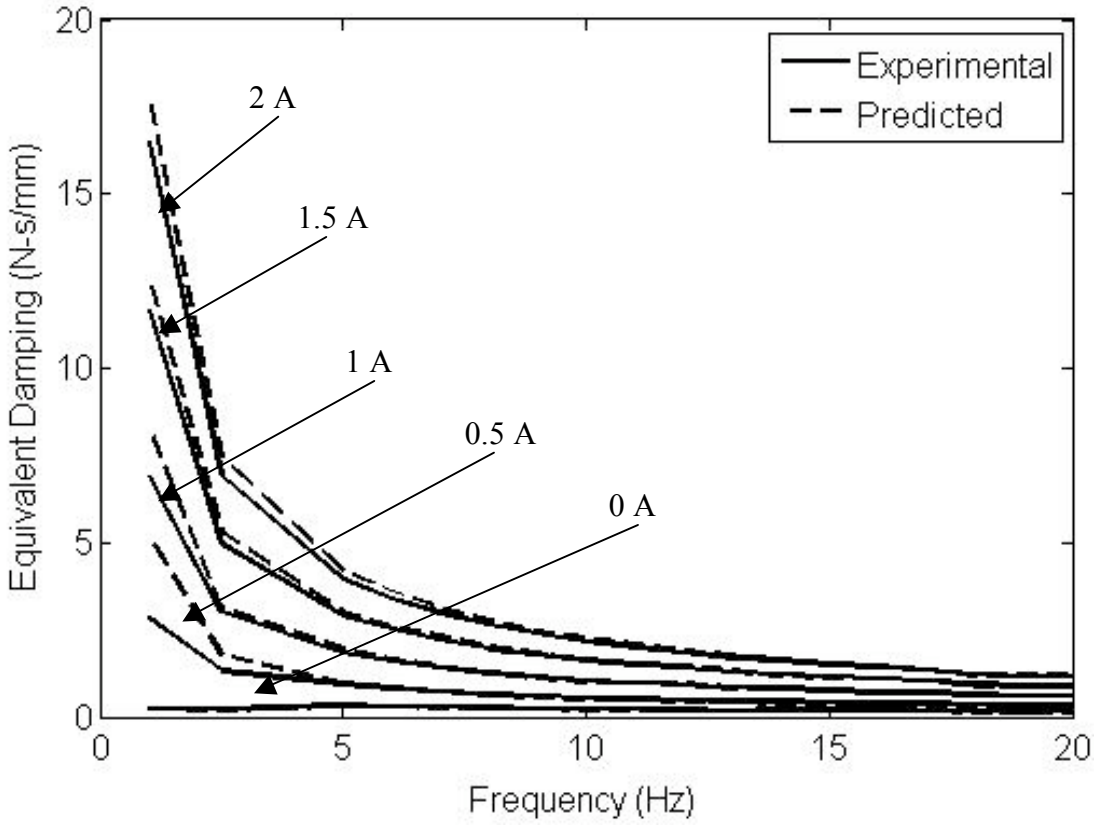

Figure 4.29 Predicted equivalent damping coefficient using Bingham model and experimental equivalent damping coefficient versus frequency for displacement amplitude of 0.5 mm and varying applied current.

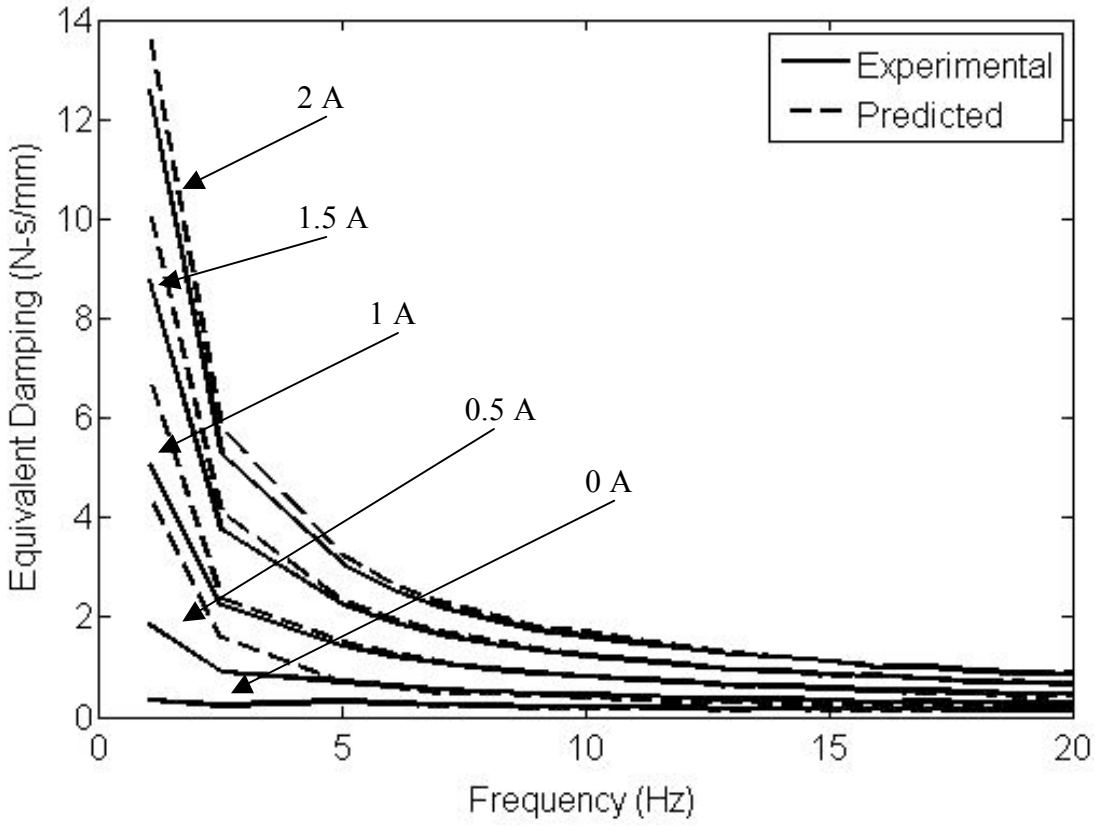

Figure 4.30 Predicted equivalent damping coefficient using Bingham model and experimental equivalent damping coefficient versus frequency for displacement amplitude of 0.1 mm and varying applied current.

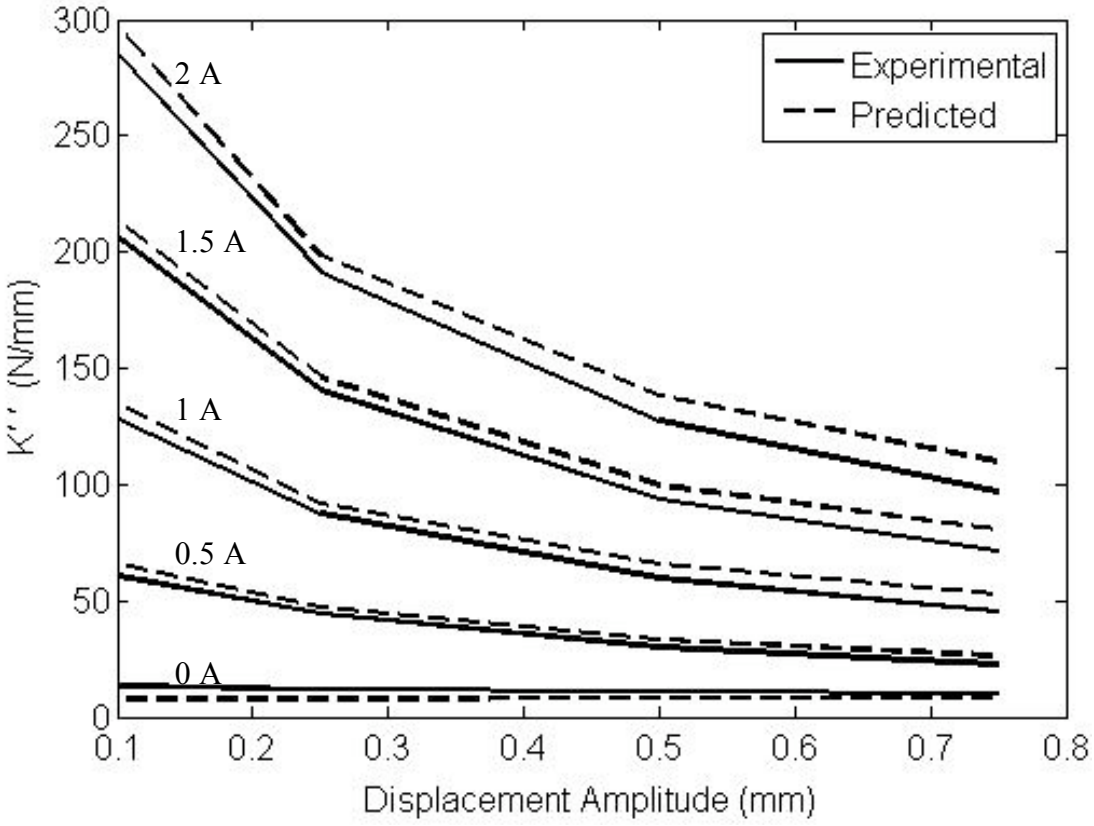

Figure 4.31 Predicted quadrature stiffness using Bingham model and experimental quadrature stiffness versus displacement amplitude for excitation frequency of 5 Hz and varying applied current.

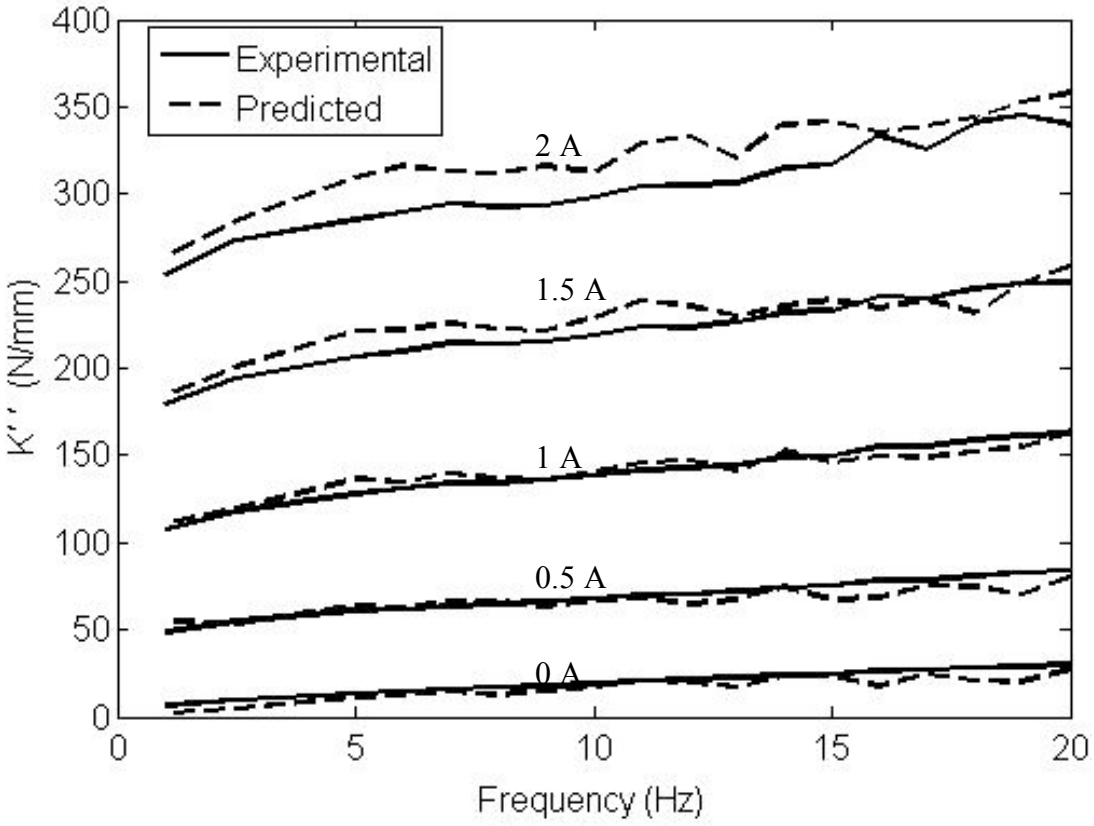

Figure 4.32 Predicted quadrature stiffness using Bingham model and experimental quadrature stiffness versus frequency for displacement amplitude of 0.1 mm and varying applied current.

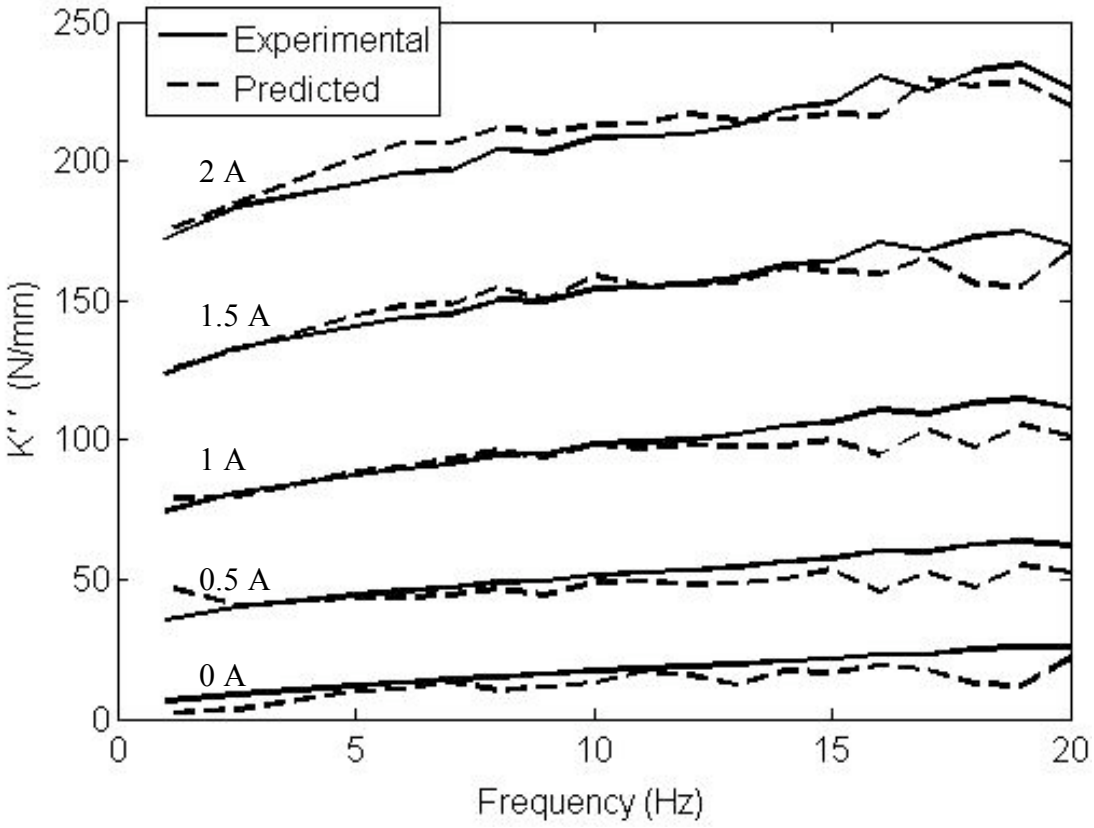

Figure 4.33 Predicted quadrature stiffness using Bingham model and experimental quadrature stiffness versus frequency for displacement amplitude of 0.25 mm and varying applied current.

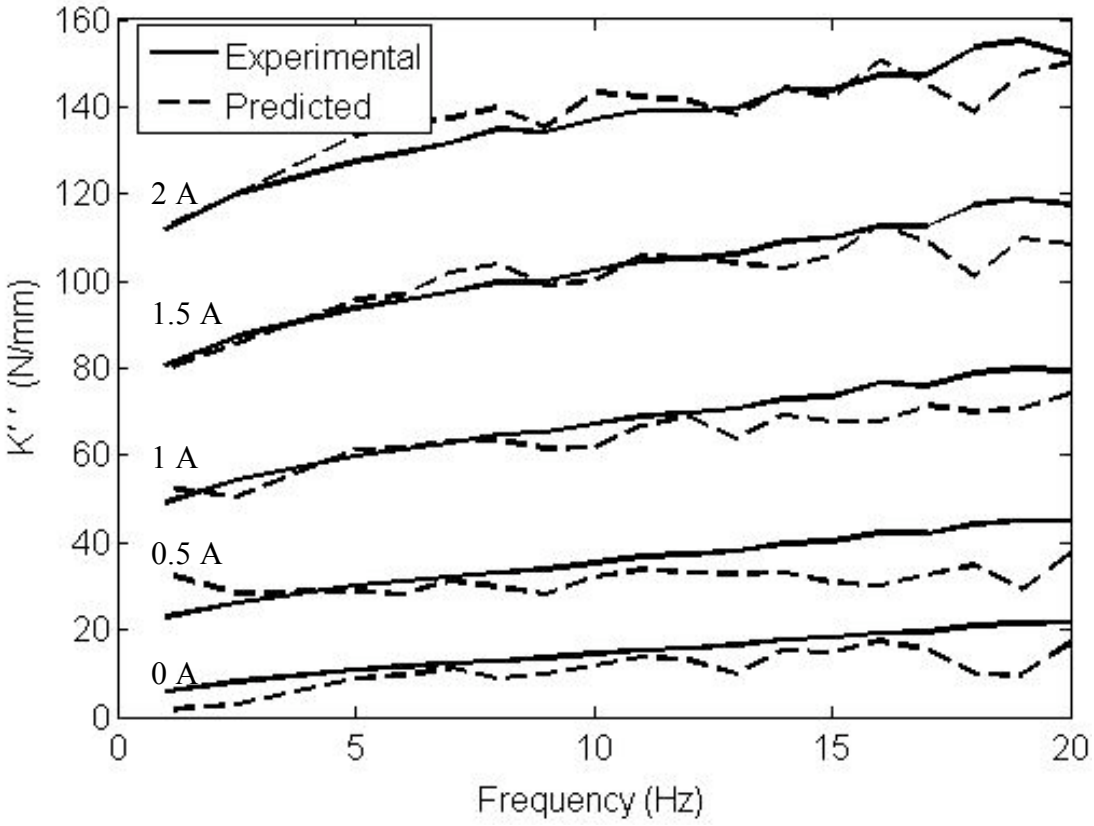

Figure 4.34 Predicted quadrature stiffness using Bingham model and experimental quadrature stiffness versus frequency for displacement amplitude of 0.5 mm and varying applied current.

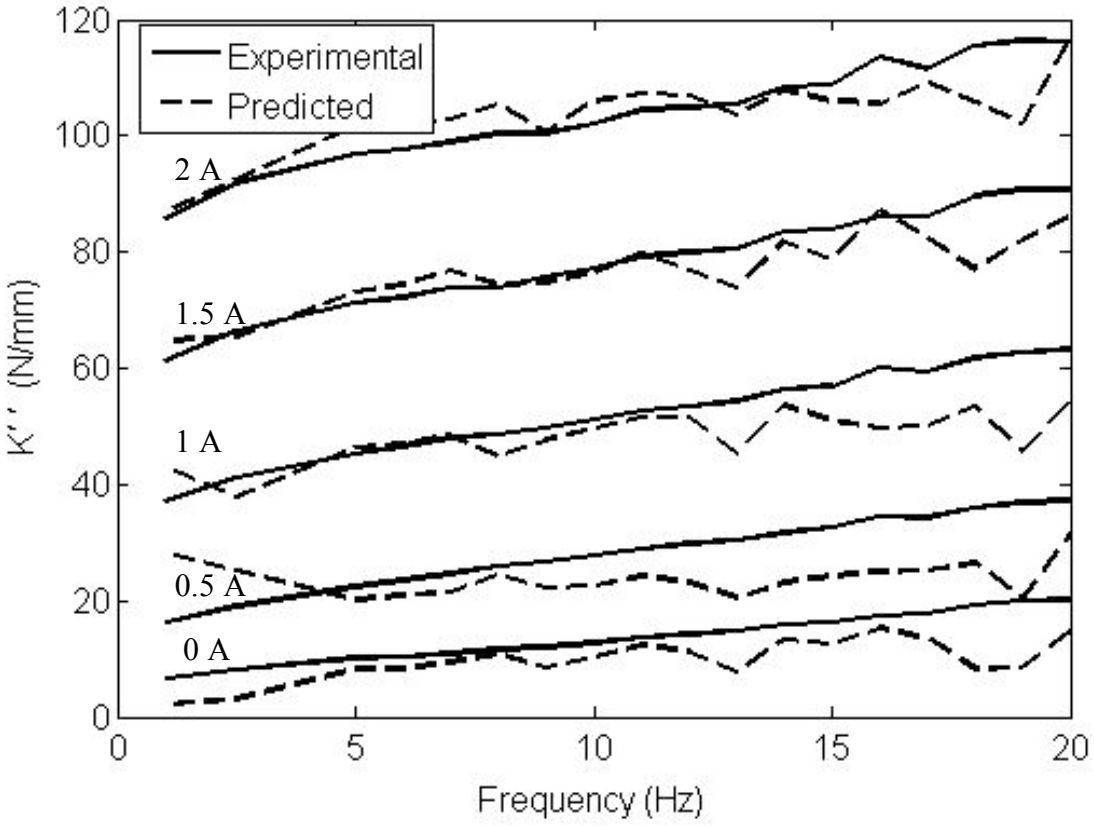

Figure 4.35 Predicted quadrature stiffness using Bingham model and experimental quadrature stiffness versus frequency for displacement amplitude of 0.75 mm and varying applied current.

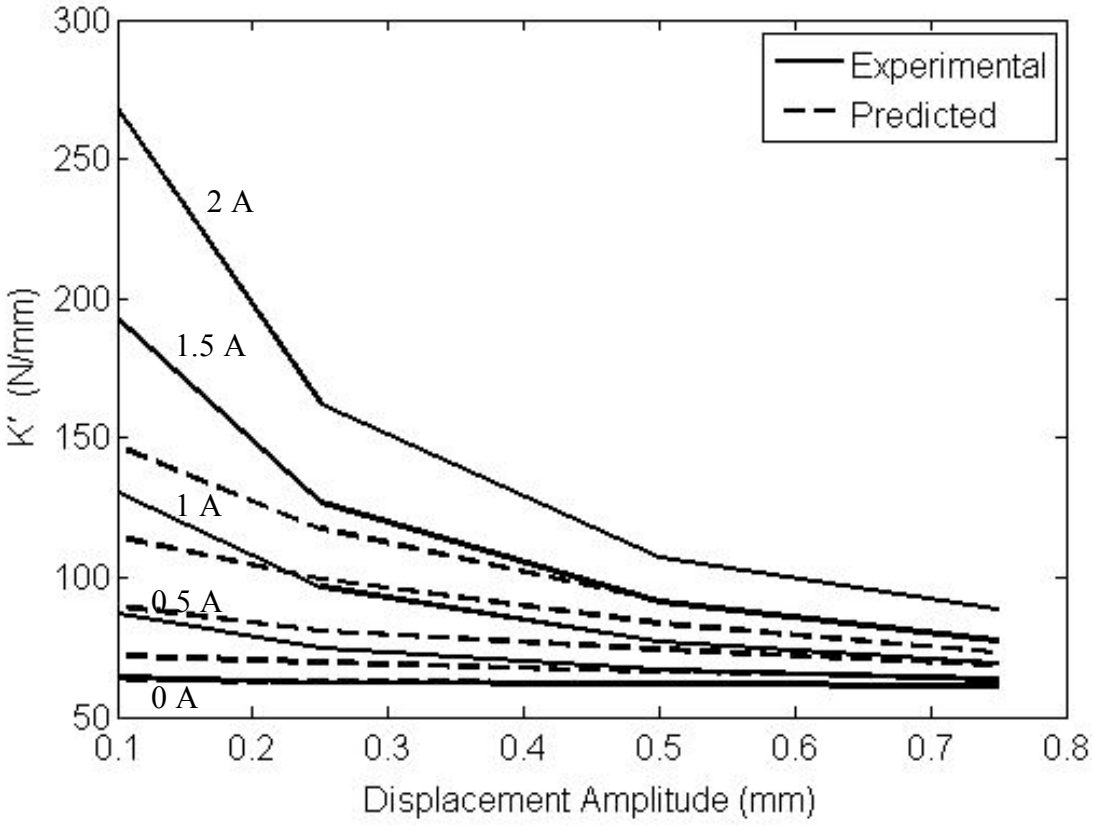

Figure 4.36 Predicted storage stiffness using Bingham model and experimental storage stiffness versus displacement amplitude for excitation frequency of 5 Hz and varying applied current.

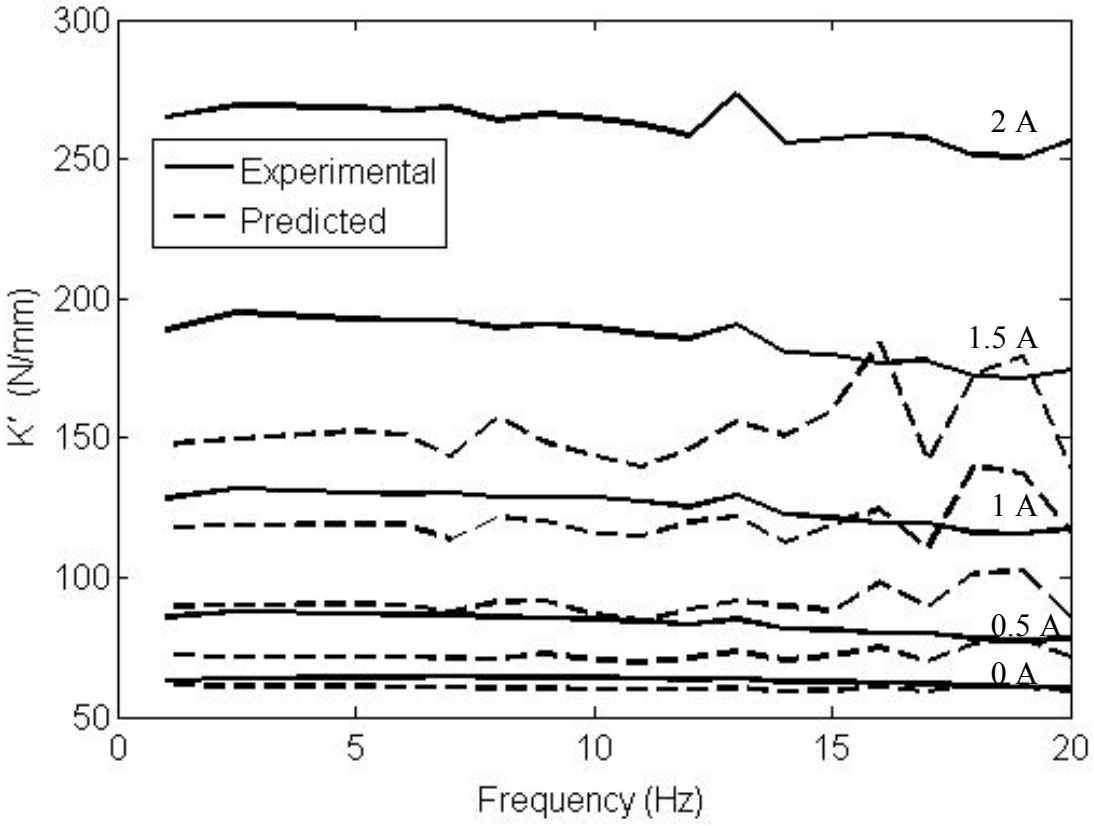

Figure 4.37 Predicted storage stiffness using Bingham model and experimental storage stiffness versus frequency for displacement amplitude of 0.1 mm and varying applied current.

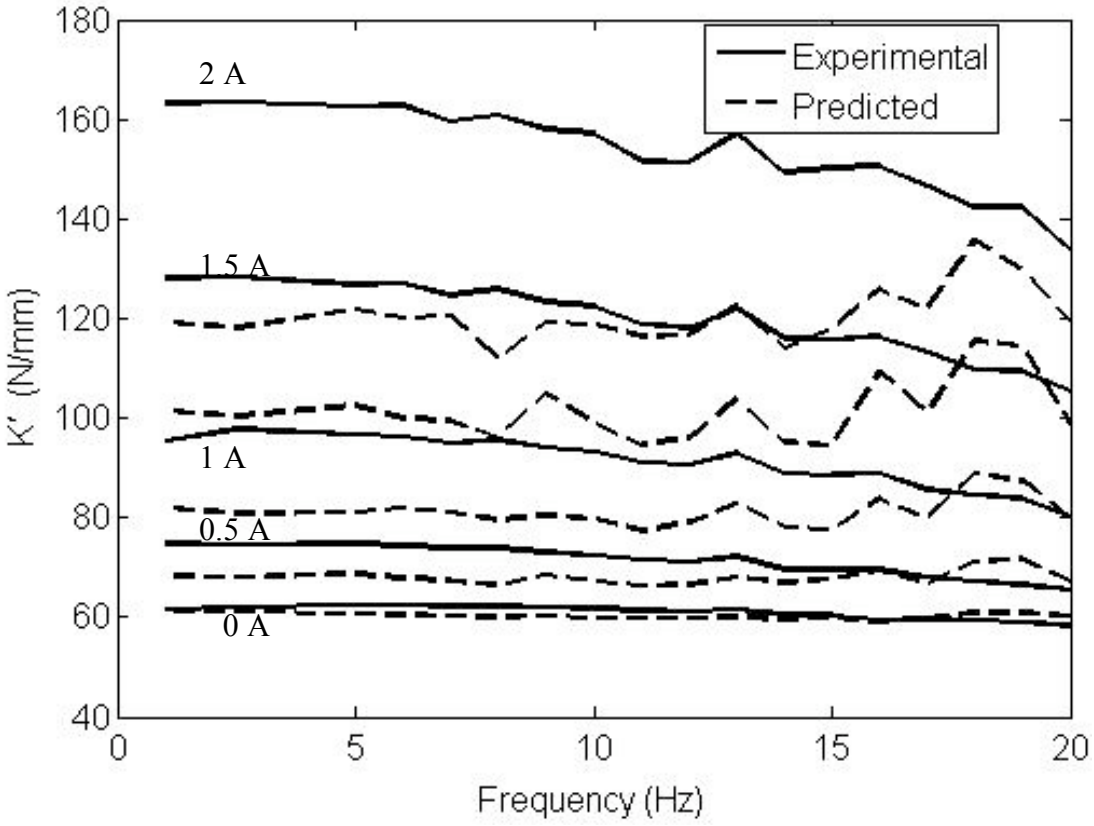

Figure 4.38 Predicted storage stiffness using Bingham model and experimental storage stiffness versus frequency for displacement amplitude of 0.25 mm and varying applied current.

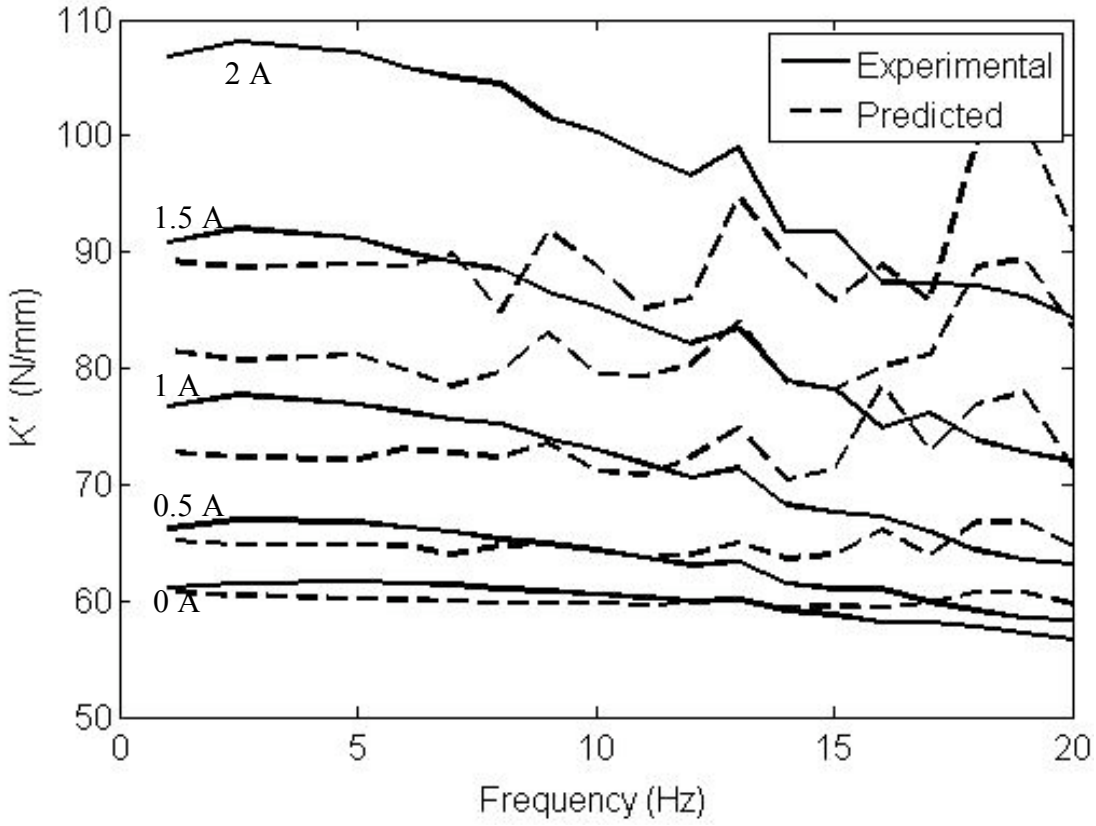

Figure 4.39 Predicted storage stiffness using Bingham model and experimental storage stiffness versus frequency for displacement amplitude of 0.5 mm and varying applied current.

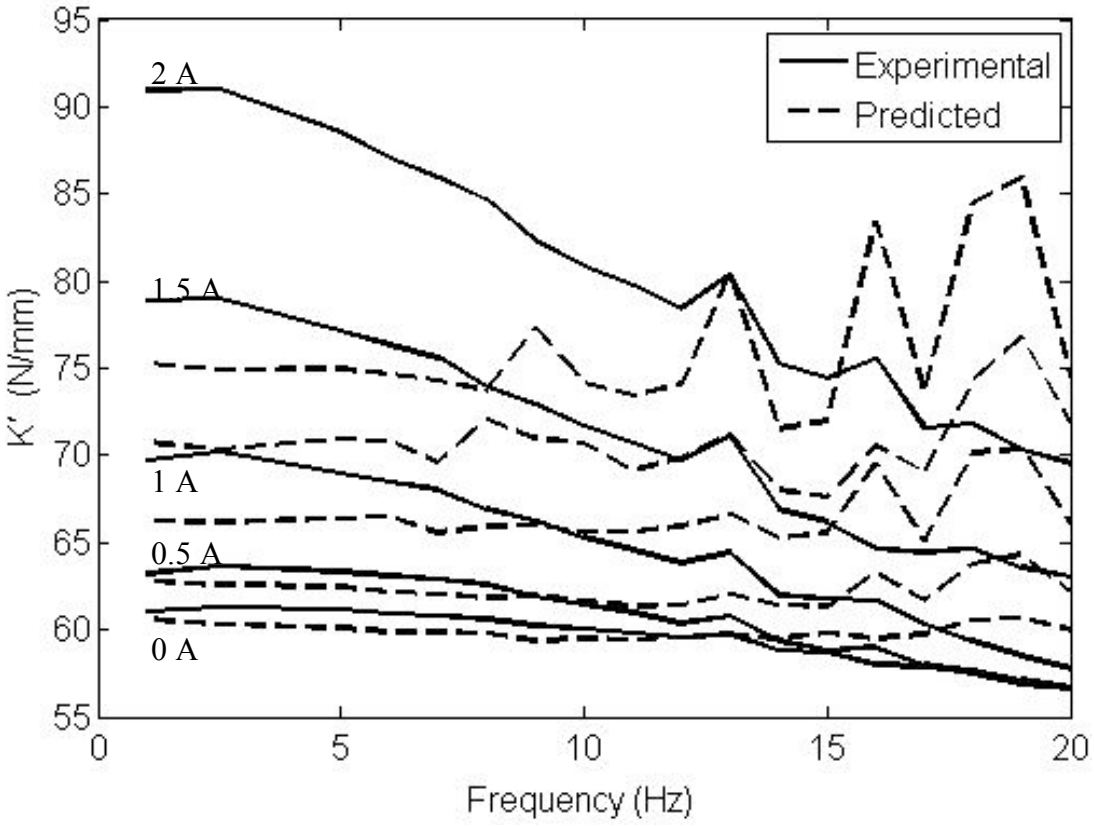

Figure 4.40 Predicted storage stiffness using Bingham model and experimental storage stiffness versus frequency for displacement amplitude of 0.75 mm and varying applied current.

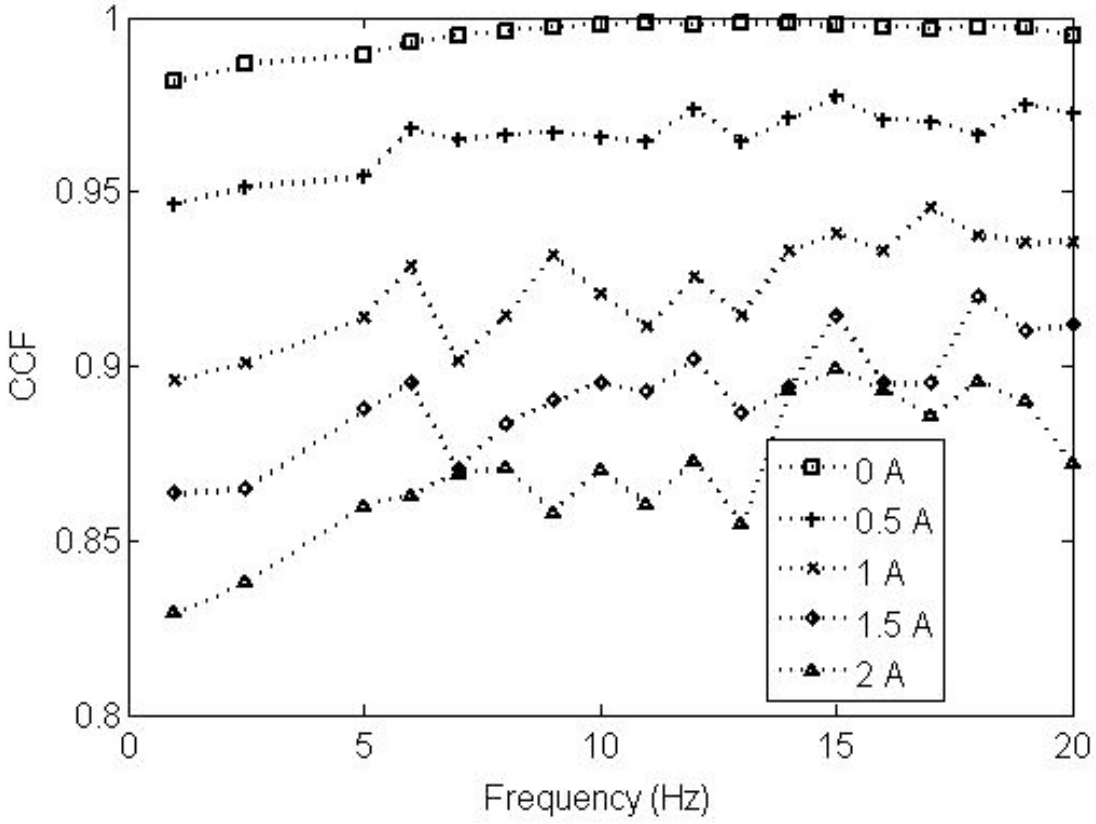

Figure 4.41 CCF versus frequency for displacement amplitude of 0.1 mm. CCF is comparing the force-displacement cycle predicted by the Bingham model to that generated from the experimental data.

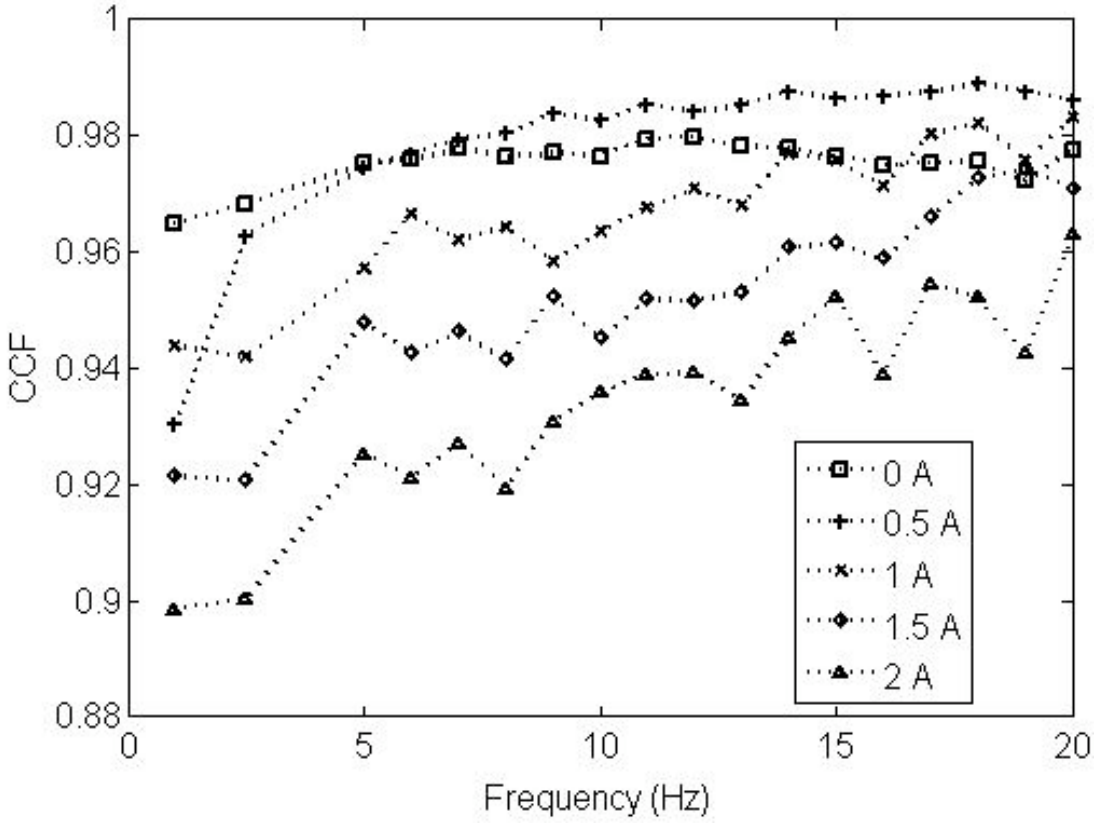

Figure 4.42 CCF versus frequency for displacement amplitude of 0.25 mm. CCF is comparing the force-displacement cycle predicted by the Bingham model to that generated from the experimental data.

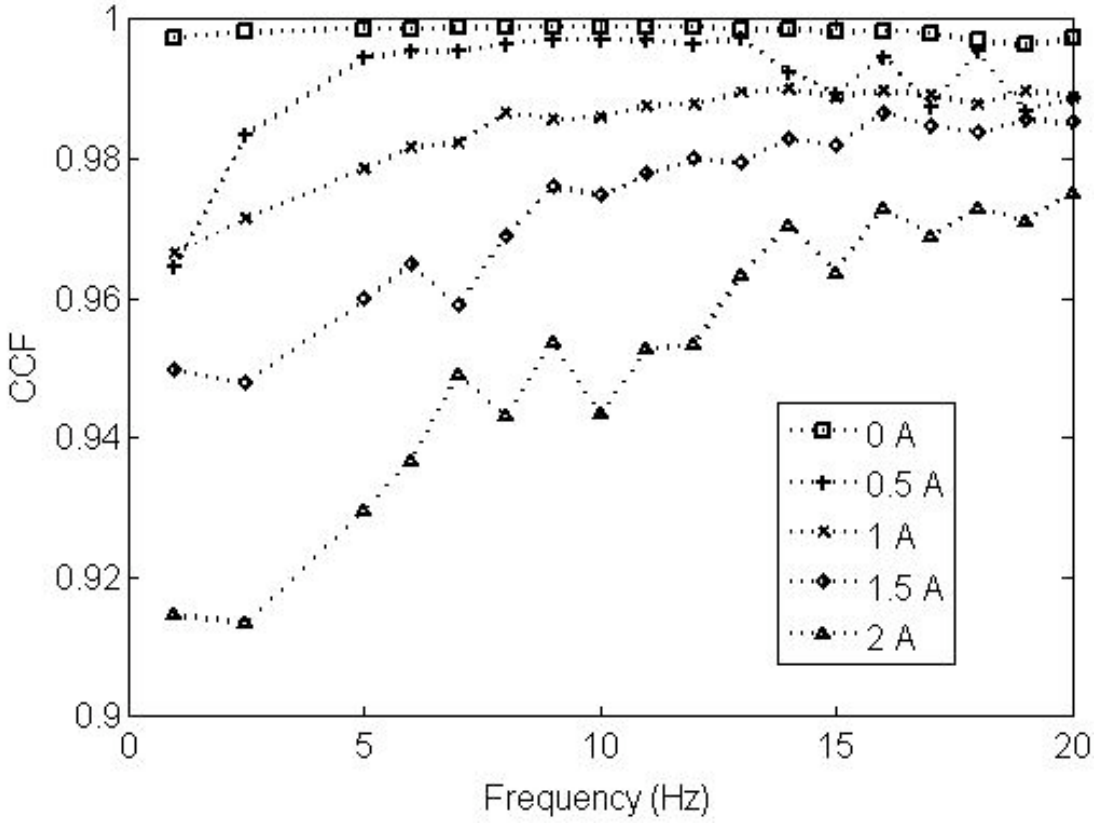

Figure 4.43 CCF versus frequency for displacement amplitude of 0.5 mm. CCF is comparing the force-displacement cycle predicted by the Bingham model to that generated from the experimental data.

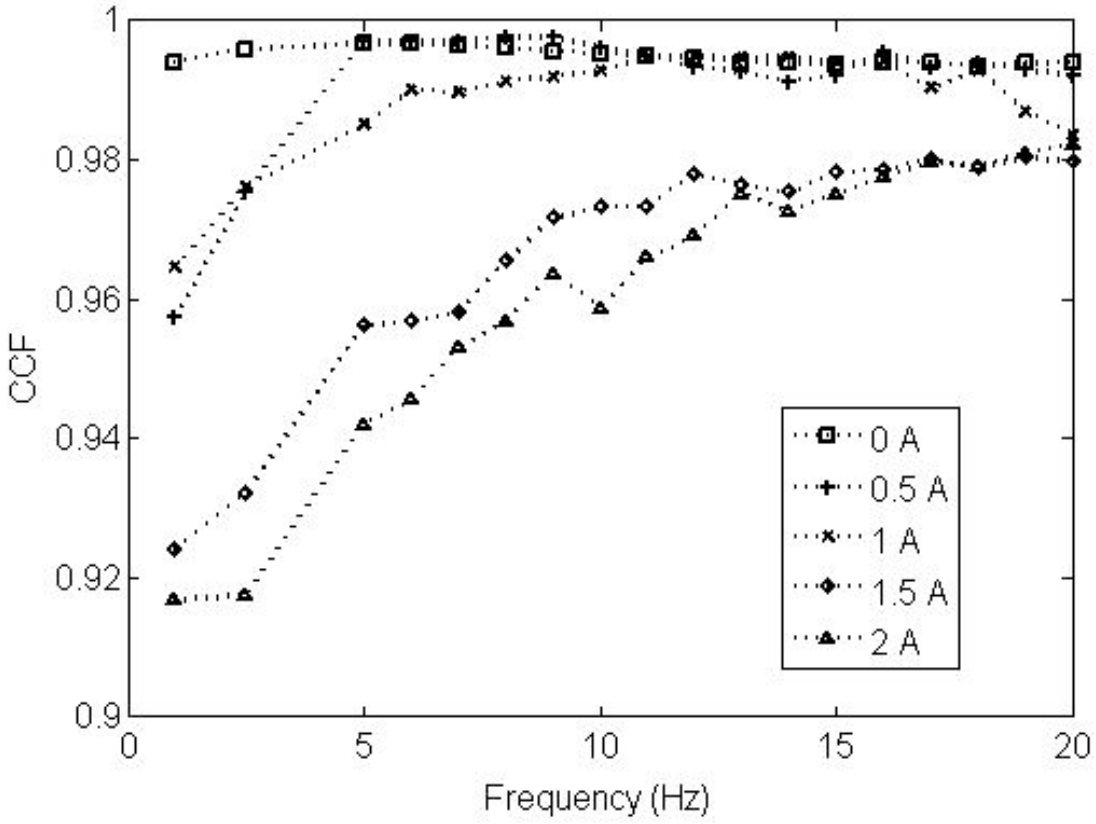

Figure 4.44 CCF versus frequency for displacement amplitude of 0.75 mm. CCF is comparing the force-displacement cycle predicted by the Bingham model to that generated from the experimental data.

Chapter 5: Nonlinear Hysteresis Model

Choi and Wereley introduced a nonlinear hysteresis model and showed it was better able to capture the behavior of an MR isolator than the Bingham model [22]. The nonlinear hysteresis model replaced the zero speed force step discontinuity present in the Bingham plastic model with more gradual transition through the low-speed regime. This resulted in a more accurate portrayal of the hysteresis characteristics of the MR isolator.

In order to more accurately describe the MR behavior through the low-speed regime the signum function, which is used in the Bingham model and is the cause for the force step discontinuity at zero speed, is replaced with the hypertangent function.

5.1 Total Isolator Force

The total isolator force described by the nonlinear hysteresis model is of a similar form to that described by the Bingham plastic model, which is given by equation 4.30. The force of the isolator given my the nonlinear hysteresis model is

$$F_{damper} = Kx + C\dot{x} + F_y \tanh\left[\lambda_2(\dot{x} + \lambda_1 x)\right] \tag{5.1}$$

where,

$$K = K_{el} \tag{5.1a}$$

$$C = \left(C_{el} + \frac{12A_p L\mu}{bd^3} + \frac{bL\mu}{d} + \frac{3\pi\mu r_p^4}{2(x_0 + x)^3} \right) \tag{5.1b}$$

$$F_y = \tau_y \left(\frac{2A_p L_a}{d} + bL_a + \frac{4\pi r_a^3}{3(x_0 + x)} \right) \tag{5.1c}$$

These model parameters are identified in the same manner and take the same values as in the Bingham plastic model; μ is 0.09 Pa-s, C_{el} is 300 N-s/m, K_{el} is identified using the displacement averaged stiffness technique and its values shown in figures 4.10-4.13, and τ_y is identified using the velocity averaged stiffness technique and its values shown in figures 4.14-4.17.

λ_1 and λ_2 are characteristic parameters used to capture the hysteresis loop. The parameter λ_1 accounts for the width of the hysteresis loop and λ_2 accounts for the slope of the hysteresis loop. Variation of these two parameters allows the model to match an experimental hysteresis plot. To fully establish the structure of the model these parameters were found using a curve-fitting method matching the experimental hysteresis plots. Figures 5.1-5.4 show the variation of λ_1 with frequency for displacement amplitudes of 0.1 mm, 0.25 mm, 0.5 mm and 0.75 mm, respectively. This parameter is found to be strongly dependent upon excitation frequency, displacement amplitude and the applied current. The variation of λ_2 over the same conditions is shown in figures 5.5-5.8, this parameters is found to have a strong dependence upon excitation frequency and displacement amplitude and a weaker correlation with the applied current.

5.2 Model Results

The nonlinear hysteresis model is better able to capture the behavior of the MR isolator than is the Bingham plastic model. Figures 5.9-5.12 show the force-displacement plots for displacement amplitudes of 0.1 mm, 0.25 mm, 0.5 mm, and 0.75 mm, respectively. The excitation frequency is constant at 5 Hz. The solid line

represents experimental force data and the dashed line represents the model predicted force. The hysteresis model correlates well with experimental data. The force-velocity plots for the same conditions are shown in figures 5.13-5.16. The ability of the model to capture the hysteresis behavior is evident, especially at low-speed when the Bingham model failed to accurately predict isolator force.

In order to verify the ability of the hysteresis model to predict isolator damping a comparison between the equivalent damping coefficient and quadrature stiffness predicted by the model and those found experimentally was made. Figures 5.17-5.20 show the variation of the equivalent damping coefficient with frequency while figures 5.21-5.24 show quadrature stiffness versus frequency for displacement amplitudes of 0.1 mm, 0.25 mm, 0.5 mm and 0.75 mm, respectively. The predicted damping of the isolator correlates well with that found through experimental measurements.

In figures 5.25-5.28 the variation of storage stiffness with frequency for displacement amplitudes of 0.1 mm, 0.25 mm, 0.5 mm, and 0.75 mm, is shown. The nonlinear hysteresis model captures the behavior of the storage stiffness very well over much of the frequency range. However, at higher frequencies (above 15 Hz), the predicted stiffness begins to deviate from the experimental stiffness. The inclusion of a hysteresis loop, which resulted from accurately capturing the transition behavior of the MR yield force, produced a model that was much better at predicting the stiffness of the MR isolator.

In order to study the ability of the nonlinear hysteresis model to predict the MR isolators force quantitatively the complex correlation coefficient (CCF) was used,

which compares the shape and phase of the model fit. A CCF of 1 indicates a perfect model fit. Figures 5.29-5.32 show the CCF versus frequency of excitation. As can be seen the lowest CCF is CCF=0.965 occurring at a displacement amplitude of 0.25 mm. This is much better than the Bingham model, which produced a CCF as low as 0.85. The nonlinear hysteresis model shows a much better ability to track the shape of the force-displacement plots.

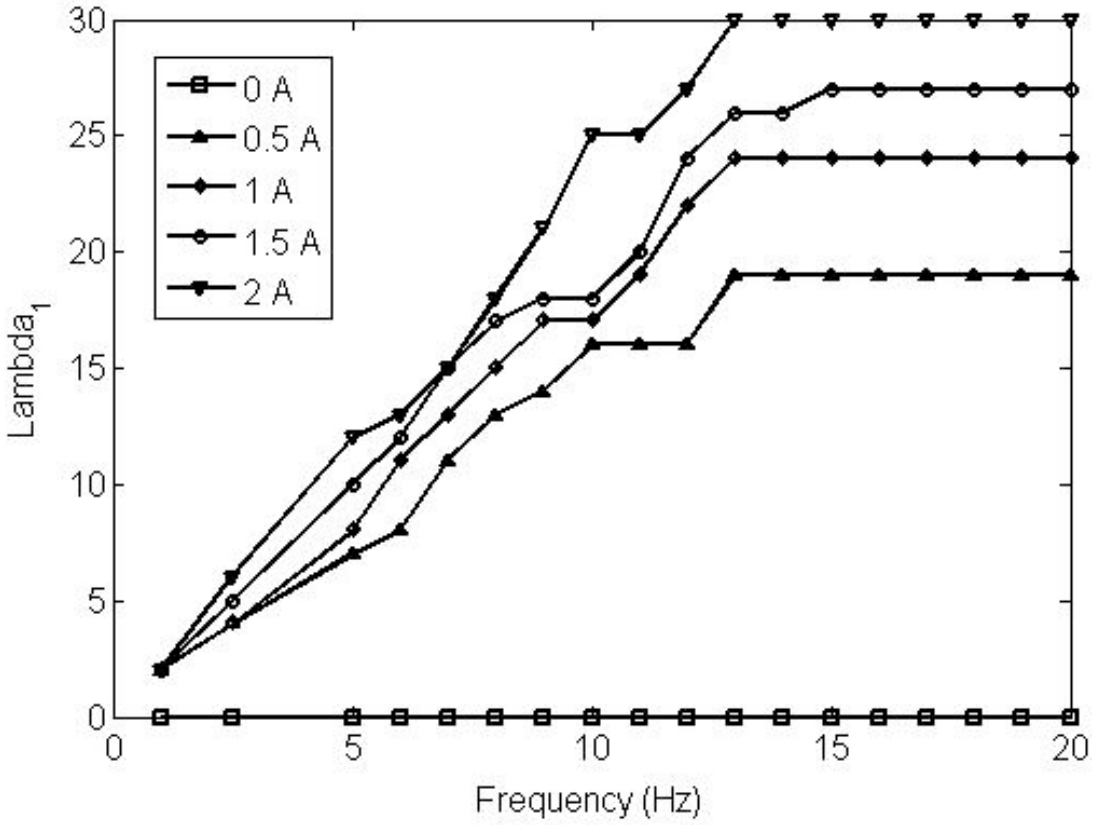

Figure 5.1 λ_1 versus frequency for displacement amplitude of 0.1 mm and varying applied current.

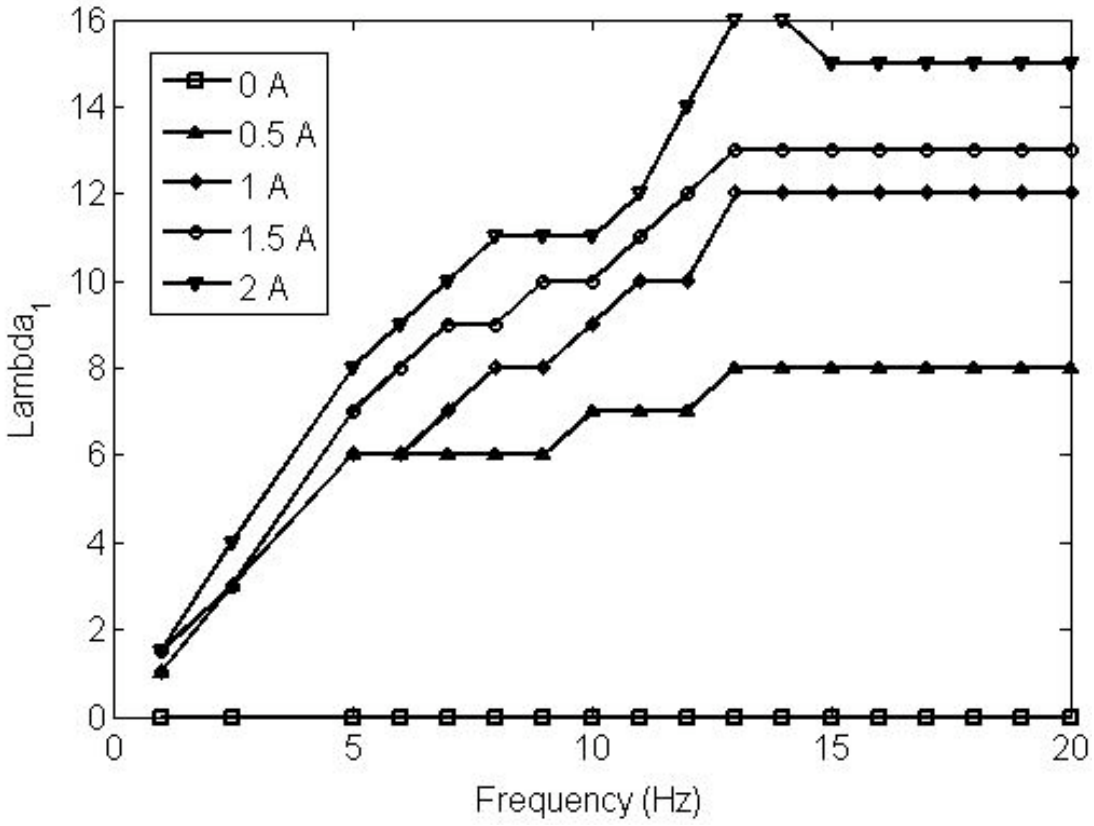

Figure 5.2 λ_1 versus frequency for displacement amplitude of 0.25 mm and varying applied current.

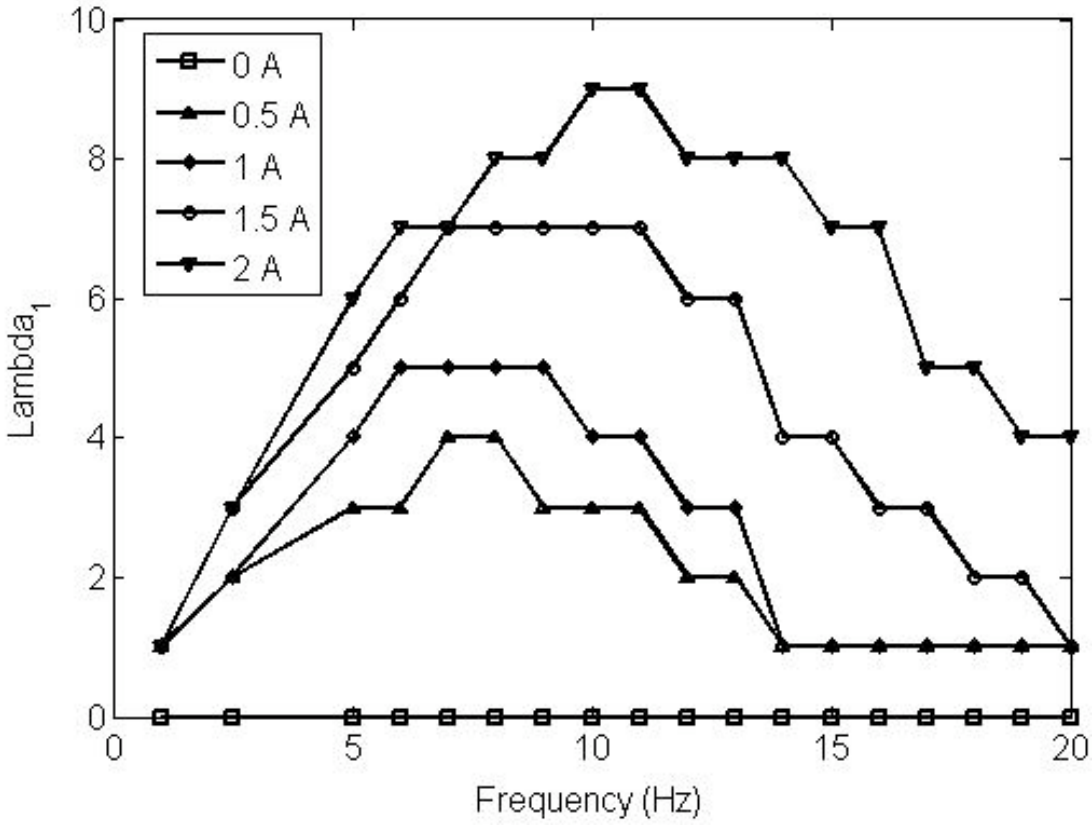

Figure 5.3 λ_1 versus frequency for displacement amplitude of 0.5 mm and varying applied current.

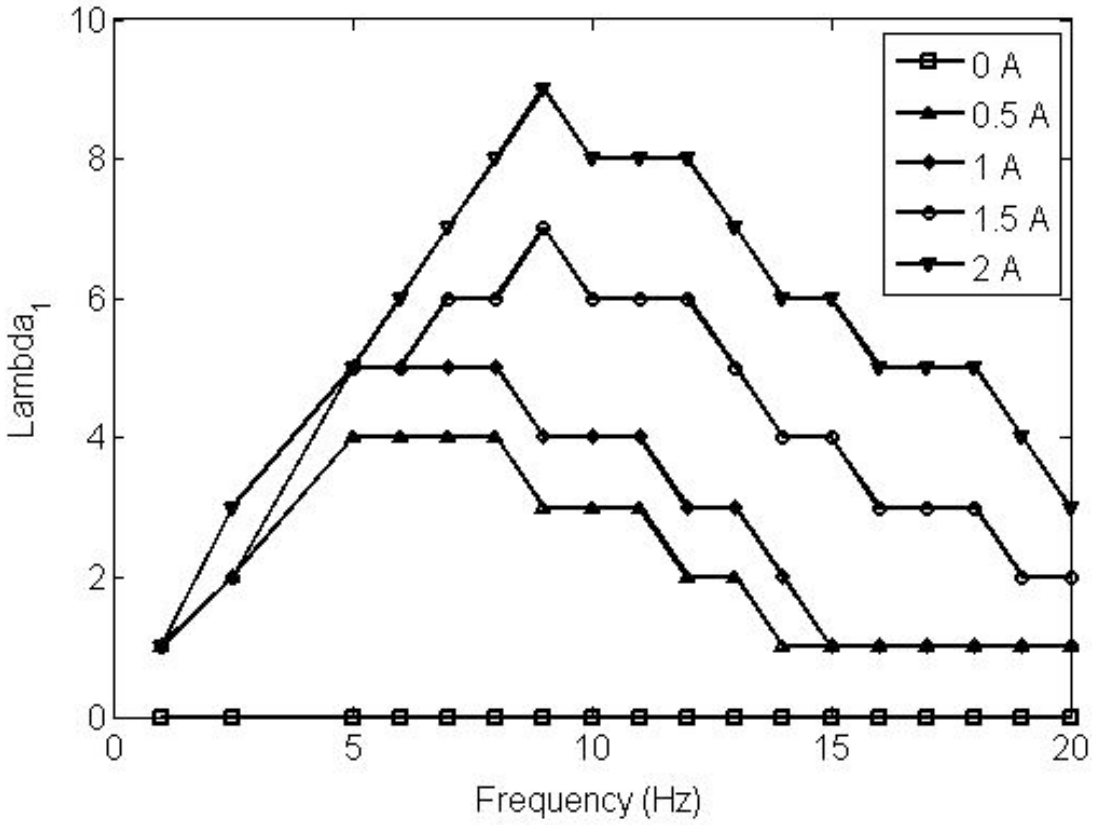

Figure 5.4 λ_1 versus frequency for displacement amplitude of 0.75 mm and varying applied current.

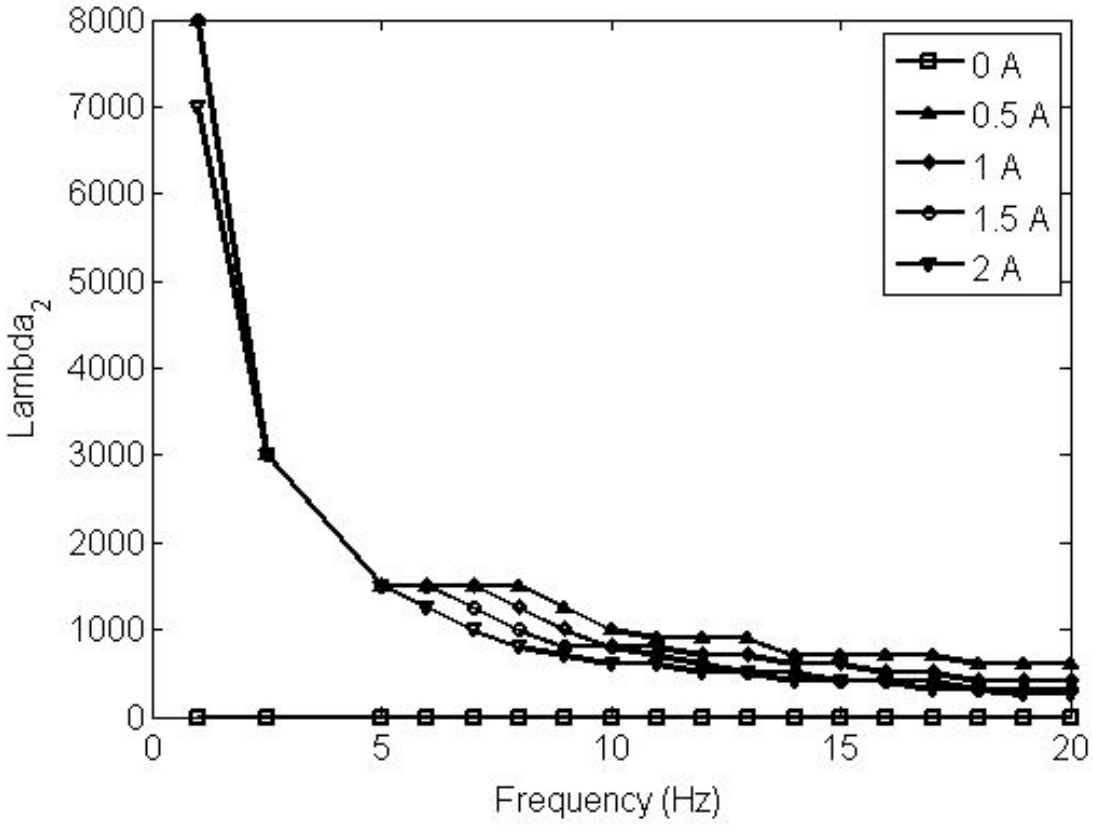

Figure 5.5 λ_2 versus frequency for displacement amplitude of 0.1 mm and varying applied current.

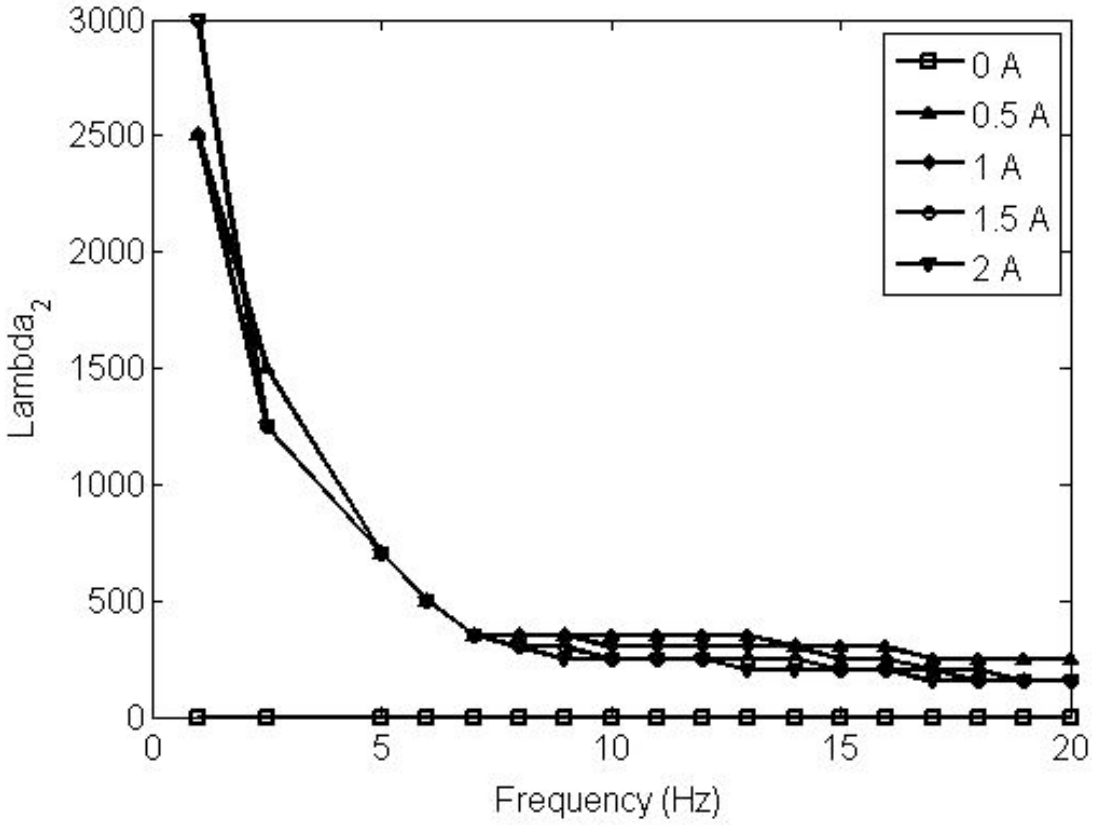

Figure 5.6 λ_2 versus frequency for displacement amplitude of 0.25 mm and varying applied current.

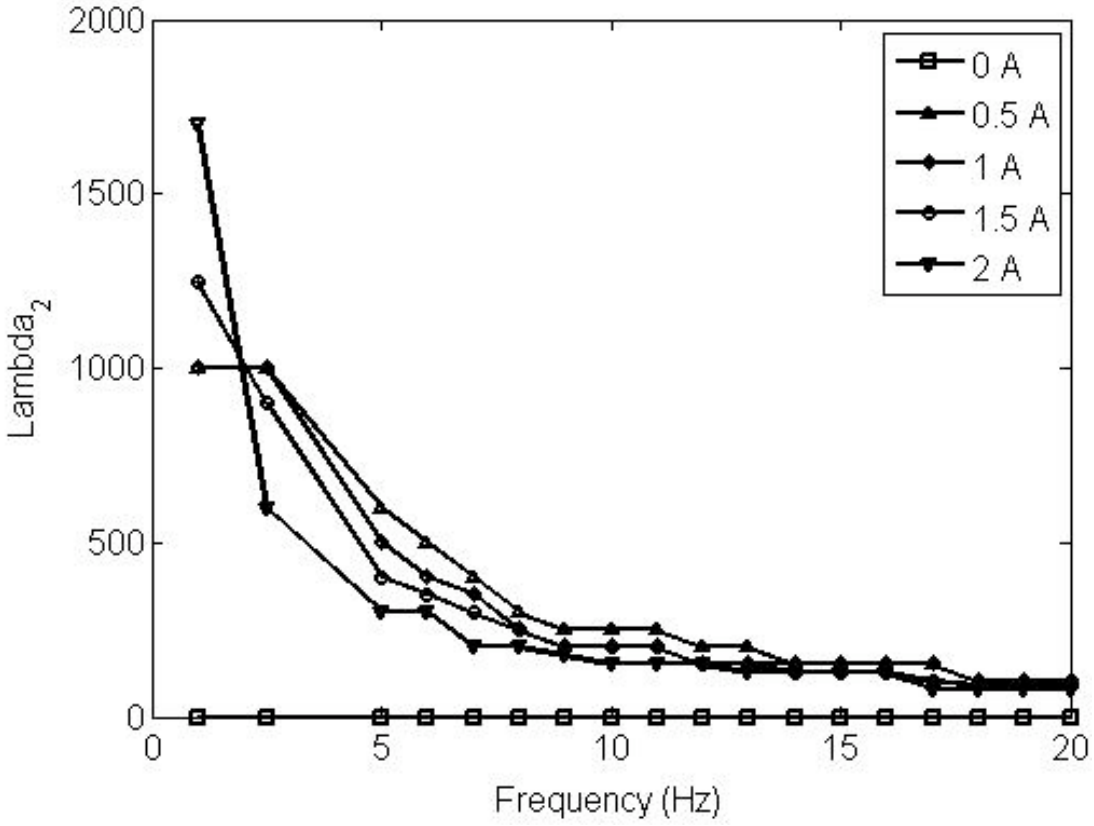

Figure 5.7 λ_2 versus frequency for displacement amplitude of 0.5 mm and varying applied current.

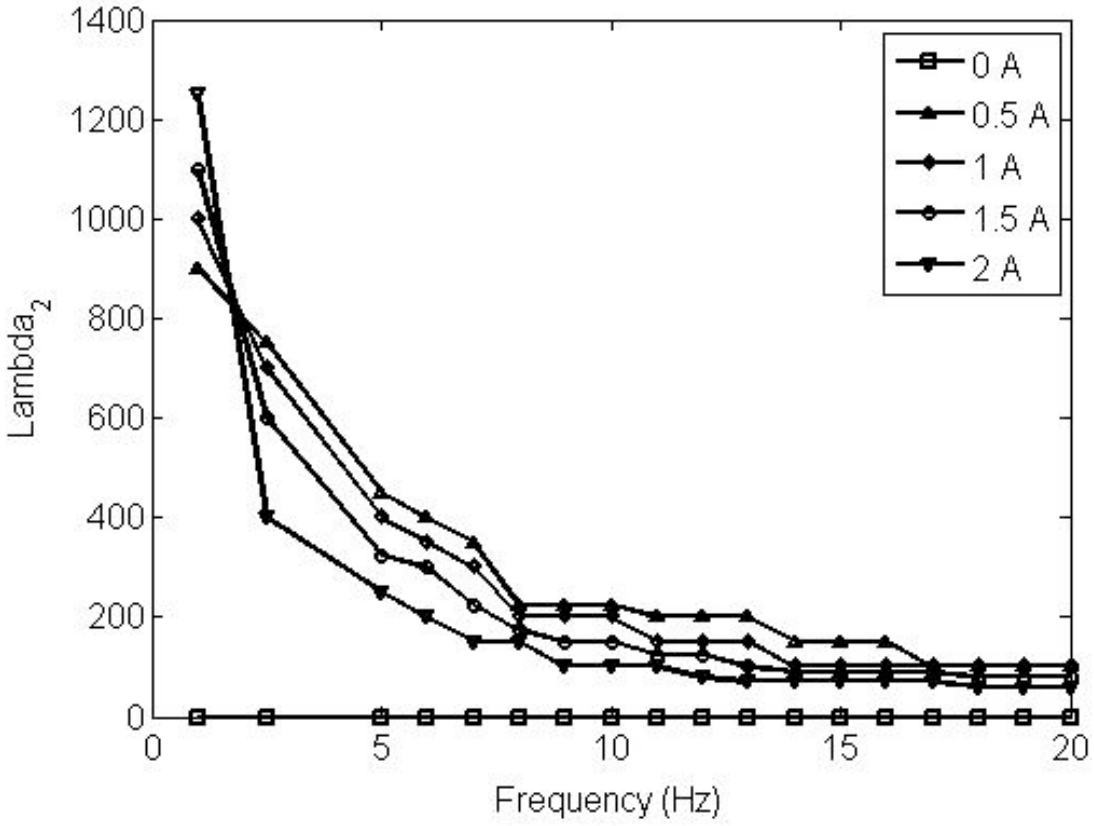

Figure 5.8 λ_2 versus frequency for displacement amplitude of 0.75 mm and varying applied current.

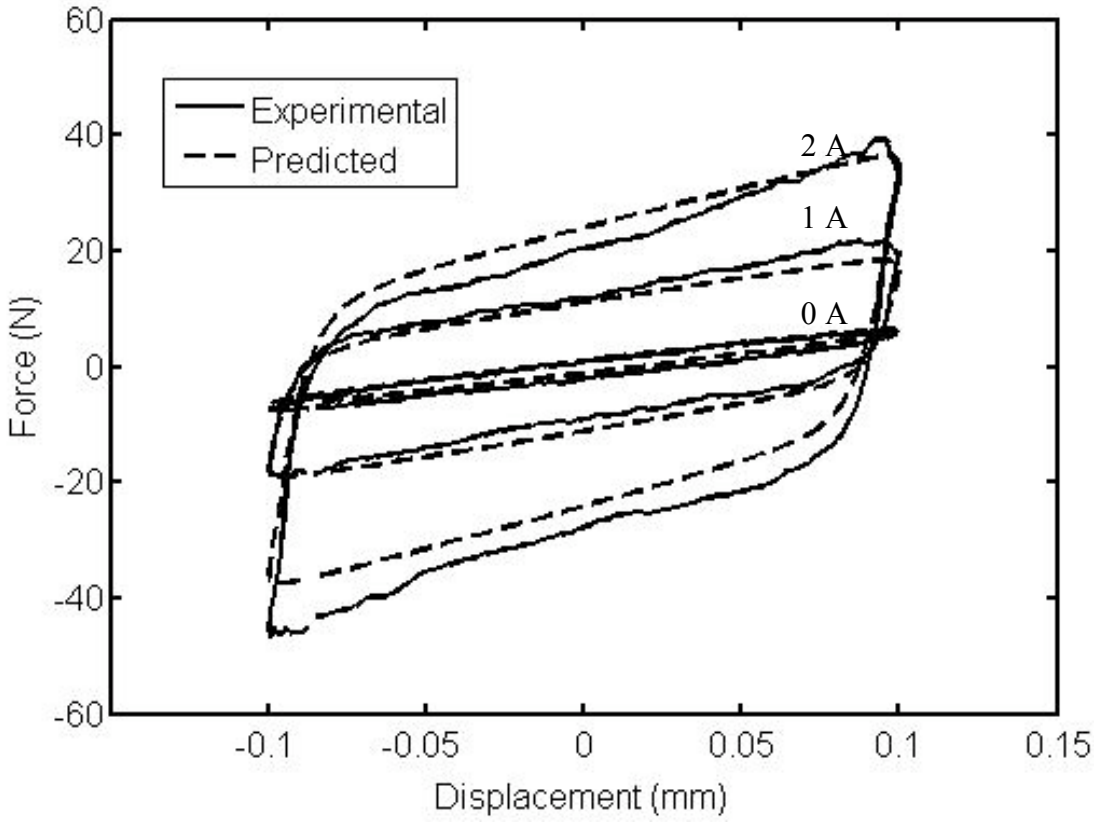

Figure 5.9 Predicted force using nonlinear hysteresis model and experimental force versus displacement for displacement amplitude of 0.1 mm, excitation frequency of 5 Hz and varying applied current.

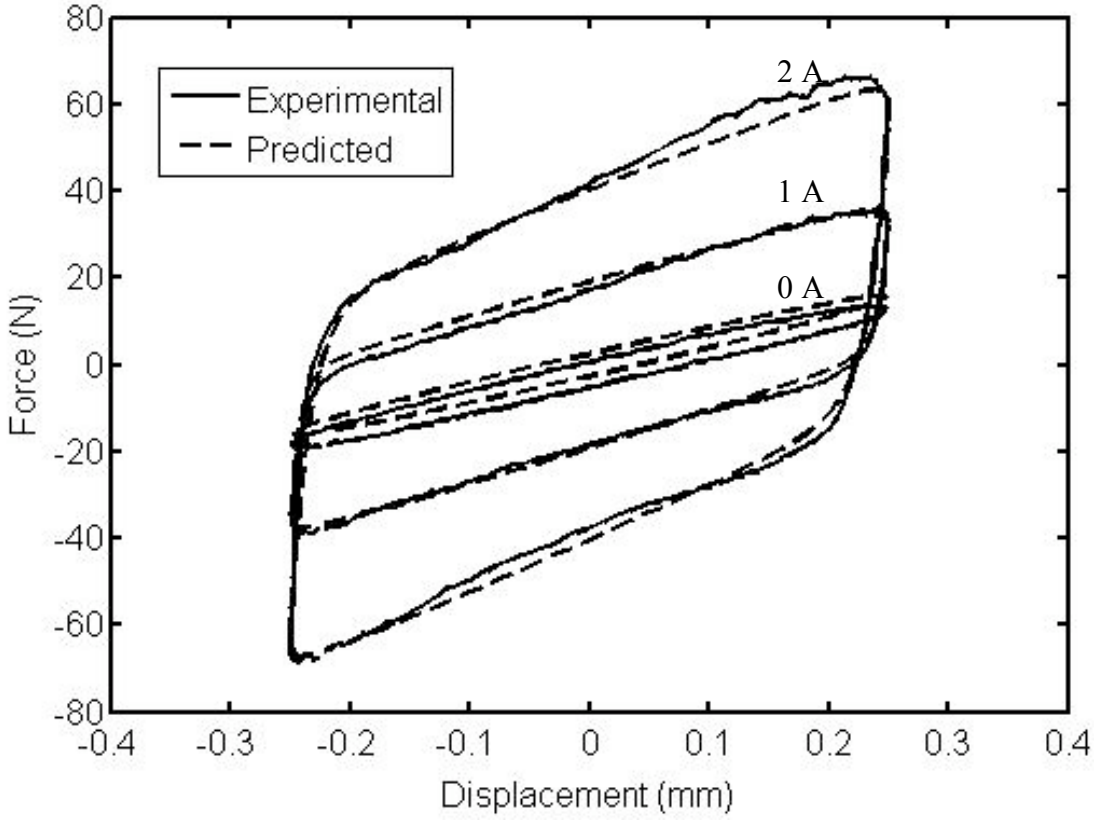

Figure 5.10 Predicted force using nonlinear hysteresis model and experimental force versus displacement for displacement amplitude of 0.25 mm, excitation frequency of 5 Hz and varying applied current.

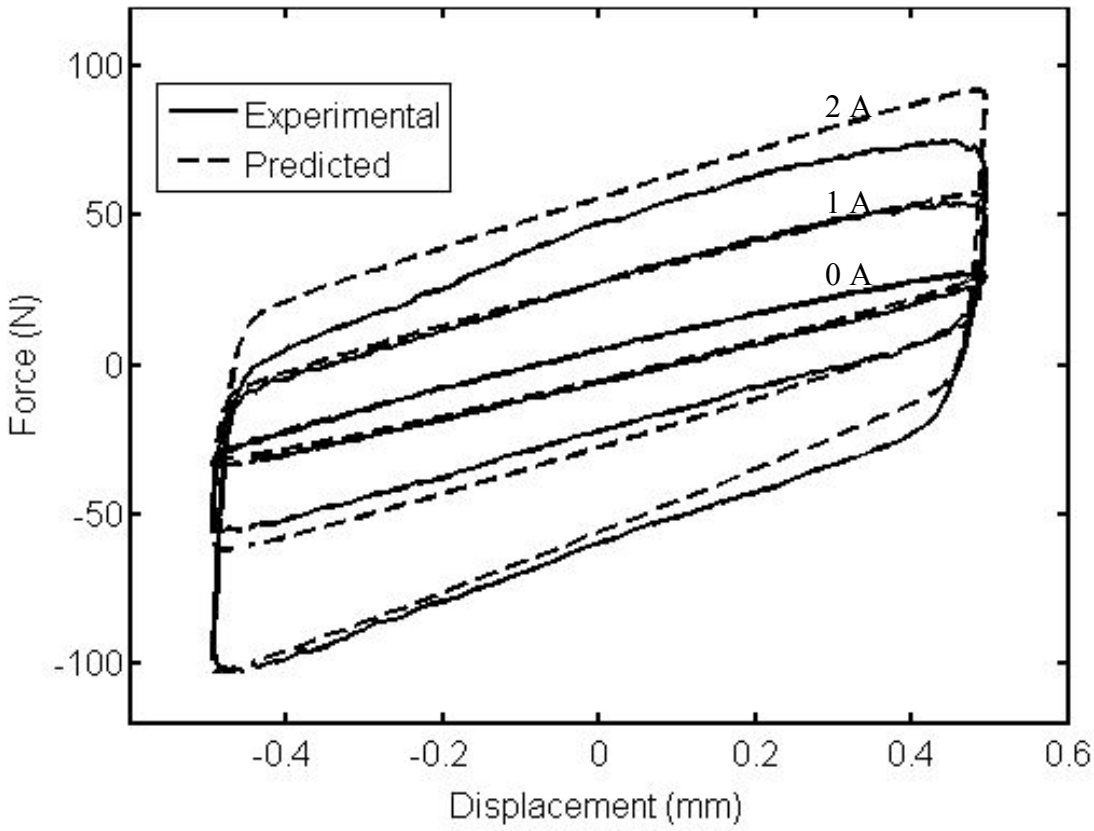

Figure 5.11 Predicted force using nonlinear hysteresis model and experimental force versus displacement for displacement amplitude of 0.5 mm, excitation frequency of 5 Hz and varying applied current.

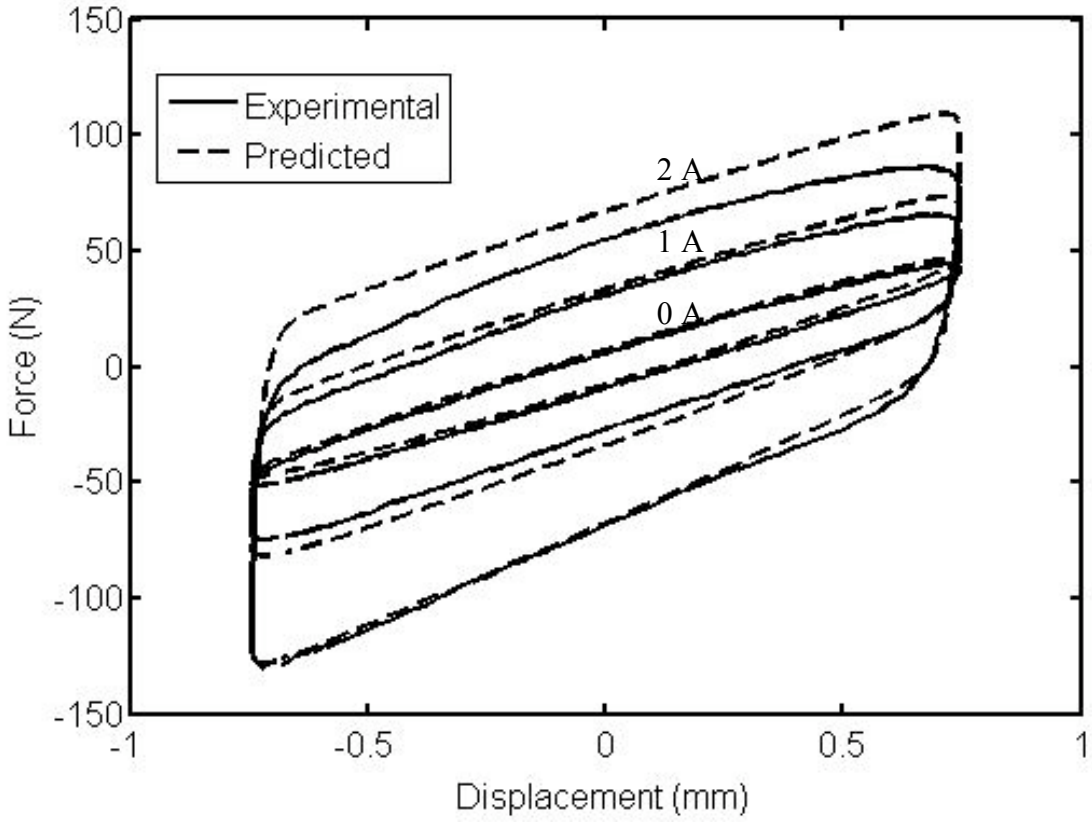

Figure 5.12 Predicted force using nonlinear hysteresis model and experimental force versus displacement for displacement amplitude of 0.75 mm, excitation frequency of 5 Hz and varying applied current.

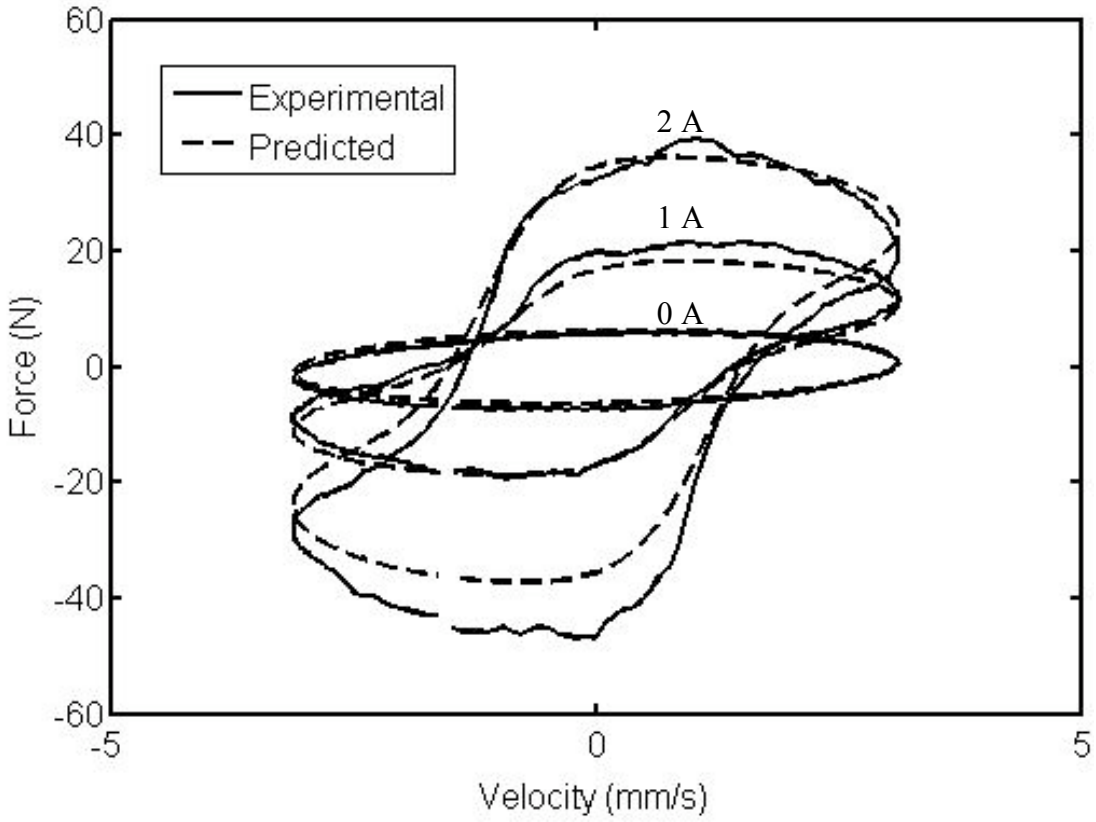

Figure 5.13 Predicted force using nonlinear hysteresis model and experimental force versus velocity for displacement amplitude of 0.1 mm, excitation frequency of 5 Hz and varying applied current.

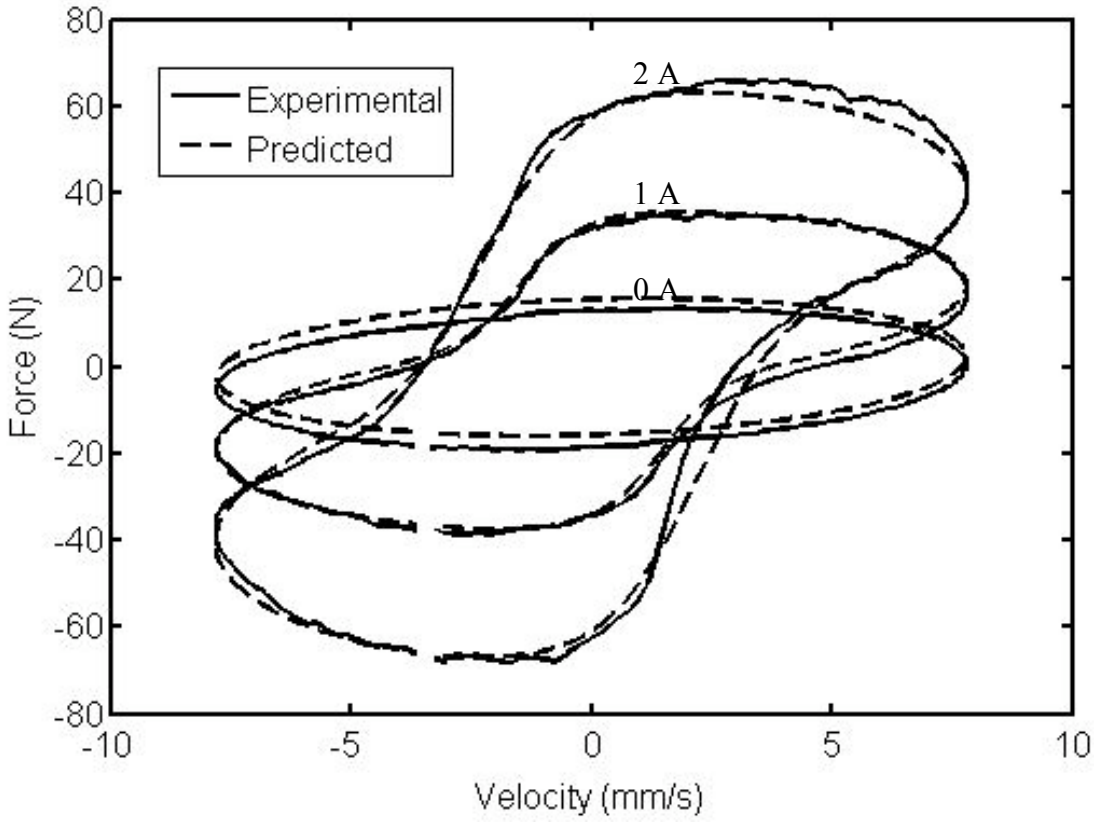

Figure 5.14 Predicted force using nonlinear hysteresis model and experimental force versus velocity for displacement amplitude of 0.25 mm, excitation frequency of 5 Hz and varying applied current.

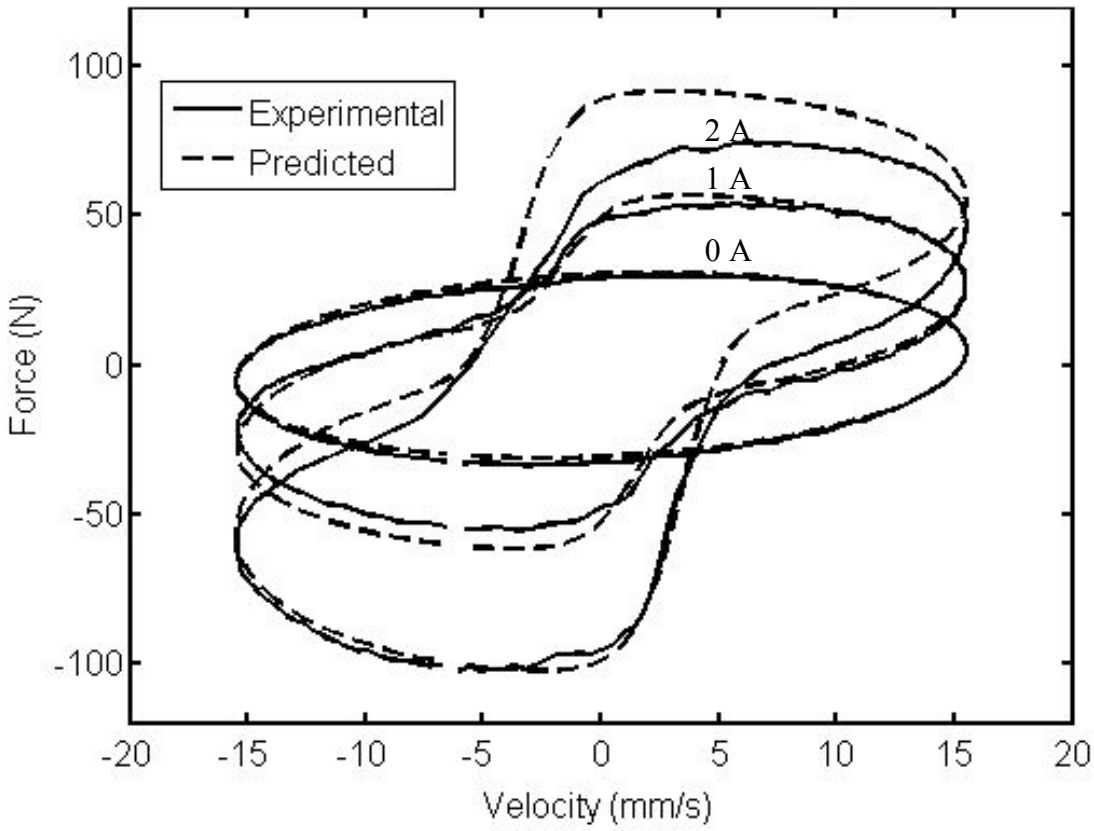

Figure 5.15 Predicted force using nonlinear hysteresis model and experimental force versus velocity for displacement amplitude of 0.5 mm, excitation frequency of 5 Hz and varying applied current.

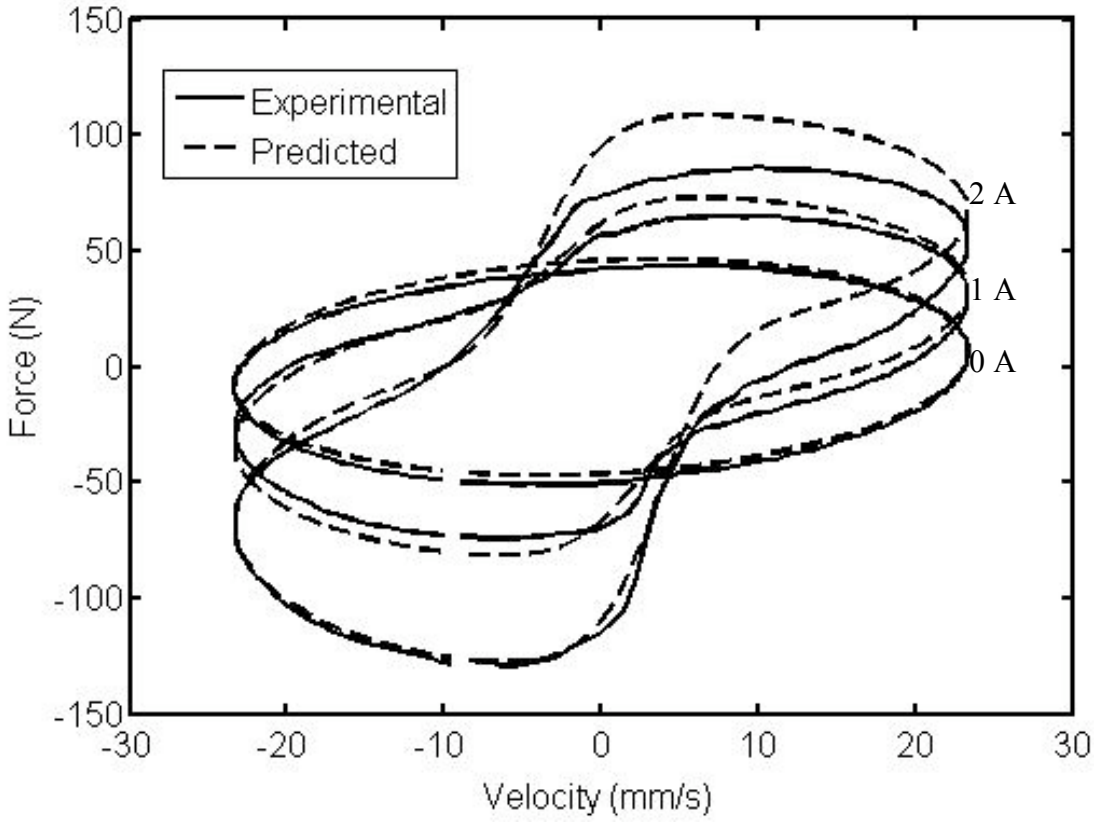

Figure 5.16 Predicted force using nonlinear hysteresis model and experimental force versus velocity for displacement amplitude of 0.75 mm, excitation frequency of 5 Hz and varying applied current.

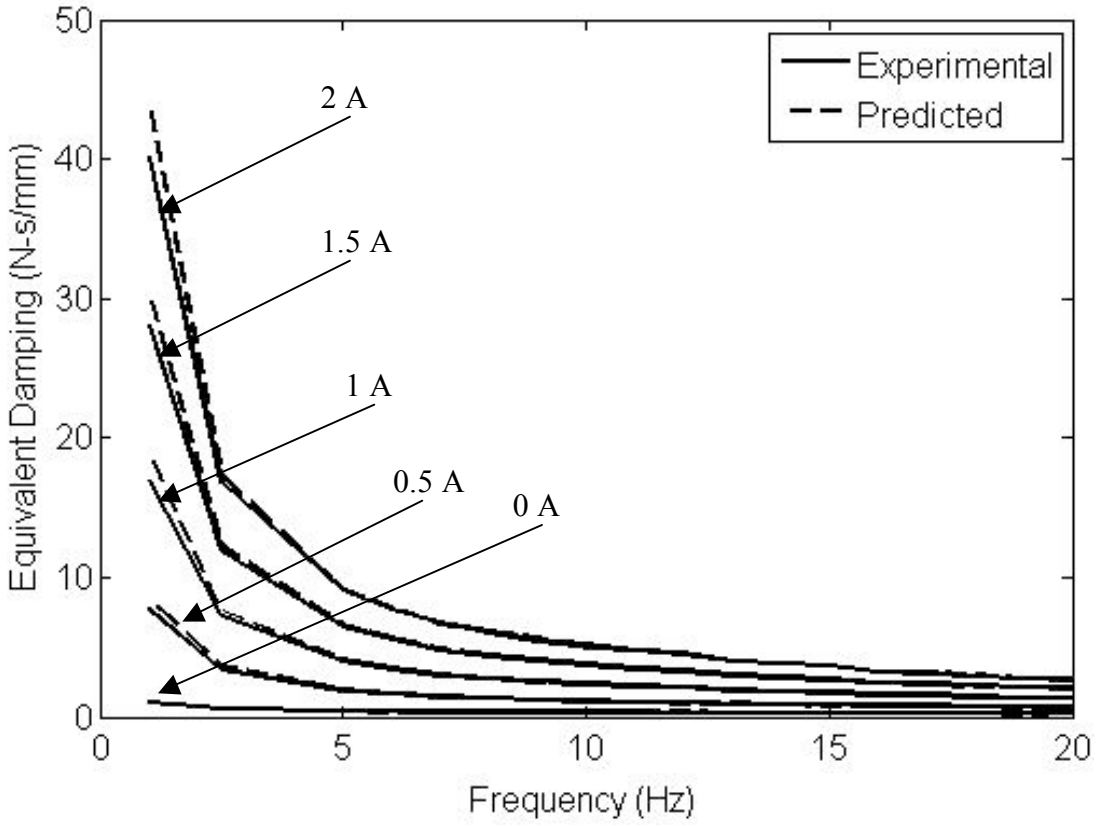

Figure 5.17 Predicted equivalent damping coefficient using nonlinear hysteresis model and experimental equivalent damping coefficient versus frequency for displacement amplitude of 0.1 mm and varying applied current.

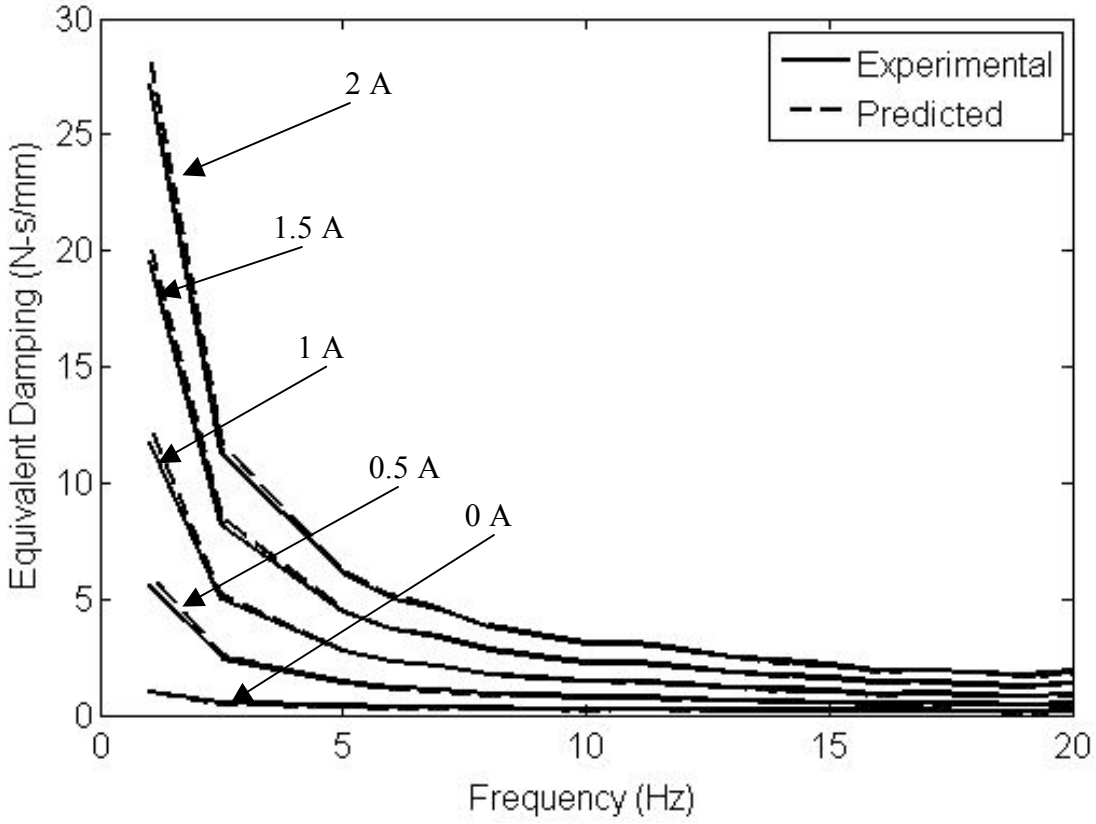

Figure 5.18 Predicted equivalent damping coefficient using nonlinear hysteresis model and experimental equivalent damping coefficient versus frequency for displacement amplitude of 0.25 mm and varying applied current.

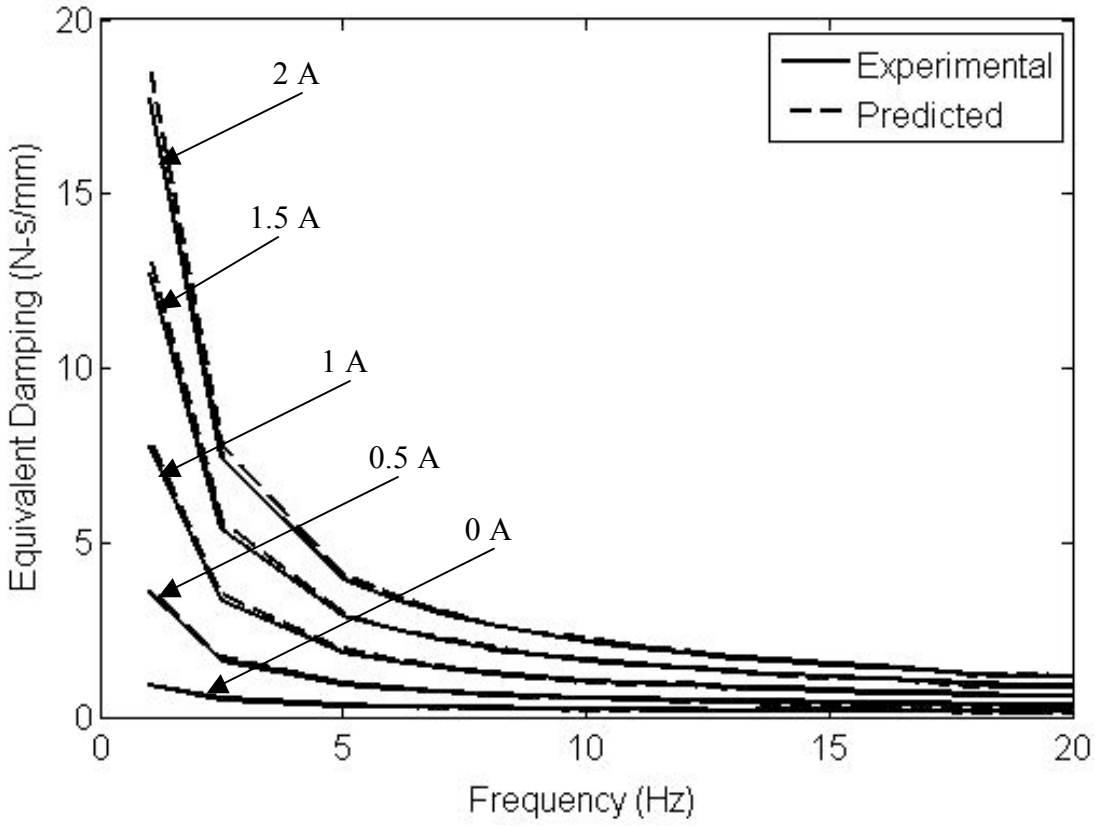

Figure 5.19 Predicted equivalent damping coefficient using nonlinear hysteresis model and experimental equivalent damping coefficient versus frequency for displacement amplitude of 0.5 mm and varying applied current.

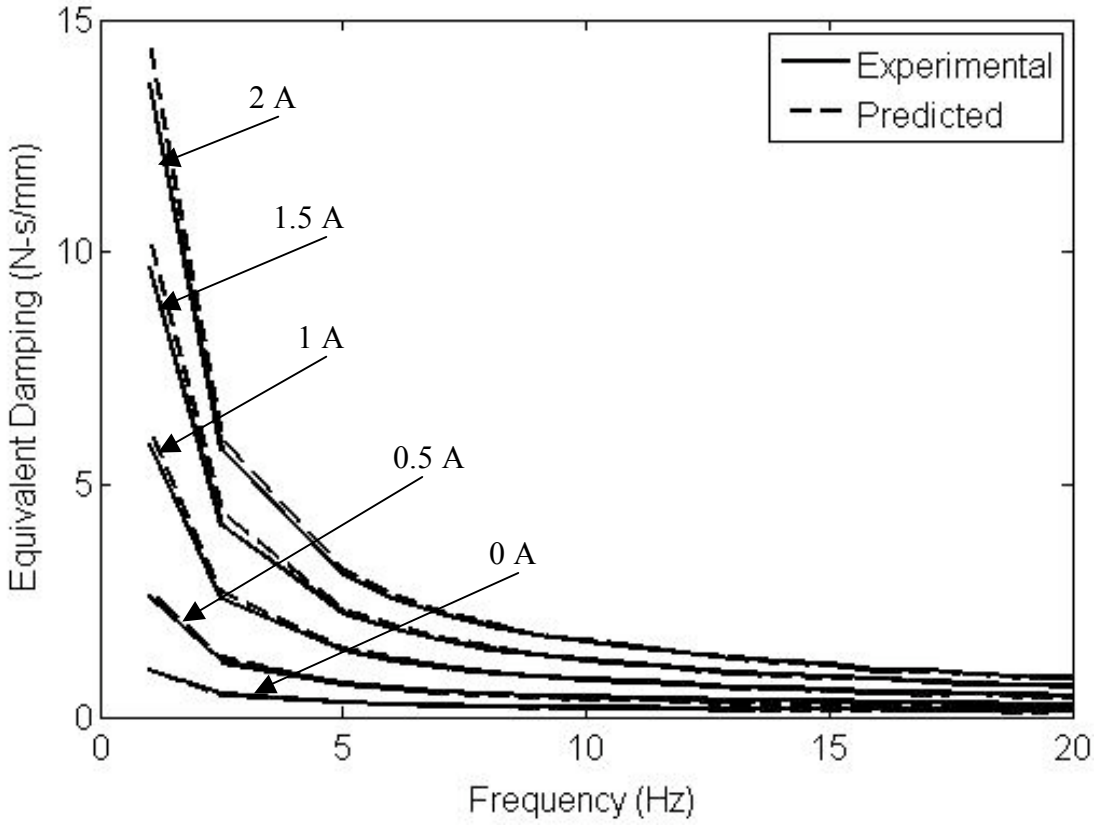

Figure 5.20 Predicted equivalent damping coefficient using nonlinear hysteresis model and experimental equivalent damping coefficient versus frequency for displacement amplitude of 0.75 mm and varying applied current.

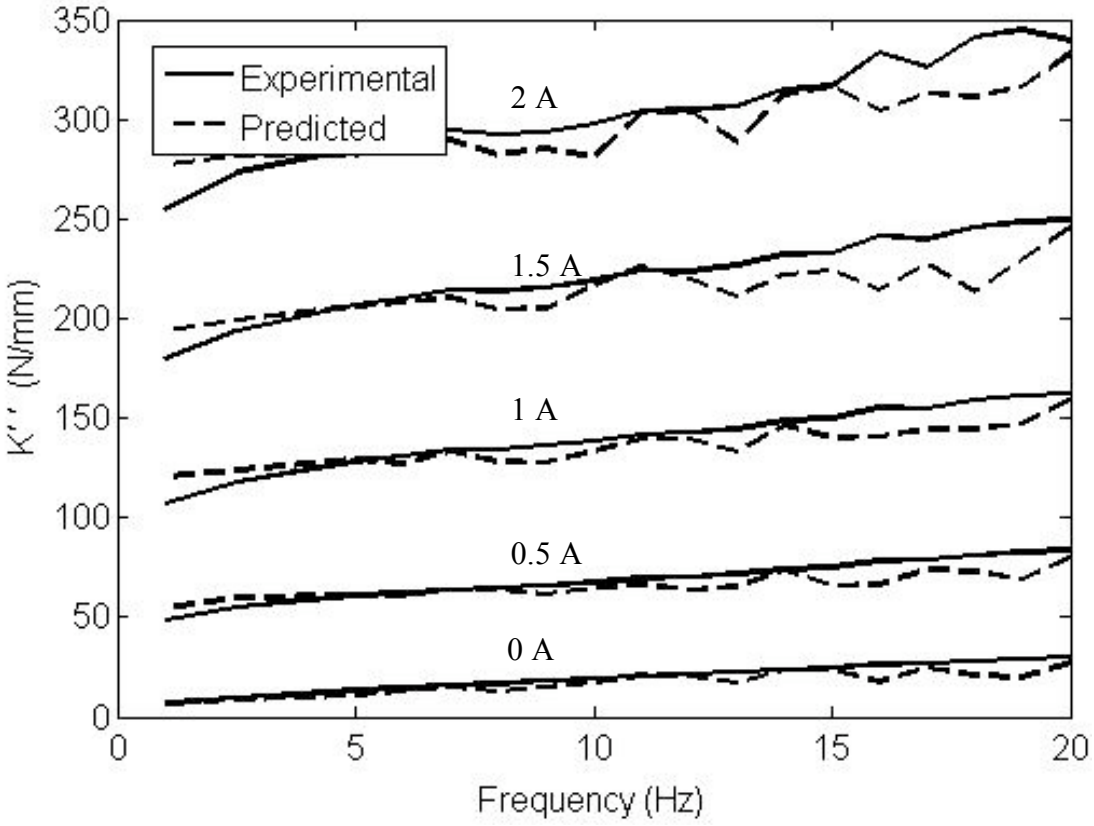

Figure 5.21 Predicted quadrature stiffness using nonlinear hysteresis model and experimental quadrature stiffness versus frequency for displacement amplitude of 0.1 mm and varying applied current.

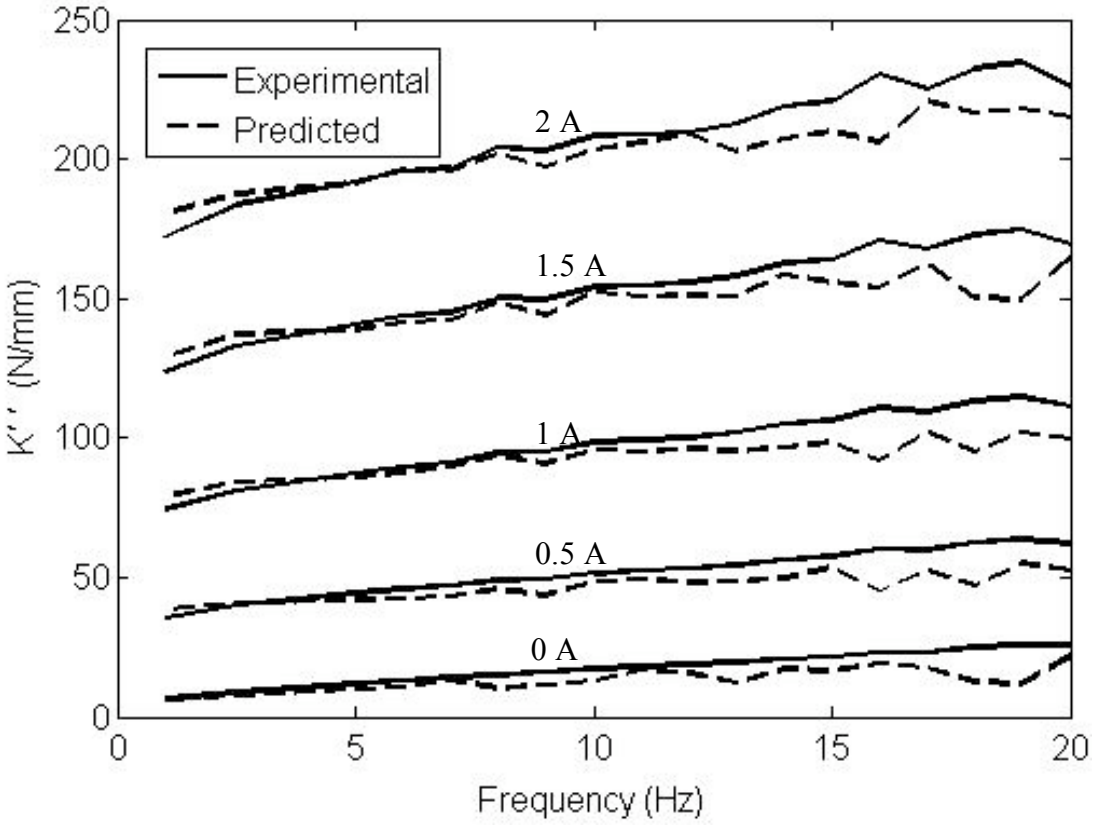

Figure 5.22 Predicted quadrature stiffness using nonlinear hysteresis model and experimental quadrature stiffness versus frequency for displacement amplitude of 0.25 mm and varying applied current.

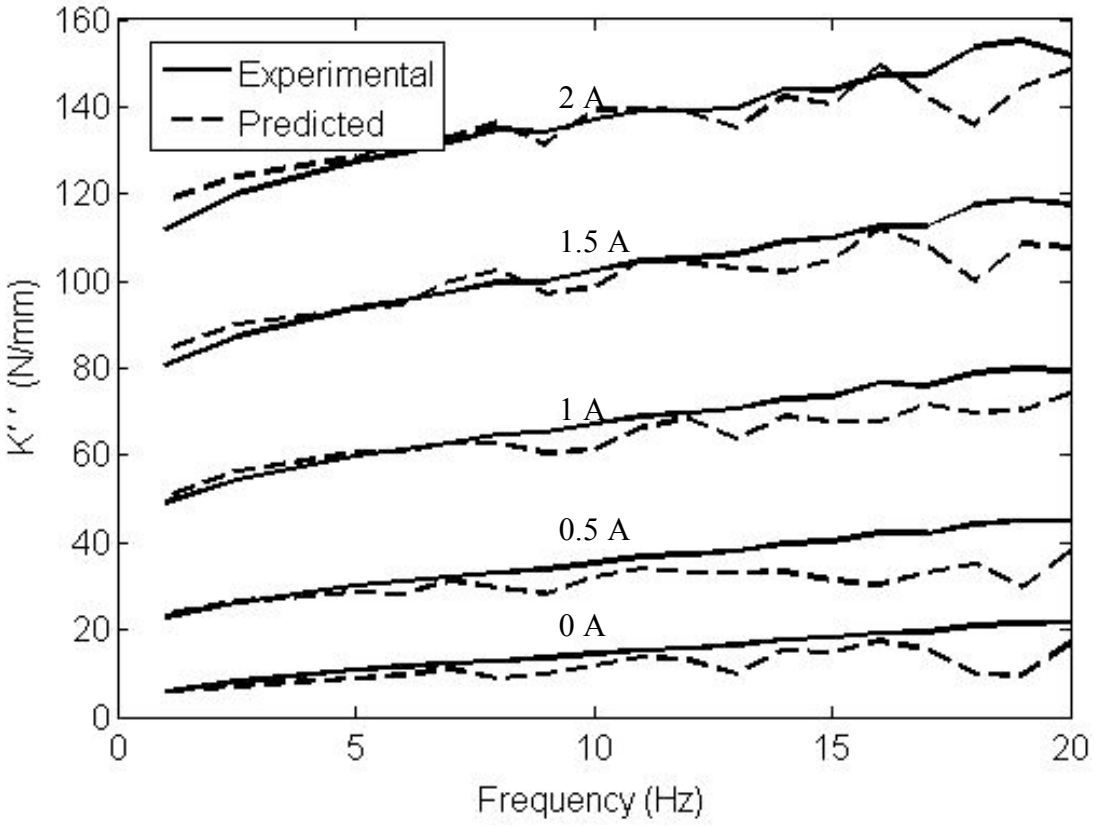

Figure 5.23 Predicted quadrature stiffness using nonlinear hysteresis model and experimental quadrature stiffness versus frequency for displacement amplitude of 0.5 mm and varying applied current.

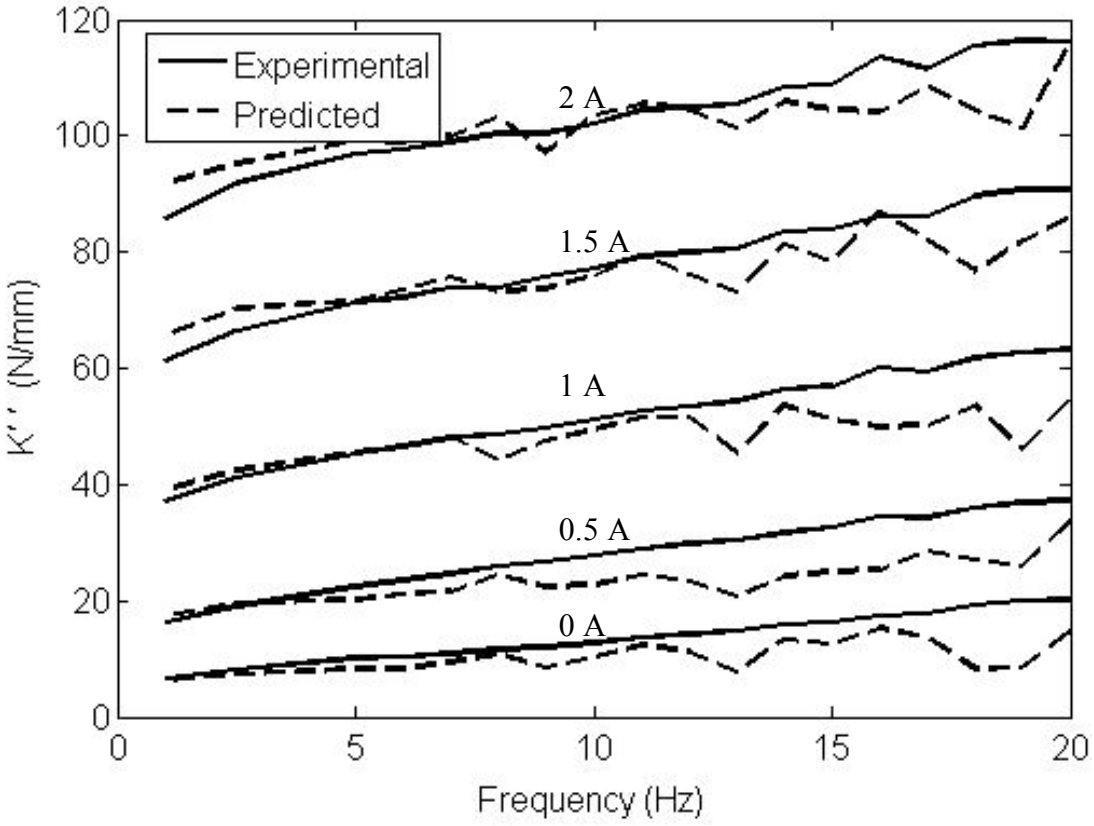

Figure 5.24 Predicted quadrature stiffness using nonlinear hysteresis model and experimental quadrature stiffness versus frequency for displacement amplitude of 0.75 mm and varying applied current.

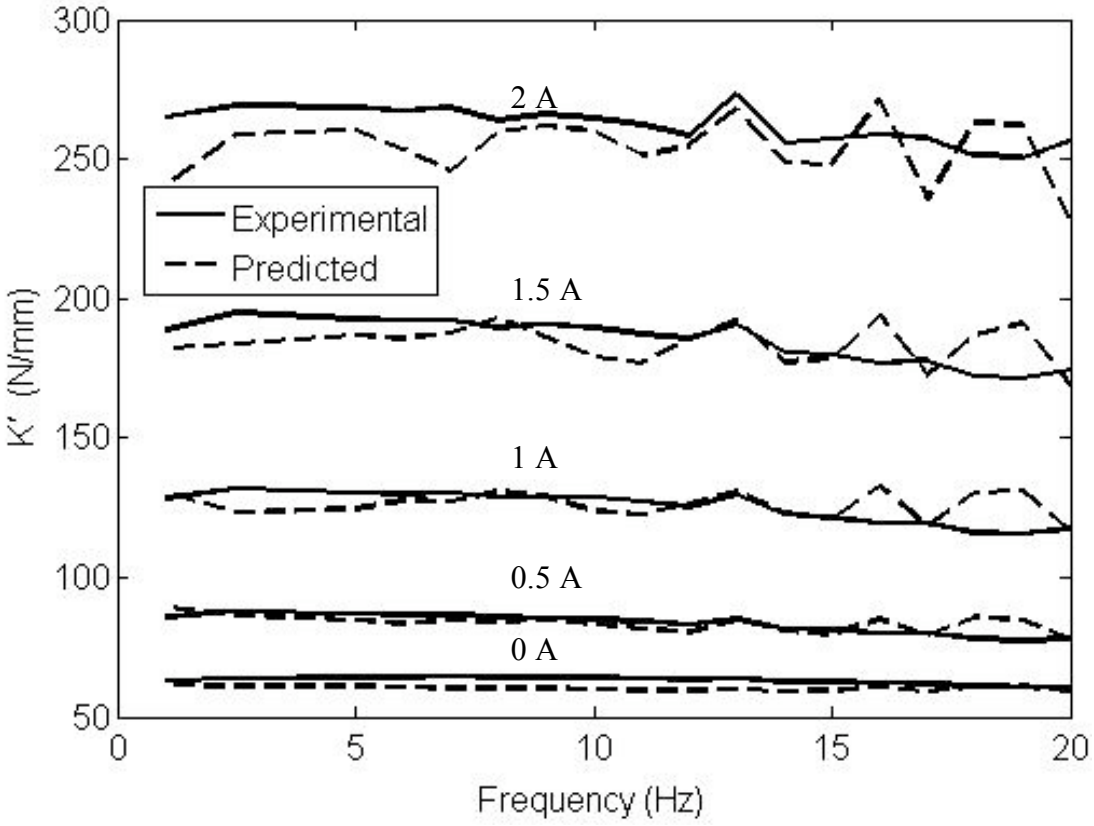

Figure 5.25 Predicted storage stiffness using nonlinear hysteresis model and experimental storage stiffness versus frequency for displacement amplitude of 0.1 mm and varying applied current.

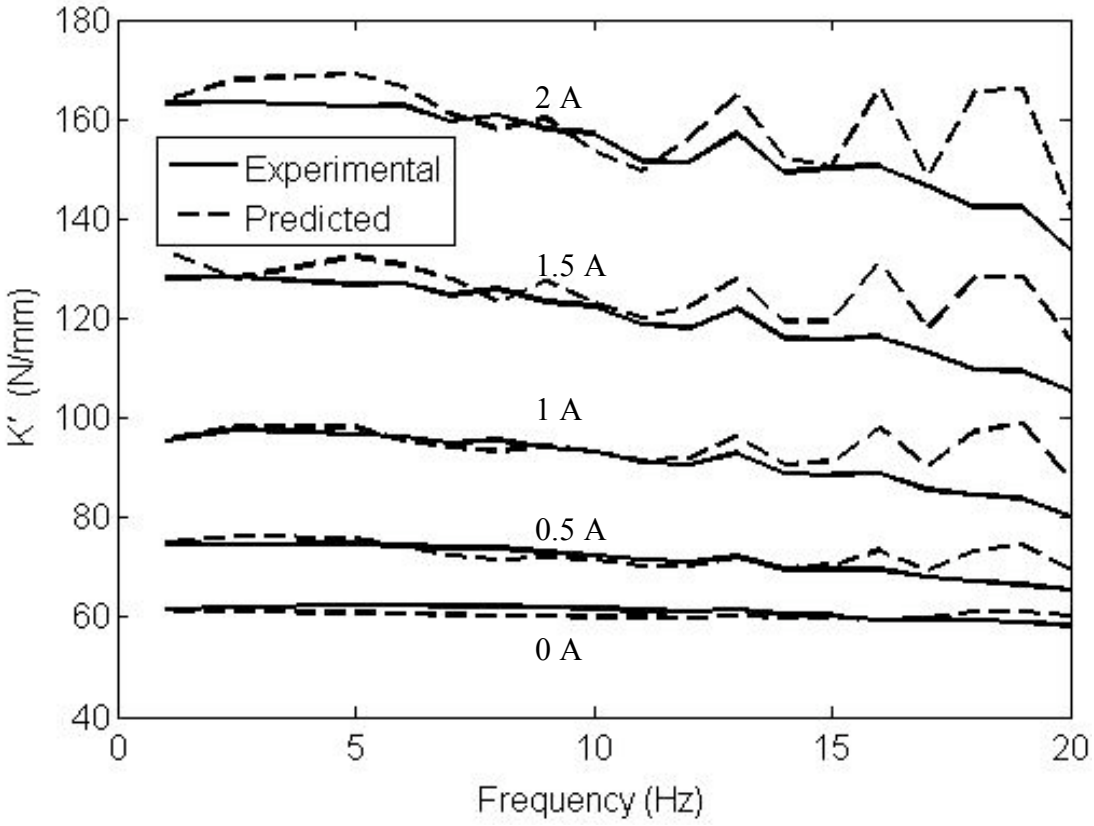

Figure 5.26 Predicted storage stiffness using nonlinear hysteresis model and experimental storage stiffness versus frequency for displacement amplitude of 0.25 mm and varying applied current.

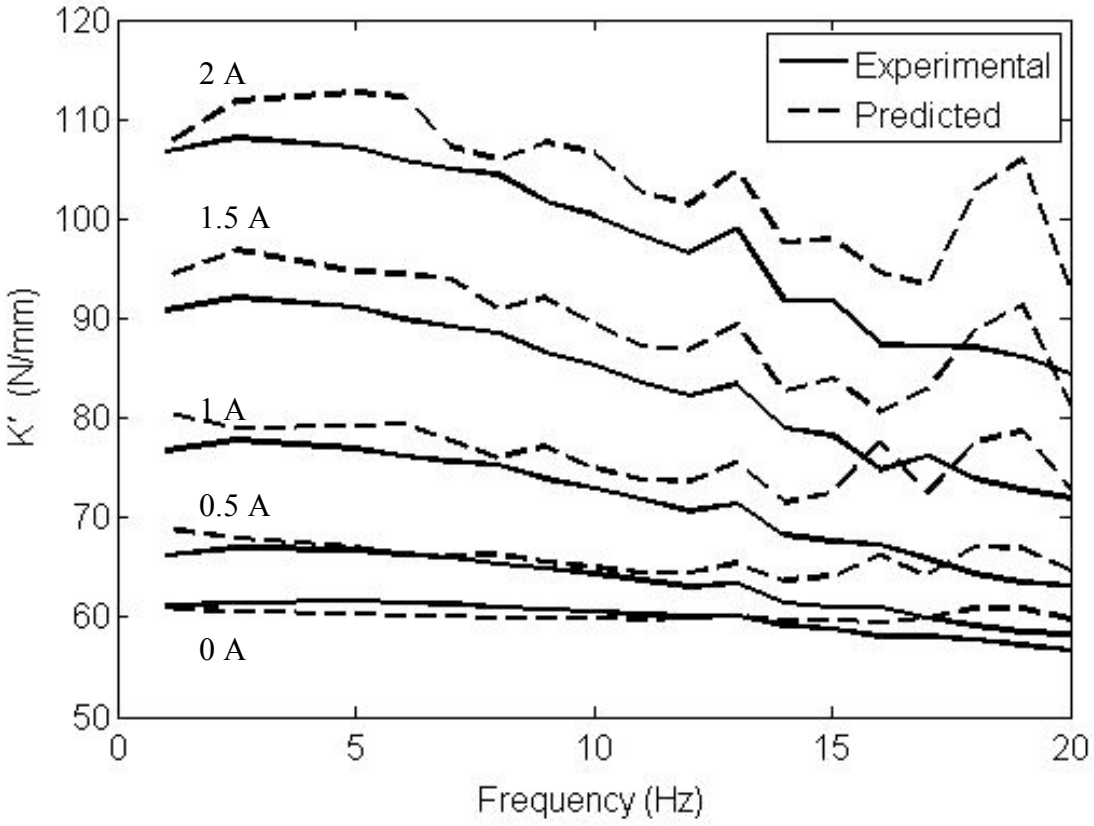

Figure 5.27 Predicted storage stiffness using nonlinear hysteresis model and experimental storage stiffness versus frequency for displacement amplitude of 0.5 mm and varying applied current.

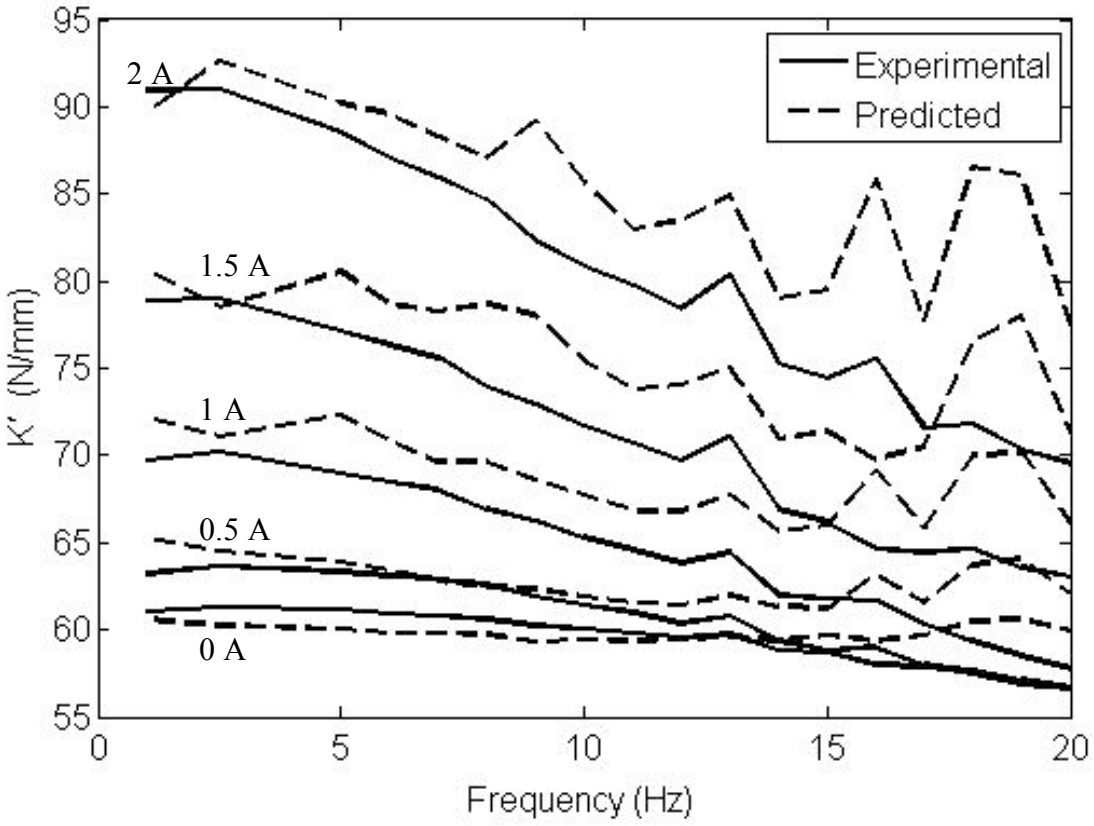

Figure 5.28 Predicted storage stiffness using nonlinear hysteresis model and experimental storage stiffness versus frequency for displacement amplitude of 0.75 mm and varying applied current.

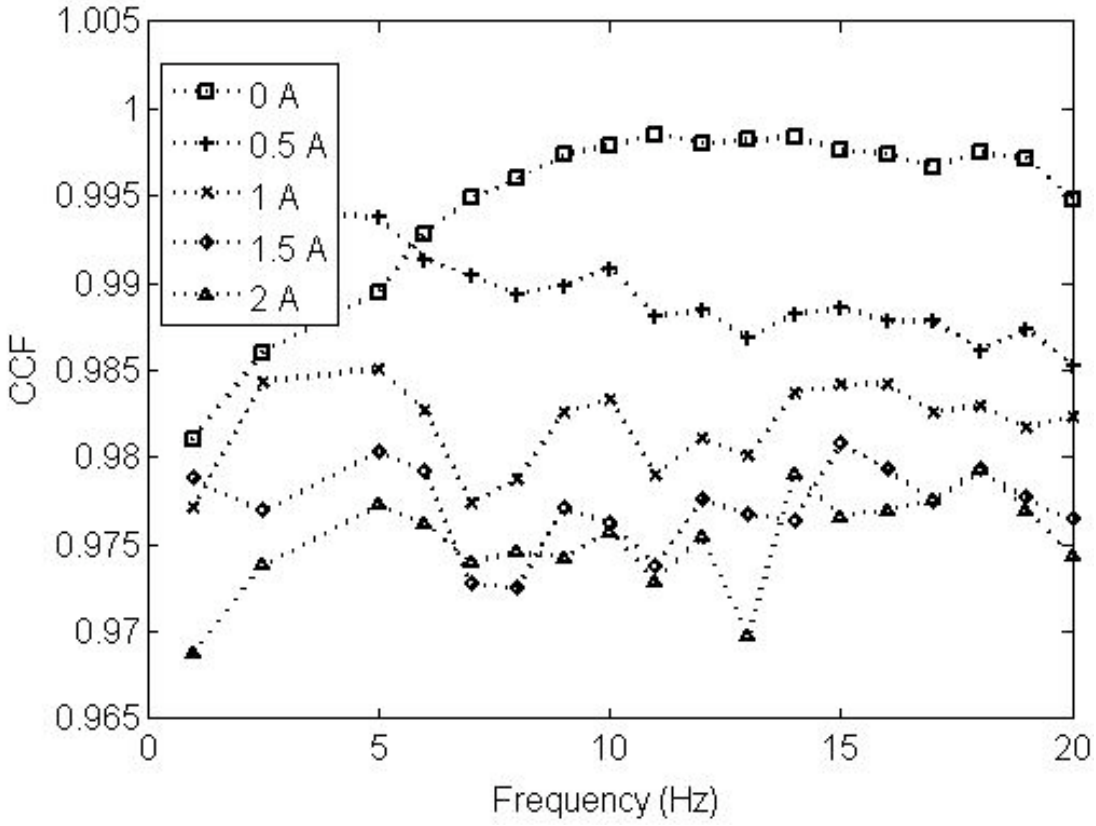

Figure 5.29 CCF versus frequency for displacement amplitude of 0.1 mm. CCF is comparing the force-displacement cycle predicted by the nonlinear hysteresis model to that generated from the experimental data.

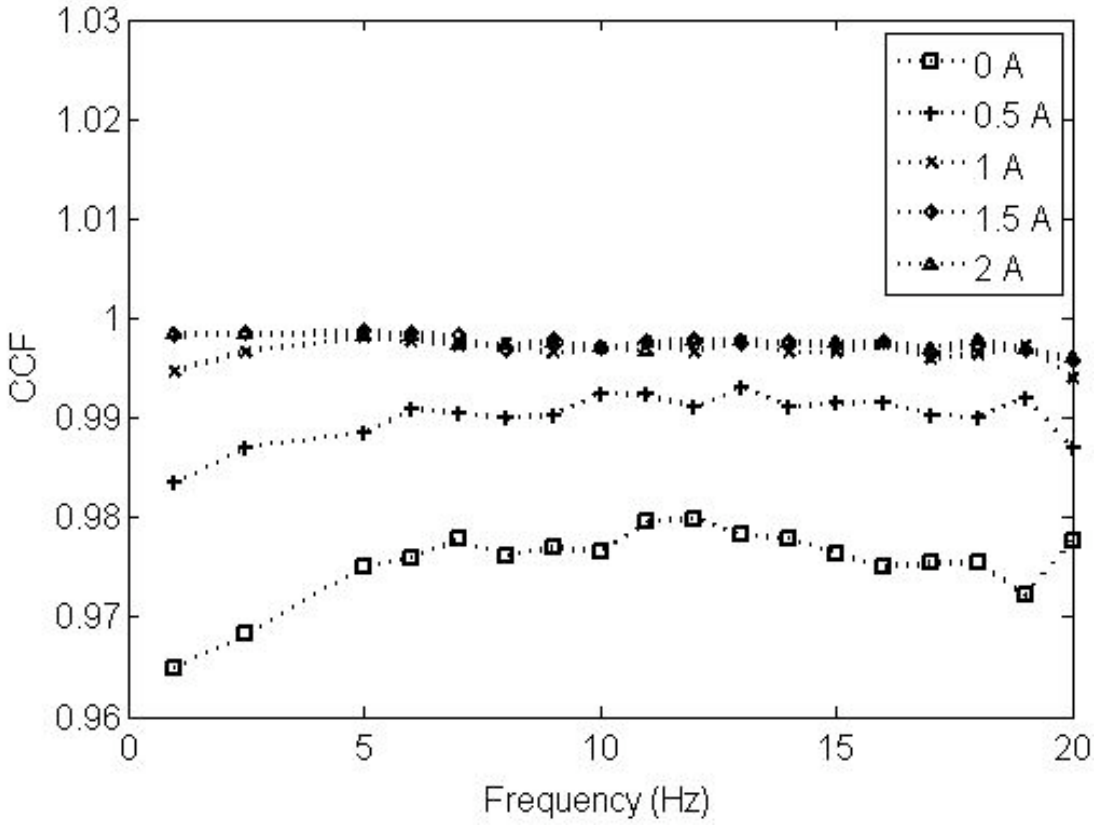

Figure 5.30 CCF versus frequency for displacement amplitude of 0.25 mm. CCF is comparing the force-displacement cycle predicted by the nonlinear hysteresis model to that generated from the experimental data.

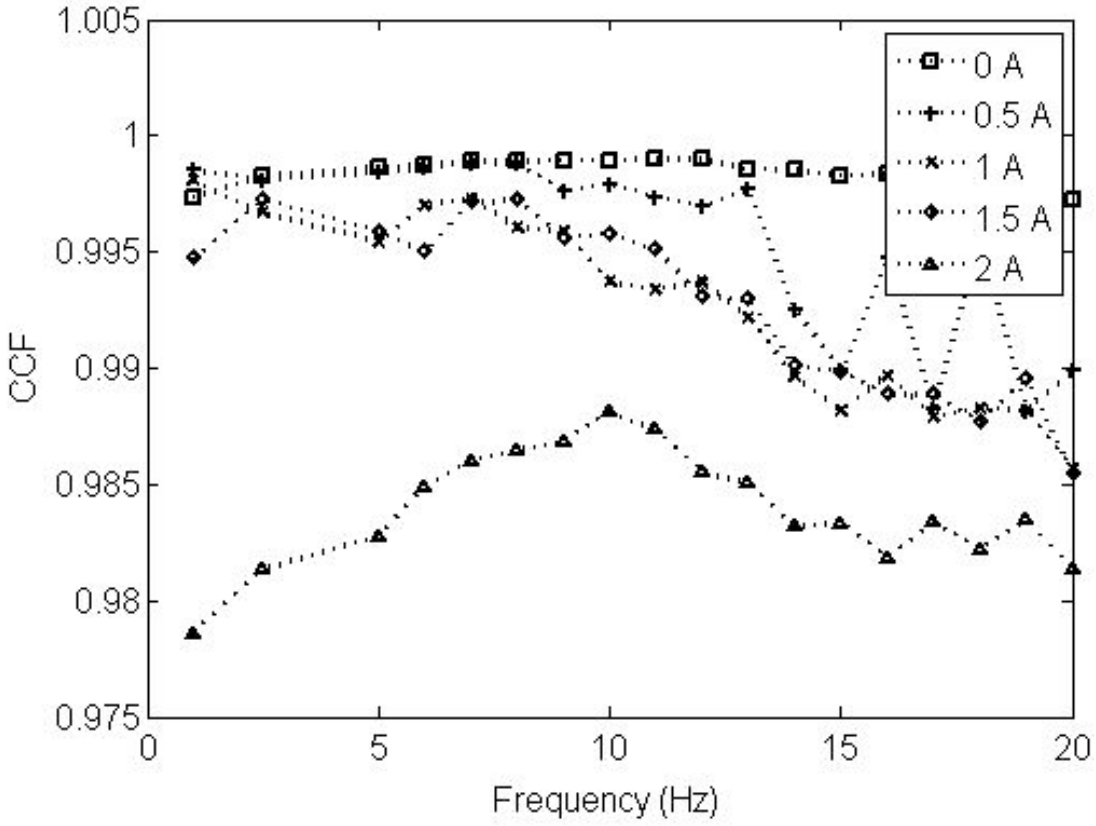

Figure 5.31 CCF versus frequency for displacement amplitude of 0.5 mm. CCF is comparing the force-displacement cycle predicted by the nonlinear hysteresis model to that generated from the experimental data.

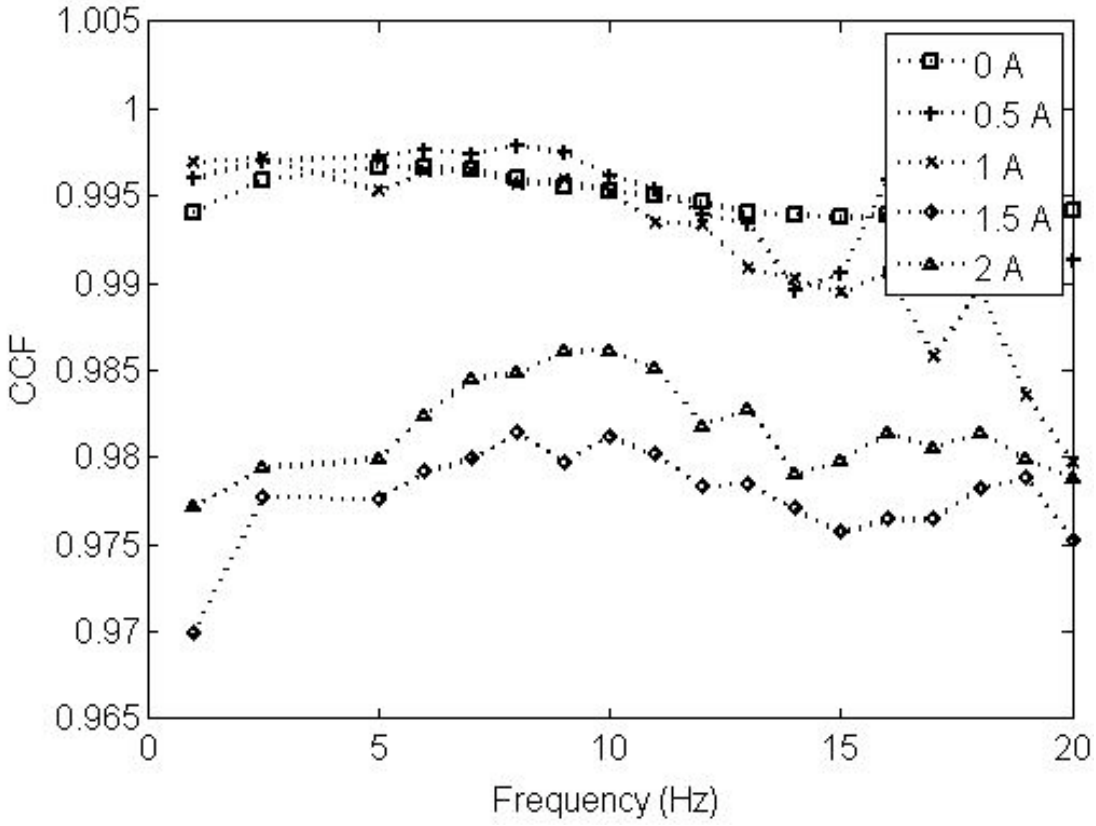

Figure 5.32 CCF versus frequency for displacement amplitude of 0.75 mm. CCF is comparing the force-displacement cycle predicted by the nonlinear hysteresis model to that generated from the experimental data.

Chapter 6: Conclusions

Three MR isolators, of separate designs, have been conceived and constructed at the University of Maryland based upon the shear, squeeze and flow modes in order to reduce vibrations in a sensor platform. Sinusoidal displacement testing using an MTS machine allowed the dynamic range for each design to be calculated. Design 3, a multi-mode isolator, was capable of producing a dynamic range of 3.7. This was a significant improvement over designs 1 and 2, which had dynamic ranges of 1 and 1.2, respectively.

Several design features contributed to the success of design 3. By creating an isolator, which produced damping through motion of a bobbin submerged in MR fluid, the effects of compliant air bubbles within the fluid chamber were mitigated. These effects were problematic in the design 1. Another successful feature is the implementation of the bobbin disc side up into the MR isolator. It was shown via an FEM analysis that the disc side up configuration was capable of producing a magnetic field in the squeeze mode region that was 2.5 times stronger than one produced using a similar bobbin in the disc side down configuration.

Axial testing of design 3 under axial motion was very successful. The equivalent damping method gave insight to the behavior of the isolator at various displacement amplitudes and frequencies. The damping was found to decrease with increasing displacement amplitude as well as increasing frequency. In the low frequency range, a substantial in increase in the energy dissipated by the isolator can be achieved by applying a magnetic field in the MR isolator. At maximum applied

current the damping of the isolator was an order of magnitude higher than in the case when no current was applied. At higher frequencies an application of current led to an increase in damping as well, although it was not as pronounced as in the low frequencies.

Several constitutive models for design 3 were developed for axial displacement of the MR isolator: one was based upon the Bingham plastic model, and the other was a nonlinear hysteresis model. The ability of the models to predict damper behavior was largely dependent upon proper identification of the model parameters. Two methods were used to determine the stiffness and yield stress parameters: (1) using the complex stiffness method the isolator stiffness was identified. (2) By averaging the experimental force over a displacement cycle linearized stiffness was found and through an averaging of the force over a velocity cycle linearized damping force was extracted. From these linearized forces information about the stiffness as well as the yield force of the MR isolator were determined. The complex stiffness method of parameter identification, which is equivalent to using the stiffness from the Kelvin chain model, did not correlate as well with the experimental data as the displacement and velocity averaging technique.

Using the equivalent damping and complex modulus techniques the ability of the models to predict the damping and stiffness of the MR isolator was studied. Both models were able to predict damping behavior. However, the Bingham plastic model, which cannot model the low speed velocity hysteresis of the MR isolator, was unable to match the stiffness of the MR isolator found through experimental means. The nonlinear hysteresis model, which includes the hypertangent function to capture the

hysteresis loop, is able to predict the stiffness of the MR isolator. The zero speed force step discontinuity found in the Bingham model is not able to recreate the hysteresis loop. This hysteresis loop is important, as it affects the stiffness of the MR isolator.

The complex correlation coefficient was used to quantitatively study the ability of the models to predict isolator force. A correlation coefficient of 1 indicates a perfect model fit. For most frequencies, displacement amplitudes and applied currents the Bingham model achieved a correlation coefficient higher than 0.9. The lowest correlation coefficient for this model was 0.85. The CCF for the nonlinear hysteresis model was usually above 0.97, while the lowest CCF was 0.965. This indicates that the nonlinear hysteresis model was able to more accurately predict the shape of the isolator's force-displacement plot, thus it was better able to predict the magnitude and phase of the isolator force.

Future work in this study includes characterization of and modeling of design 3 for lateral motions. Once a complete model of the isolator has been developed, which accommodates axial as well as lateral motion, a control strategy can be implemented to further reduce vibrations within the sensor platform.

Bibliography

[1] L. Zipser, L. Richter, U. Lange, "Magnetorheological fluids for actuators," *Sensors and Actuators A,* Vol. 92, pp. 318-325, 2001

[2] M.R. Jolly, J.D. Carlson, B.C. Munoz, "A model of the behaviour of magnetorheological materials," *Smart Materials and Structures,* Vol. 5, pp. 607-614, 1996

[3] Kamath, G.M., Wereley, N.M., Jolly, M.R., "Characterization of magnetorheological helicopter lag dampers," *Journal of the American Helicopter Society,* Vol. 44, pp.234-248, 1999

[4] Hiemenz, G.J., Choi, Y.T., Wereley, N.M., "Seismic control of civil structures utilizing semi-active MR braces," *Computer-Aided Civil and Infrastructure Engineering,* Vol. 18, pp. 30-43, 2003

[5] Choi, Y.T., Wereley, N.M., " Vibration control of a landing gear system featuring electrorheological/magnetorheological fluids," *Journal of Aircraft*, Vol.40, pp. 432-439, 2003

[6] Kamath, G.M., Hurt, M.K., Wereley, N.M., "Analysis and testing of Bingham plastic behavior in semi-active electrorheological fluid dampers," *Smart Materials and Structures*, Vol. 5, pp. 576-590, 1996

[7] Phillips, R.W., "Engineering applications of fluids with a variable yield stress," *PhD Thesis University of California, Berkeley*

[8] Atkin, R.J., Shi, X., Bullough, W.A., "Solutions of the constitutive equations for the flow of an electorheological fluid in radial configurations," *Journal of Rheology,* Vol. 35, pp. 1441-1461, 1991

[9] Kamath, G.M., Wereley, N.M., "A nonlinear viscoelastic-plastic model for electrorheological fluids," *Smart Materials and Structures,* Vol. 6, pp. 351-359, 1997

[10] Lee-Glauser, G.J., Ahmadi, G., Layton, J.B., "Satellite active and passive vibration control during liftoff," *Journal of Spacecraft and Rockets*, Vol. 33, pp. 428-432, 1996

[11] Cobb, R.G., Sullivan, J.M., Das, A., Davis, L.P., Hyde, T.T., Davis, T., Rahman, Z.H., Spanos, J.T., "Vibration isolation and suppression system for precision payloads in space," *Smart Materials and Structures,* Vol. 8, pp. 798-812, 1999

[12] Sable, W.W., Metzger, W.W., Bicos, A.S., Dotson, R.D., "Future science payloads face technology challenges," *Aerospace America,* Feb. 1994, pp. 30-34

[13] White, F.M., "Fluid Mechanics," McGraw-Hill, Inc., 1986

[14] Jolly, M.R., Carlson, J.D., "Controllable squeeze damping using magnetorheological fluid," *5th International Conference on New Actuators*, pp. 333-336, 1996

[15] Wereley, N.M., Pang, L., "Nondimensional analysis of semi-active electrorheological and magnetorheological dampers using approximate parallel plate models," *Smart Materials and Structures*, Vol.7, No.5, pp. 732-743, 1998

[16] Lindler, J., Wereley, N.M., "Analysis and testing of electorheological bypass dampers," *Journal of Intelligent Material Systems and Structures,* Vol. 10, pp. 363-376, 1999

[17] Meirovitch, L., "Elements of vibration analysis," McGraw-Hill, Inc., 1986

[18] Wereley, N.M., Snyder, R., Krishnan, R., Sieg, T., "Helicopter Damping," *Encyclopedia of Vibration,* Academic Press, London, UK, 1999

[19] Hu, W., Wereley, N.M., "Characterization and modeling of nonlinear elastomeric dampers under sinusoidal loading," *Presented at the 44th AIAA/ASME/ASCE/AHS Structures, Structural Dynamics, and Material Conference*, Norfolk, VA, 2003

[20] Choi, S.B., Choi, Y.T., "Sliding mode control of shear-mode type ER engine mount," *KSME International Journal*, Vol. 13, No.1, pp. 26-33, 1999

[21] Nakhaiejazar, G. and Golnaraghi, M.F., "Nonlinear Modeling, Experimental Verification, and Theoretical Analysis of a Hydraulic Engine Mount," Journal of Vibration and Control, Vol. 8, pp. 87-116, 2002

[22] Choi, Y.T., Wereley, N.M., "Semi-active vibration using Magnetorheological isolators," Journal of Aircraft, Vol. 41, No. 3, 2004

Appendix A: Detail Drawings

MR Isolator Design 1

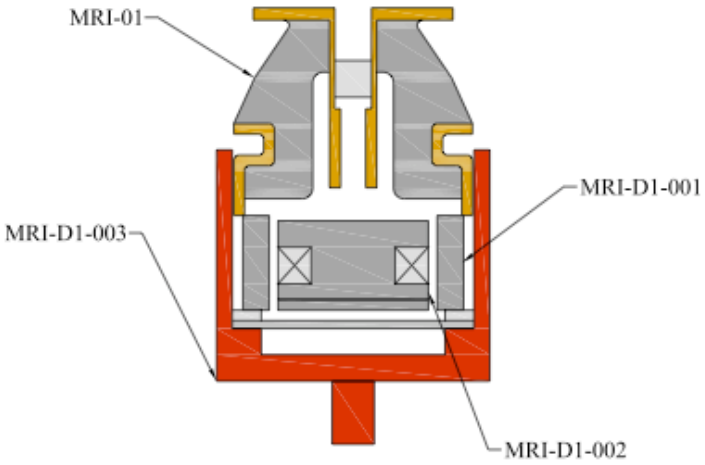

MR Isolator Design 2

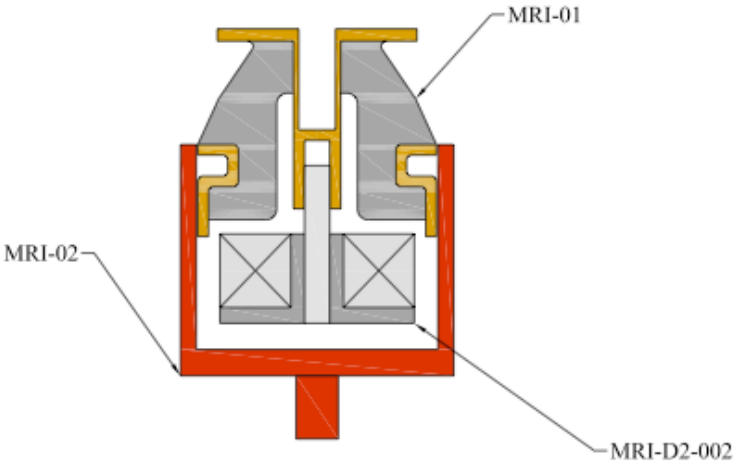

MR Isolator Design 3

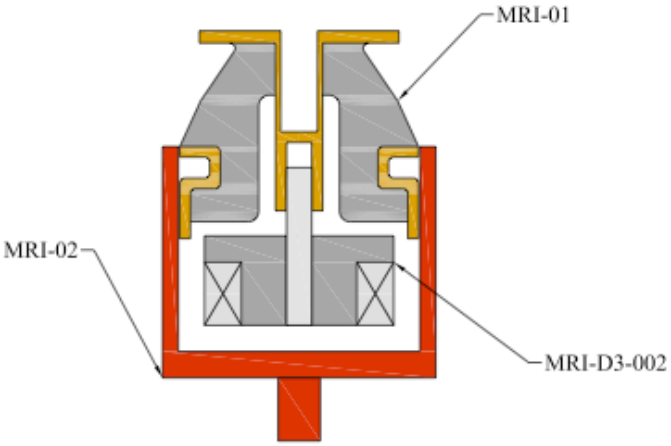

Name: MRI-D1-001 (Design 1 Modified Hydromount)
Material:
Qty: 1
Units: mm unless otherwise noted

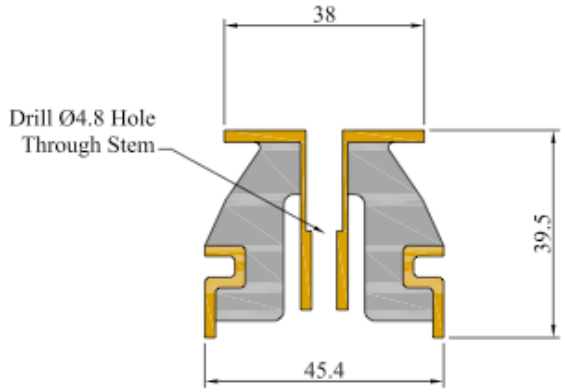

NOTE:
Modifications to Top Part of Hydro-isolator:

A. Cut through shell, 15.5mm
from bottom of flange.

B. 4 holes, 8-32 threaded
thru, separated by 90° should be drilled
10.5mm from bottom of flange to connect
with Outer Cup.

C. Mill flange to be flush with exposed elastomer

D. Drill a Ø4.8 hole through hydromount stem

NOTE: Drawings Not to Scale

Name: MRI-01 (Designs 2 and 3 Modified Hydromount)
Material:
Qty: 5
Units: mm unless otherwise noted

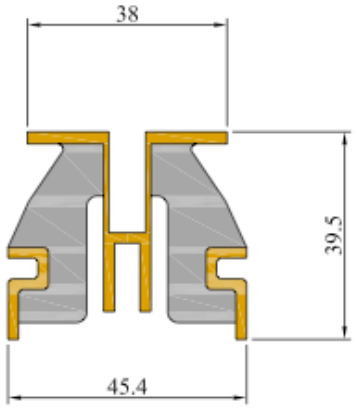

NOTE:
Modifications to Top Part of Hydro-isolator:

A. Cut through shell, 15.5mm
from bottom of flange.

B. 4 holes, 8-32 threaded
thru, separated by 90° should be drilled
10.5mm from bottom of flange to connect
with Outer Cup.

C. Mill flange to be flush with exposed elastomer

NOTE: Drawings Not to Scale

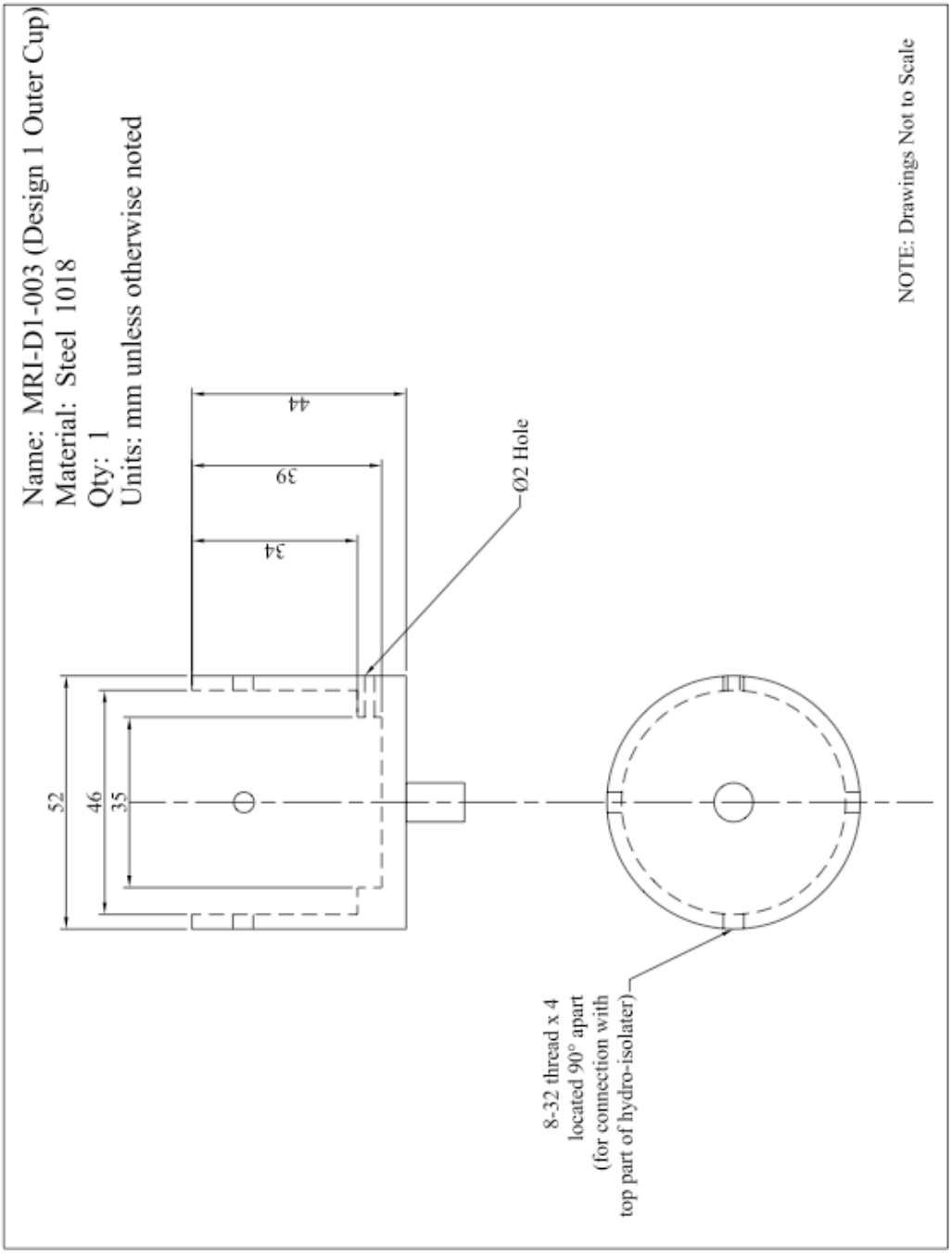
Name: MRI-D1-003 (Design 1 Outer Cup)
Material: Steel 1018
Qty: 1
Units: mm unless otherwise noted
44
39
34
Ø2 Hole
52
46
35
8-32 thread x 4
located 90° apart
(for connection with
top part of hydro-isolater)
NOTE: Drawings Not to Scale

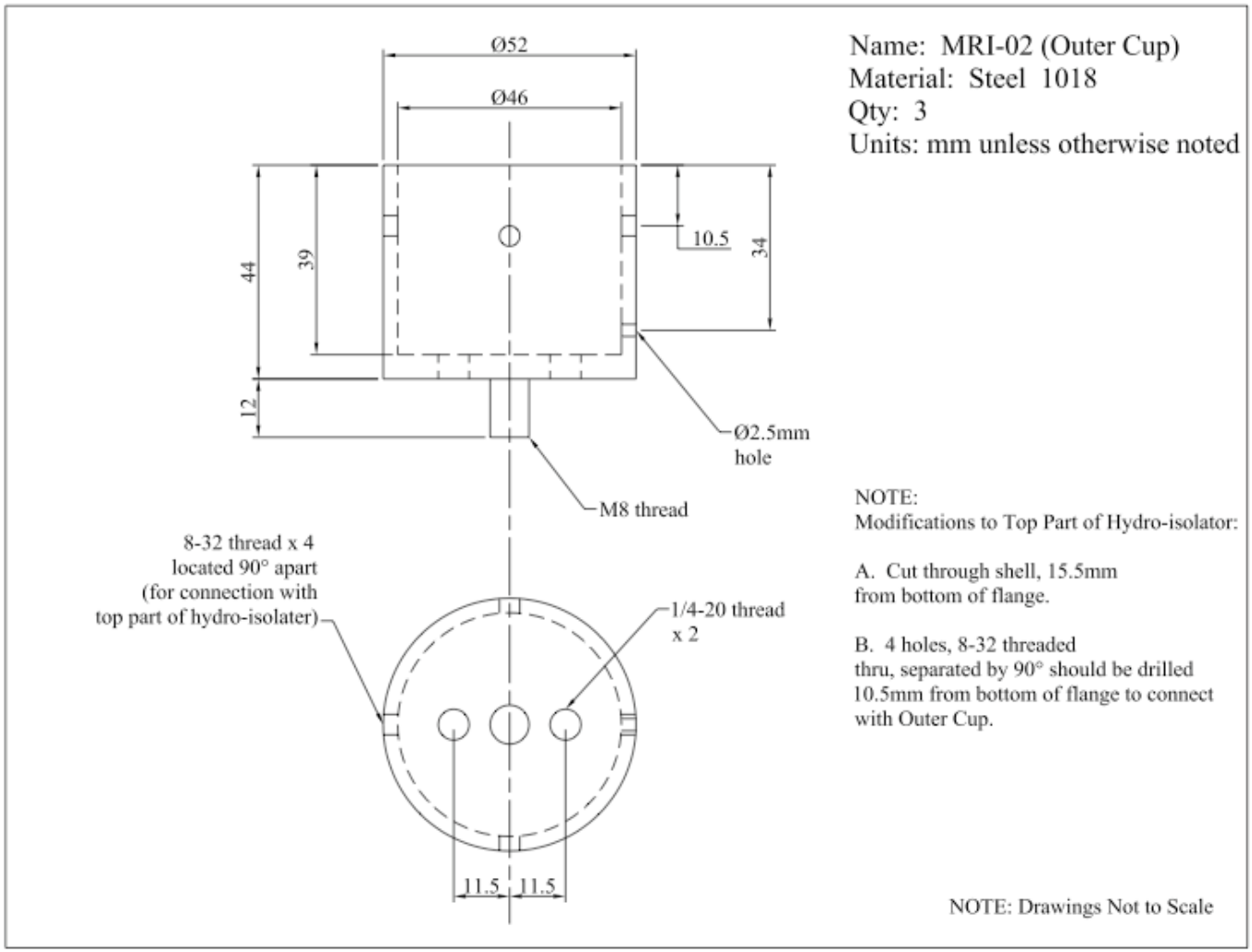
Ø52
Ø46
44
39
10.5
34
12
Ø2.5mm
hole
M8 thread
8-32 thread x 4
located 90° apart
(for connection with
top part of hydro-isolater)
1/4-20 thread
x 2
11.5
11.5
Name: MRI-02 (Outer Cup)
Material: Steel 1018
Qty: 3
Units: mm unless otherwise noted
NOTE:
Modifications to Top Part of Hydro-isolator:
A. Cut through shell, 15.5mm
from bottom of flange.
B. 4 holes, 8-32 threaded
thru, separated by 90° should be drilled
10.5mm from bottom of flange to connect
with Outer Cup.
NOTE: Drawings Not to Scale

Name: MRI-D1-002 (Design 1 Bobbin)
Material: 1018 Steel
Qty: 1
Units: mm unless otherwise noted

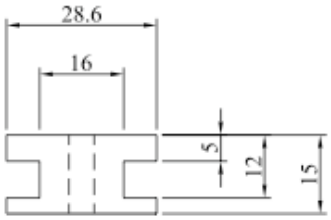

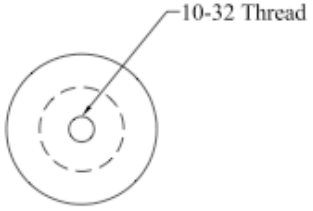

NOTE: Drawings Not to Scale

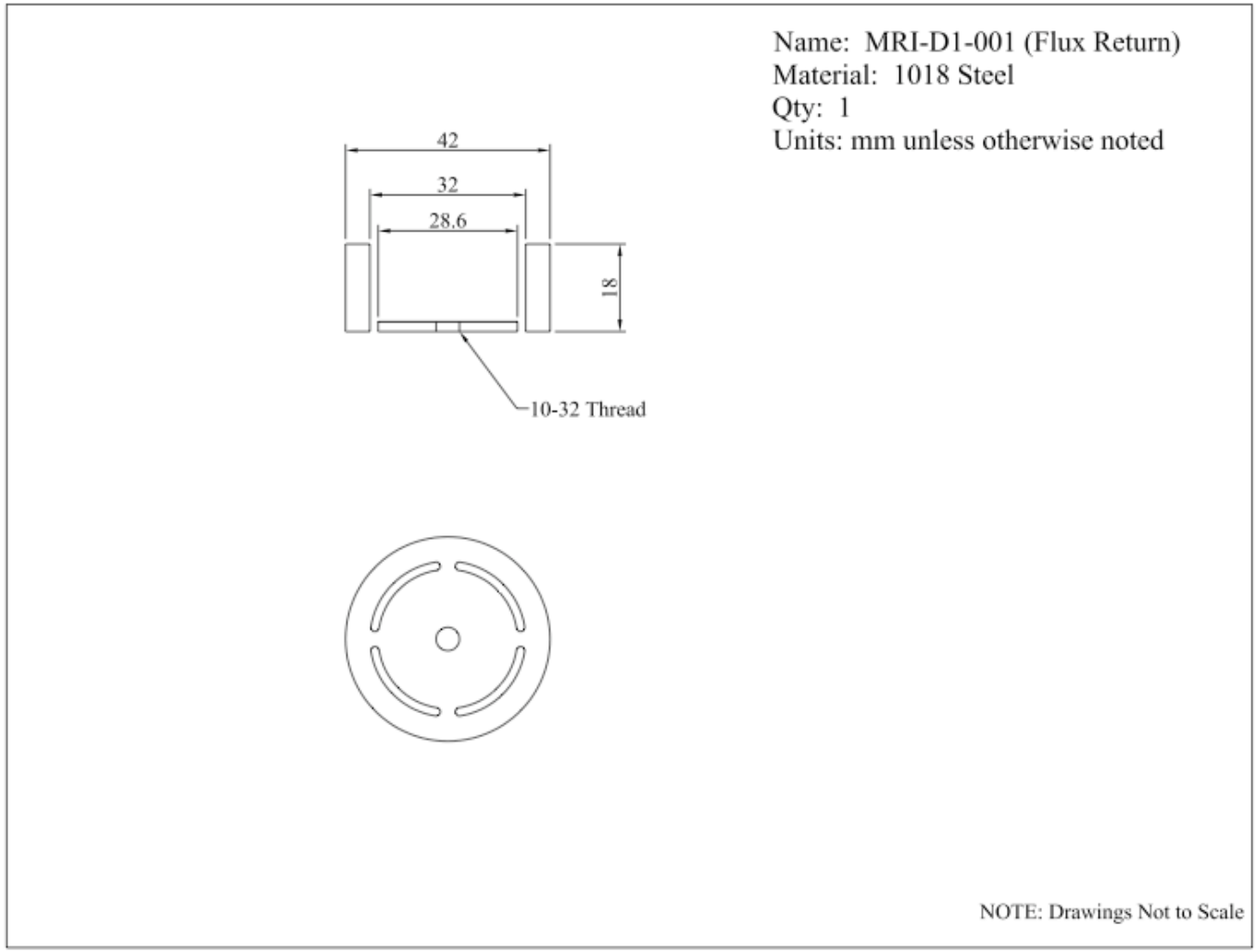
Name: MRI-D1-001 (Flux Return)
Material: 1018 Steel
Qty: 1
Units: mm unless otherwise noted
42
32
28.6
18
10-32 Thread
NOTE: Drawings Not to Scale

Name: MRI-D2-002 (Design 2 Bobbin)
Material: Aluminum
Qty: 1
Units: mm unless otherwise noted

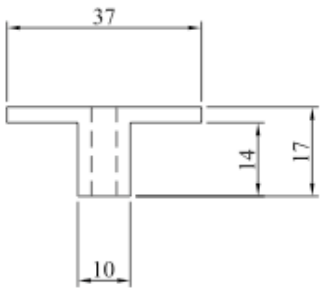

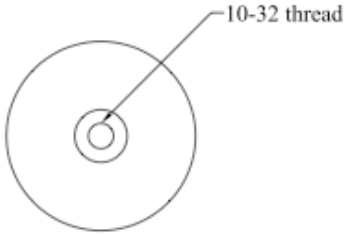

NOTE: Drawings Not to Scale

Name: MRI-D3-002 (Design 3 Bobbin)
Material: Steel 1018
Qty: 3
Units: mm unless otherwise noted

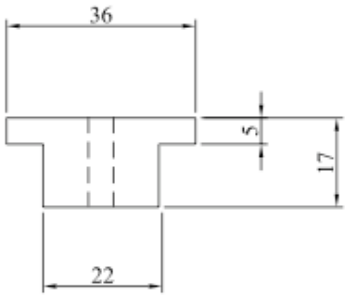

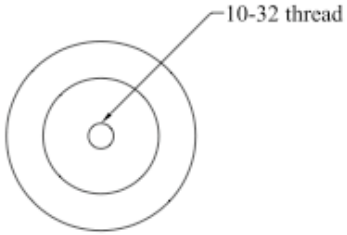

NOTE: Drawings Not to Scale